

	<b>BelSAR Campaign 2018</b>	Doc.	RP-CSL-BEL-19003
	<b>Final Report</b>	Date	10/08/2019
		Issue:	1.1
		Page:	1 of 103

---

# Technical Assistance for the Deployment of an L-Band SAR system to perform bistatic and interferometric SAR measurements during the ESA BelSAR Campaign

## Final Report

August 10, 2019

Ref.: PR-CSL-BEL-19003

*Document written in the frame of the contract 4000117154/16/NL/FF/mc  
between ESA and Centre Spatial de Liège*

### Document Change Record

Issue	Date	Comments
1	25/04/2019	First issue
1.1	10/08/2019	Clarifications in <ul style="list-style-type: none"> <li>- §7.1 Campaign implementation</li> <li>- §8.6 NESZ</li> <li>- §11 Ground measurement: soil moisture and roughness</li> <li>- §12 Ground measurements: agriculture</li> </ul> Appendix added

### Distribution List

Name	Affiliation
D. Schuettmeyer	ESA
M. Davidson	ESA
L. Fabrizi	ESA
A. Orban	CSL
C. Barbier	CSL
D. Defrere	CSL
Configuration Management Office	CSL
X. Neyt	RMA
F. Bettens	RMA
D. Heymans	UCLouvain
P. Defourny	UCLouvain
N. Verhoest	UGent
J. Claessen	UGent
A. Coccia	MetaSensing
C. Trampuz	MetaSensing
K. Macedo	MetaSensing

## Contents

<b>1</b>	<b>Scope of the Document .....</b>	<b>8</b>
<b>2</b>	<b>Documents .....</b>	<b>8</b>
2.1	Applicable Documents .....	8
2.2	References.....	8
<b>3</b>	<b>Context and Objectives of the Campaign .....</b>	<b>10</b>
<b>4</b>	<b>Scientific and Technical Requirements .....</b>	<b>12</b>
4.1	Agriculture Requirements .....	12
4.2	Soil moisture Requirements.....	12
4.3	Bistatic SAR Science Requirements .....	13
4.4	InSAR Requirements.....	14
4.4.1	Geometrical across-track decorrelation.....	15
4.4.2	Along-track baseline.....	17
4.4.3	Squint considerations.....	18
4.4.4	Preliminary conclusions .....	18
4.5	SAR Processing Requirements.....	19
4.6	Corner reflectors .....	19
4.6.1	Deployment.....	20
<b>5</b>	<b>Test Site Definition.....</b>	<b>22</b>
5.1	Area of Interest .....	22
5.2	Individual fields identification .....	22
5.3	Subset.....	22
<b>6</b>	<b>Flight Hardware .....</b>	<b>24</b>
6.1	L band SAR system .....	24
6.1.1	Sensor.....	24
6.1.2	Antennas .....	25
6.2	Technical Test Campaign.....	26
6.3	Airplanes Provider and Onboard Installation.....	27
<b>7</b>	<b>Airborne Data Acquisition .....</b>	<b>30</b>
7.1	Campaign Implementation.....	30
7.2	Acquired SAR Data .....	33
7.3	Stored Data Format.....	35
<b>8</b>	<b>SAR Data Processing and Results .....</b>	<b>36</b>
8.1	Processing of airborne SAR data .....	36
8.2	Quick data look .....	37
8.3	Navigation data.....	38
8.4	Processed SAR Data .....	39
8.5	Geo-referencing check .....	42
8.6	Noise-Equivalent Sigma Zero (NESZ) estimation.....	45
8.7	Impulse Response Function (IRF) .....	46
8.8	Additional Comments for further Interferometric Processing.....	47
8.9	Conclusion .....	50
<b>9</b>	<b>Bistatic SAR Science .....</b>	<b>51</b>
9.1	Data with ground-range misalignment .....	51
9.1.1	Data and selection of scatterers .....	51
9.1.2	Analysis of the ground-range misalignment .....	51
9.2	Analysis of random phase noise effects in the azimuth direction .....	51
9.2.1	Introduction .....	51

9.2.2	The random phase noise model.....	52
9.2.3	Analysis.....	54
9.2.4	Simulations and results .....	55
9.3	Conclusions .....	57
<b>10</b>	<b>Interferometric Processing .....</b>	<b>58</b>
10.1	Description of data sets .....	58
10.2	Data processing.....	58
10.3	Example of results.....	58
10.4	Temporal loss of coherence .....	61
10.5	Geometric loss of coherence .....	62
10.6	Output data and file format.....	63
10.7	Conclusions .....	63
<b>11</b>	<b>Ground measurements: Soil moisture and roughness.....</b>	<b>65</b>
11.1	Hardware.....	65
11.2	Protocol.....	65
11.2.1	Soil moisture measurement .....	65
11.2.2	Bulk density measurement.....	66
11.2.3	Soil roughness measurement.....	66
11.2.4	Error characteristics .....	66
11.3	Acquisition report .....	66
11.4	Preliminary Analysis .....	69
11.4.1	Data quality .....	69
11.4.2	Comparison radar versus bistatic radar .....	70
<b>12</b>	<b>Ground measurements: Agriculture.....</b>	<b>71</b>
12.1	Hardware.....	72
12.2	Protocol.....	72
12.2.1	Dataset 1 .....	72
12.2.2	Dataset 2 .....	73
12.3	Acquisition report .....	75
12.4	Preliminary Analysis.....	77
12.4.1	Field data analysis .....	77
12.4.2	SAR data .....	79
<b>13</b>	<b>Sentinel-1 acquisitions .....</b>	<b>85</b>
<b>14</b>	<b>Summary and Conclusions.....</b>	<b>86</b>
	<b>Appendix A – MetaSAR-L NetCDF data format.....</b>	<b>88</b>
A.1	File names.....	88
A.2	Variables.....	90
A.2.1	Variables 1D .....	90
A.2.2	Variables 2D .....	93
A.3	Parameters .....	96
A.3.1	The RF antenna .....	96
A.3.2	The transformation matrix.....	97
A.3.3	Others .....	98
	<b>Appendix B - Acronyms.....</b>	<b>103</b>

## Table of Figures

Figure 4-1 Estimated coherence as a function of incidence angle, for various orthogonal baselines and flight altitudes (top: allocated bandwidth of 50MHz, bottom: 100MHz) .....	16
Figure 4-2 On ground antenna footprint computed for an incidence at mid swath of 40° at flight altitude 2000m .....	17
Figure 4-3 Schematic representation of mono and bistatic range migration (left: no squint, both antennas are observing strictly across track at right angle with respect to flight direction; right: symmetrically squinted antennas).....	18
Figure 4-4 Picture and main characteristics of the corner reflectors. ....	20
Figure 4-5 Corner reflectors localization within the subset .....	20
Figure 4-6 Orientation of the corner reflectors with respect to aircraft trajectory, both in elevation (left) and azimuth (right) directions. ....	21
Figure 5-1 Localization of the selected area inside the Hesbania BELAIR site, with average slope (left) and APEX flight lines (right) ( <i>on Google Earth – Google Map</i> ).....	22
Figure 5-2 Selected area with waypoints and the 3 parallel swaths covering the full area. Fields (blue: wheat, orange: maize) and Corner Reflectors (white triangles) locations. The subset area is in red. Fields outside the white area are not guaranteed to be imaged. ....	23
Figure 6-1 L-band sensor .....	25
Figure 6-2 Installation of MetaSAR-L on board a C208 in NL .....	26
Figure 6-3 Airborne configuration, showing the very small baseline that can be achieved (C208s used for test flight in NL).....	27
Figure 6-4 Monostatic (left) and bistatic (right) images, showing no azimuth undulation or drift, but only range shift as expected from the theory. ....	27
Figure 6-5 The installation of the Mission Equipment in the C208.....	28
Figure 6-6 Pictures of the two Cessna 208 from Skydive Spa .....	29
Figure 7-1 Track design for the BeISAR AOI, simulated for an antenna look angle of 45°, flight altitude of 1500 m AGL, 40° 3dB beamwidth in elevation, 20% images overlapping. ....	31
Figure 7-2 Areal pictures of corner reflector number 4 (CR4) shot during different missions; from top left, clockwise: M2, M3, M4, M5. ....	32
Figure 7-3 Ground pictures of corner reflector number 4 (CR4) shot during different missions; from top left, clockwise: M1, M2, M3, M5. ....	33
Figure 8-1 SAR processing implemented on BeISAR airborne data .....	36
Figure 8-2 Example of Range-Doppler maps processed after each acquisition day as data check. ....	38
Figure 8-3 Example of post-processed navigation data: AC track plotted over Google Earth. ....	39
Figure 8-4 Georeferenced BeISAR images from Mission 2, monostatic mode. From top left, clockwise: HH, VH, HV, VV. ....	40
Figure 8-5 Georeferenced BeISAR images from Mission 2, XT configuration. From top left, clockwise: HH, VH, HV, VV. ....	41
Figure 8-6 Georeferenced BeISAR images from Mission 2, ATI configuration. From top left, clockwise: HH, VH, HV, VV. ....	42
Figure 8-7 Position of the CRs. (a) Designed positions on a google map image. (b) Polarimetric SAR image composite from M1, where red, green and blue correspond to HH, VV and HV pol, respectively: corner reflectors appear as yellow spots.....	43
Figure 8-8 CR: Processed SAR image versus measured geographical position (red cross). From top left, clockwise: CR1, CR2, CR3, CR4. ....	44
Figure 8-9 Detail of a processed SAR image: in the red circle the selected area with the lowest backscatter levels which have been used for the NSEZ estimation. ....	45
Figure 8-10 Phase (top) and coherence (bottom) between two delivered BeISAR images.....	48

Figure 8-11 Phase (top) and coherence (bottom) between two delivered BelSAR images after coherence optimization and phase filtering.....	49
Figure 8-12 SAR processing and post-processing for interferometric analysis on BelSAR data. ....	50
Figure 9-1 Reference phase noise spectrum.....	52
Figure 9-2 Stochastic realisations of the phase noise spectrum for both the Local Oscillator and the RF signal .....	53
Figure 9-3 Phase error sequences for different stochastic realisations of the phase noise (a) as raw sequences, (b) after removal of the linear component.....	54
Figure 9-4 Azimuth IRF for successive stochastic realisations of the phase noise after removal of the linear component from the phase noise error (plotted in color), compared to the ideal (noise-free) azimuth IRF (plotted in black).....	55
Figure 9-5 Evolution of the ISLR in function of the additional phase noise level (mean and std value), the black curve illustrates the ISLR in the absence of phase noise.....	56
Figure 9-6 Evolution of the ISLR in function of the coherent integration time (mean and std value), the black curve illustrates the ISLR in the absence of phase noise. ....	56
Figure 10-1 Example of co-registered master (left) and slave (right) backscatter coefficient images (mission 5 as master and mission 4 as slave, AT, track A, and polarization HH).....	59
Figure 10-2 Coherence map (left) and interferometric phase (right) for the image pair shown in Figure 10-1. ....	60
Figure 10-3 Coherence map for the same master image (mission 5, XT, track A, polarization HH) and the corresponding slave images for the four other mission (1 to 4 from left to right), illustrating the strong temporal loss of coherence. ....	61
Figure 10-4 Coherence map (left) and corresponding geometric decorrelation (right) for an example interferometric pair (mission 1, mission 2, XT, short track, polarization HH). The loss of coherence is clearly related to the geometric decorrelation, caused by the large perpendicular baseline.....	62
Figure 11-1 1-m pin profilometer, with a spacing of 1cm.....	66
Figure 11-2 Fields distribution for soil moisture and roughness measurements .....	67
Figure 11-3 Soil moisture & roughness acquisition areas.....	68
Figure 11-4 Field average soil moisture measurements for winter wheat (left) and maize (right) fields for the 5 missions. The different coloured lines represent different fields.....	69
Figure 11-5 Field average roughness correlation length (L) (top row) and root mean square variation (s) (bottom row). For each vegetation type, along and across track measurements were taken. Different colours represent different fields.....	70
Figure 11-6 Radar backscatter in function of soil moisture with roughness correlation length defining the colour or the dots for a selection of fields during campaign 1. Radar and bistatic radar are shown on top and bottom row, respectively.....	71
Figure 12-1 Typical crop calendar for winter wheat and maize in the Hesbania site (Belgium). The black time lines represent the crop canopy presence. The red arrows represent the five bistatic acquisitions period.....	73
Figure 12-2 Example of DHP picture in maize plot.....	74
Figure 12-3 (a) Biomass harvesting in maize plot and in-situ weighting of maize subsample and (b) Drying of subsamples in oven.....	74
Figure 12-4 Field data observation over the campaign for the agricultural variables (Fields of maize). ....	78
Figure 12-5 Field data observation over the campaign for the agricultural variables (Fields of winter wheat) .....	79
Figure 12-6 The three tracks (A-Z-B) of the AT and the polarisation HH from the mission 2. The winter wheat fields are displayed in blue and the maize fields in red.....	80
Figure 12-7 GAI function of the backscatter coefficient (maize) .....	81
Figure 12-8 GAI function of the backscatter coefficient (winter wheat) .....	82
Figure 12-9 SAR data for the different flights – all polarisation and interferometry. (Maize fields) .....	83

Figure 12-10 SAR data for the different flights – all polarisation and interferometry (winter wheat fields) 84  
Figure A-1 Example of delivered SAR data set. .... 88  
Figure A-2 Dimensions of the provided SAR images ..... 89

## Table of Tables

Table 4-1 MS bi-static acquisition system typical values ..... 15  
Table 6-1 Main specification for the MS L band sensor. .... 24  
Table 6-2 L-band RF antennas specs. .... 25  
Table 7-1 CRs orientation angles..... 31  
Table 7-2 Corner reflectors actual measurements for Mission 1 ..... 32  
Table 7-3 Mission 1 acquisition log..... 33  
Table 7-4 Mission 2 acquisition log..... 34  
Table 7-5 Mission 3 acquisition log..... 34  
Table 7-6 Mission 4 acquisition log..... 35  
Table 7-7 Mission 5 acquisition log..... 35  
Table 8-1 Accuracies of the post-processed navigation solutions for the two MetaSAR-L sensors for the five BeISAR missions, relatively to position and attitude measurements. .... 39  
Table 8-2 NESZ [dB] estimated from SAR data acquired during M1 ..... 45  
Table 8-3 NESZ [dB] estimated from SAR data acquired during M2 ..... 45  
Table 8-4 Ground-range resolution [m] estimated from IRF analysis of the four corners processed from data acquired during M2, for different polarization schemes The theoretical resolution is given in parenthesis for each corner ..... 46  
Table 8-5 Azimuth resolution [m] estimated from IRF analysis of the four corners processed from data acquired during M2, for different polarization schemes The theoretical resolution is given in parenthesis for each corner..... 46  
Table 11-1 Campaign summary – Soil moisture & roughness ..... 68  
Table 12-1 Campaign summary - Agriculture..... 76  
Table 13-1 Sentinel-1 acquisition planning..... 85

	<b>BeISAR Campaign 2018 Final Report</b>		Doc.	RP-CSL-BEL-19003
			Date	10/08/2019
			Issue:	1.1
			Page:	8 of 103

## 1 Scope of the Document

The present document presents the final report of the Bistatic Airborne L-band BeISAR Campaign performed in 2018 under ESA Contract 4000117154/16/NL/FF/mc, Technical Assistance for the Deployment of an L-Band SAR system to perform bistatic and interferometric SAR measurements during the 2015/2016 ESA BeISAR Campaign.

The partnership is composed by:

- Centre Spatial de Liège (CSL - ULiège)
- MetaSensing BV (MS)
- Laboratory of Hydrology and Water Management (LHWM) of the University of Gent (UG),
- Royal Military Academy (RMA),
- Earth and Life Institute (ELI) of the Université Catholique de Louvain (UCLouvain)

## 2 Documents

### 2.1 Applicable Documents

- [A01] Statement of Work, EOP-SM/2846/DS-ds, Technical Assistance for the Deployment of an L-Band SAR system to perform bistatic and interferometric SAR measurements during the 2015/2016 ESA BeISAR Campaign, issue 1, revision 2, dated 05/01/2015
- [A02] ESA Contract 4000117154/16/NL/FF/mc, Technical Assistance for the Deployment of an L-Band SAR system to perform bistatic and interferometric SAR measurements during the 2015/2016 ESA BeISAR Campaign
- [A03] MT-CSL-Bel-16001-BelSAR\_MoM, Negotiation meeting, 06/06/2016.
- [A04] MT-CSL-Bel-16002-Version 1\_0, Kick-off Meeting, 12/09/2016.
- [A05] CCN No.002, Contract Change Notice, Additional activities on BeISAR contract 4000117154/16/NL/FF/mc, 31/08/2018.

### 2.2 References

- [R01] SAOCOM Companion Satellite Science Report, ESA Document EOP-SM/2764/MWJD-mwjd, Dec. 2014.
- [R02] Technical Requirement Document, CSL-BEL-RP-16001, 02 March 2017
- [R03] MetaSensing L band SAR Sensor, 22/09/2016
- [R04] GOMOLZIG Flugzeug- und Maschinenbau GmbH (DO EASA.21J.274), Modification 2043841, C208B BeISAR Installation Provision, Issue: 03.04.2018
- [R05] BeISAR Campaign Implementation Plan, PLN-CSL-BEL-18001-BelSAR CIP, 23-07-2018

	<b>BelSAR Campaign 2018</b> <b>Final Report</b>		Doc.	RP-CSL-BEL-19003
			Date	10/08/2019
			Issue:	1.1
			Page:	<b>9 of 103</b>

- 
- [R06] MetaSAR-L NetCDF, File Format Description, MS-CSL-BEL-FFD-002-13, Iss. 1.3, 24 July 2019.
- [R07] BelSAR Campaign 2018 Logbook, LB-CSL-BEL-18001
- [R08] V. Kubica, Opportunistic radar imaging using a multichannel receiver, PhD thesis, Royal Military Academy (Belgium) - University College London (UK), 2016
- [R09] Gerhard Krieger and Marwan Younis, Impact of Oscillator Noise in Bistatic and Multistatic SAR, IEEE Geoscience and Remote Sensing Letters, vol. 3, no. 3, July 2006
- [R10] BelSAR Campaign 2018 Data Acquisition Report, RP-CSL-BEL-1806, 09/01/2019

	<b>BeSAR Campaign 2018 Final Report</b>		Doc.	RP-CSL-BEL-19003
			Date	10/08/2019
			Issue:	1.1
			Page:	<b>10 of 103</b>

### 3 Context and Objectives of the Campaign

The BeSAR project intended to carry out an airborne campaign for SAR bistatic interferometric measurements at L-band and full polarization, over a test site in Belgium.

The idea was to operate a flight campaign that fit as much as possible with the defunct SAOCOM/SAOCOM-CS configuration [R01] providing the opportunity to the science community to validate the capability of active-passive satellite configuration and to ensure the performances of L-band SAR bistatic or multistatic imagery. The intention was thus to assess the potential of SAR bistatic acquisitions in the particular domains of vegetation monitoring, soil moisture and bistatic SAR science, by the collection, over a selected test site in Belgium, of L-band full-polarimetric interferometric airborne SAR data, providing:

- Time series of interferometric coherence measurements,
- Monostatic and bistatic coherence signatures,
- Bistatic measurements to be used in the context of agriculture monitoring, soil moisture monitoring and bistatic SAR science.

to be associated with simultaneous field measurements, designed for providing:

- Information on crop types and stage of development for the main crop types of the selected region,
- Dielectric and geometric properties of a selection of maize and winter wheat fields

In addition to bistatic, polarimetric data, the campaign enabled for the first time single-pass L-band interferometry based on the formation flying of two planes with separate L-band payloads.

The acquisition schedule was driven by the applications: the campaign had to take place during the vegetation growth period:

- A 1<sup>st</sup> flight in May (bare soils for soil moisture assessment and preliminary to vegetation appearance)
- 3 flights between mid of June and end of July (vegetation growth season,)
- the last flight last in August or begin of September (soil moisture measurement on already harvested fields (mainly wheat) and still-growing vegetation follow-up, in particular maize).

The first step was to derive the technical and scientific requirements, allowing to define acquisition scenarios, and to perform a technical test campaign, with a possible feedback loop towards scientific requirements.

These tasks allowed to prepare the Campaign Implementation Plan and to secure the campaign in terms of technical readiness and in compliance with the air traffic control regulations. It must be highlighted that this step of obtaining the authorization to flight from the air traffic control authorities

	<b>BelSAR Campaign 2018</b> <b>Final Report</b>		Doc.	RP-CSL-BEL-19003
			Date	10/08/2019
			Issue:	1.1
			Page:	<b>11 of 103</b>

---

was very tricky and time consuming, mainly due to changes in European Regulation (April 2017) as well as the campaign area situation which is in close proximity the Charleroi airport. For this reason, the campaign was delayed from 2017 to 2018.

The five flight missions of the campaign were then done between end of May and mid of September 2018, simultaneously on air and in the fields. After a time left for verifying and processing the data, some preliminary scientific analyses have been done and are reported here. A further project supported by Belspo, BelSAR\_Science (12/2018 – 06/2021), is devoted to a more detailed exploitation of the data.

## BelSAR Campaign 2018 Final Report

### 4 Scientific and Technical Requirements

Scientific requirements specific to each targeted application have been derived from Task 1 of the project and are reported in details in the Technical Requirements Report CSL-BEL-RP-16001 (See [R02]).

#### 4.1 Agriculture Requirements

Temporal evolution of C-band SAR time series over agricultural areas have shown saturation effect as plants grow during the season. A larger penetration through vegetation of L-band signal occurs. For early growth stage the scattered signal is influence by both vegetation and underlying soil. As plant growth monitoring and crop recognition were the main focuses of the BelSAR project agricultural part, large incidence angle were required. Large incidence angles are preferred to limit the contribution of soil enhancing the part scattered by vegetation. Moreover, it is interesting to investigate the impact of incidence angle on the coherence along the season, which can only be done if a time series can be acquired with two fixed incidence angles through the agricultural season. The test site location had to be selected over flat or slightly undulated topographic area to avoid various incidence angle form one field to the other.

In order to avoid effect of early morning dew on the SAR signal, agricultural areas should not be imaged too early in the morning. Acquisition around mid-day was then recommended.

Agricultural crop recognition by remote sensing requires a diversity crop types to be covered in single scene. This can only be obtained over an area large enough. Considering the average field size (around 3.5 - 4 ha) and the crop type diversity of the region, an area of interest (AOI) of about 50-100 square km was recommended for mapping. Note that the AOI shape does not matter as soon as the width reaches at least 3 to 5 km to avoid imaging half of fields monitored on the ground. A large strip also would facilitate the selection of the 20 fields to be monitored on the ground for crop growth aligned in the plane track. Large fields were required to guarantee a sufficient number of pixels to reduce the speckle noise by multilooking of the SAR scattered signal.

#### 4.2 Soil moisture Requirements

Soil moisture sensing from radar is optimal if there is no or a limited amount of vegetation on the field. Furthermore, if a rain event happens between the image acquisition and the in situ measurements, significant differences in monitored soil moisture and the soil moisture at the time of acquisition can be found. Therefore, it was suggested not to fly on days for which rain is predicted.

Also at least one campaign had to be held during a period where a limited amount of vegetation is on the fields in order to test the relationship between the scattered signal and the observed soil moisture.

## BeISAR Campaign 2018 Final Report

### 4.3 Bistatic SAR Science Requirements

Bistatic systems have to overcome two synchronization challenges: time and phase synchronization.

Time synchronization refers to the process of recovering the time of transmission of each pulse needed to compute the range-to-target in the SAR processing. There are of course uncertainties in the available positions of the transmitter and the receiver and trajectory errors result in phase errors along the aperture.

As SAR is a coherent imaging system, a phase synchronization step is essential: the receiver and the transmitter must stay coherent during the illumination time of the scene. Knowledge of the phase of the transmitted signal at the receiver is required to perform SAR imaging. In a monostatic SAR, the same local oscillator is used for both the transmit and the receive function. In bistatic SAR, the separation between the transmitter and the receiver leads to the use of independent oscillators for modulation (at the transmitter side) and demodulation (at the receiver side) of the radar pulses. Any deviation between the two oscillators will result in a phase error in the bistatic data which, depending on magnitude and nature, will differently affect the SAR imaging.

In the frame of the BeISAR project, it was assumed that the two operating aircrafts would be equipped with GPS disciplined oscillators, each one generating a 10MHz reference clock, to synchronize the receiver with the transmitter.

The phase errors can be classified into two classes depending on their variation over the aperture: low-frequency errors, which have periods larger than the coherent integration time; and high-frequency errors, which vary rapidly over the aperture and have periods less than the coherent integration time.

Low-frequency errors encompass constant, linear, quadratic and higher order phase errors. Linear phase errors typically result in the shift of the point target response in azimuth direction but have no impact on SAR imaging focus. Quadratic phase errors cause broadening of the point target response. If it is space invariant, the effect is uniform defocus over the scene. One considers that, when the low-frequency phase errors are smaller than  $\pi/2$ , the effect on the focussed SAR point target response can be neglected. Low-frequency phase errors along the aperture can impose constraints concerning the maximal scene size to be imaged and on the maximal integration time.

High-frequency errors include sinusoidal and random phase errors and cause grating lobes to appear in the system impulse response. The inherent phase noise of a local oscillator is part of this category. A typical value for the allowable RMS high-frequency phase error is  $4^\circ$ .

The bistatic configuration consisted in two aircrafts, one is transmitting and the second receiving.

In practice, the positions of the transmitter/receiver and the frequencies are not known exactly. Therefore, the phase of the (computed) azimuth matched filter does not perfectly match the actual phase of the signal along the aperture.

## BelSAR Campaign 2018 Final Report

The consequences on the bistatic SAR imaging were studied by simulating an uncertainty on different parameters individually.

The associated phase error along the aperture can be modelled by a first-order polynomial and higher order terms. The first-order polynomial permits an estimation of the linear and the constant phase error. The latter does not affect the image quality itself, but affects the image position and might have an effect on the interferogram.

The phase error first-order modelling was performed for the entire scene. The linear phase component of the phase error is equivalent to a shift in Doppler frequency,  $\Delta f$ , resulting in a shift in the azimuth direction. The magnitude of the residual phase error after removal of the bias and the linear trend can be used to determine to what extent SAR defocussing occurs in the scene.

As an example, the impact of the frequency uncertainty of the local oscillators in the azimuth direction was evaluated, considering a specular geometry in which the transmitter and the receiver are on both sides of the imaged area. A (constant) uncertainty of the receiver's local oscillator of  $\Delta f = 50$  kHz was considered.

In a first scenario, the two aircrafts were considered as flying at the same speed and at the same flight altitude.

In a second scenario, the two aircrafts were still considered in the same specular geometry, but flying at two constant different speeds.

And in a third scenario, the two aircrafts were considered as flying with identical speed but at two different altitudes.

For the considered scene extent, it was shown (see the Technical Requirement Document) that the maximal residual quadratic phase error along the processed aperture due to an uncertainty of the frequency of the local oscillator of the receiver is smaller than the limit of  $\pi/2$ . Thus, despite a (very large) local oscillator frequency difference  $\Delta f = 50$  kHz, negligible SAR defocusing was expected for the considered geometrical configuration besides the expected shift of the scene.

For a synchronization analysis, following requirements were finally specified:

- the exact positions of both aircrafts, i.e., ideally, the raw data comprising the acceleration, rotations and GPS coordinates from the IMU
- the data sheets of the GPS disciplined local oscillators

### 4.4 InSAR Requirements

InSAR scientific requirements are defined principally for the coherence time series measurements. In the frame of the BELSAR project, they had to be defined for the two acquisition geometries: Bistatic Across-Track (XT) and the Along-Track (AT).

The study was based on the main characteristics of the system as given in Table 4-1:

	Value / typical value	Range	Notation
SAR carrier frequency	1.3 [GHz]		v
Signal bandwidth		[50 ; 200] [MHz]	B
PRF		[0.5 ; 10] [kHz]	prf
Azimuth resolution	> 0.3 [m]		Ra
Range resolution	> 0.75 [m]		Rr
Across-track minimum baseline	> 30 [m]		B <sub>⊥</sub>
Along-track minimum baseline	> 30 [m]		Ba
Flight altitude	~1200 [m] 4000 [ft]	[300 ; 3000] [m]	H
Velocity	57 [m/s] 110 [kn]	[46 ; 72] [m/s]	v
3dB antenna beam aperture: Range	40 [°]		θa
Azimuth	40 [°]		θr

**Table 4-1 MS bi-static acquisition system typical values**

Considering a maximum azimuth resolution of about 30cm, we deduced that the antenna length is of about 60 cm.

Since the 3 dB antenna aperture along range is of 40°, minimum boresight angle is of 20° to avoid left-right range ambiguities. The predefined boresight angle of the Metasensing system was of ~30° (swath width of about 3000 m at flight altitude 3000 m, considering the 3 dB range antenna aperture). Larger incidence angle was to be considered to both cover a wider area and meet UCLouvain and UGent requirements. Consequently, we considered an antenna boresight angle interval of [30° ; 50°], which allowed covering local incidence angle within the interval [10° ; 70°].

#### 4.4.1 Geometrical across-track decorrelation

The induced coherence losses for an uncorrelated distribution of surface scatterers may be approximate using the following expression:

$$\gamma_B = 1 - 2B_{\perp} \frac{R_r \cos(\alpha_0)}{\lambda r} = 1 + \frac{c_0 \cos(\alpha_0)}{2B h_a}$$

where

- $\gamma_B$  is the estimated coherence taking only into account the geometrical decorrelation
- $B_{\perp}$  is the across-track perpendicular baseline
- $R_r$  is the ground range system resolution
- $B$  is the range signal bandwidth

- $h_a$  is the ambiguity amplitude

First estimations of geometrical coherence losses with respect to antenna incidence angle, for different flight altitude and different cross-track baselines, were done considering a range signal bandwidth of 100 and 200 MHz (see [R02]). They had to be reviewed during campaign implementation, as the allocated bandwidth was only 50 MHz (see §7). The results are shown on Figure 4-1 for 50 and 100 MHz. Geometrical coherence losses increase with increasing baseline. These conditions are largely relaxed if working at higher resolution, it is to say at higher range bandwidth, and at higher altitude.

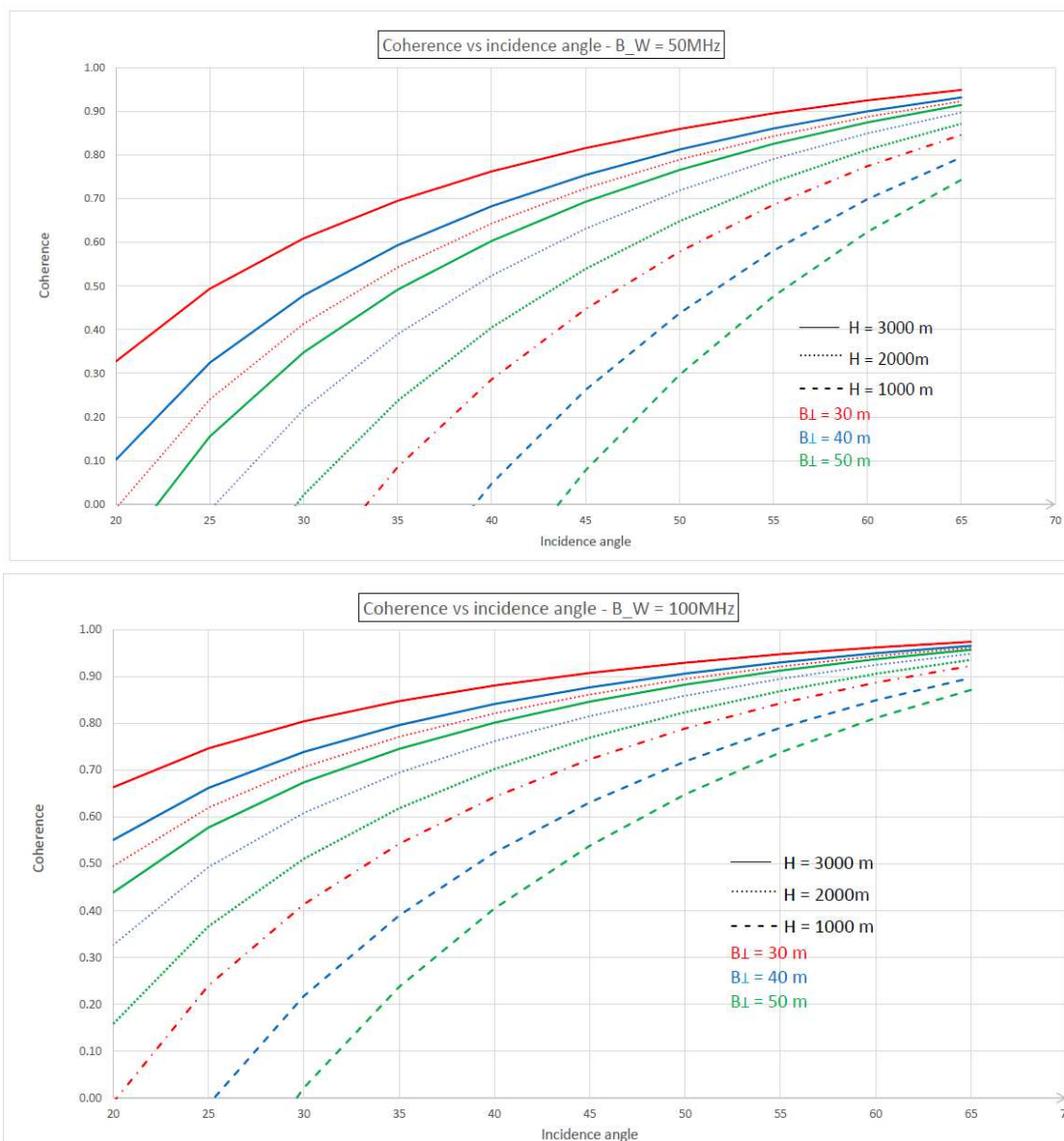


**Figure 4-1 Estimated coherence as a function of incidence angle, for various orthogonal baselines and flight altitudes (top: allocated bandwidth of 50MHz, bottom: 100MHz)**

#### 4.4.2 Along-track baseline

In both XT and AT configurations, the planes never fly in a strictly parallel formation, so that there always is an along-track baseline, so that it is not the same portion of the range migration curve that is travelled in each respective acquisition. Consequently, in a bi-static acquisition mode, each platform samples the azimuth signal on an azimuthal bandwidth centered on different Doppler Centroids.

As the target is observable by the receiving-only antenna only when it is located in the intersection of both footprints, interferometry between both acquisitions can only be considered on common azimuth frequency interval. In first approximation (if considering the bi-static acquisition as quasi mono-static), if the azimuth baseline is equal or bigger than half the azimuth footprint width, there is no common intersection of azimuth bandwidth. Half the azimuth spectrum is common to both acquisitions if the azimuth baseline is reduced to a fourth of the azimuth footprint width. Consequently, at the expense of an azimuth resolution loss of a half, images can be brought to interfere.

Figure 4-2 shows the 3 dB footprint for a flight altitude of 2000 m, considering an incidence angle of 40° at mid swath. Footprints were computed considering a sinc antenna pattern in both dimensions.

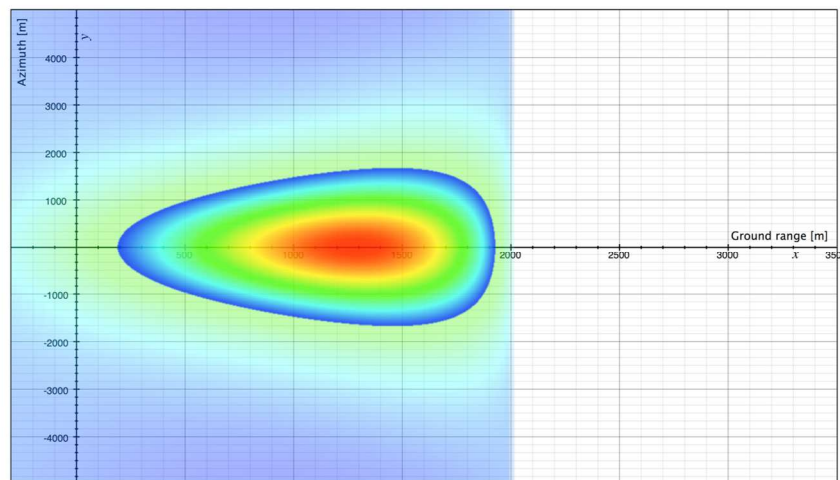


**Figure 4-2 On ground antenna footprint computed for an incidence at mid swath of 40° at flight altitude 2000m**

As can be seen, the 3 dB half width at mid antenna pattern is a little smaller than the flight altitude (~1800 m for H = 2000 m) and decreases with decreasing range. Consequently, if considering an along-track baseline of a fourth ( $\frac{1}{4}$ ) of the azimuthal footprint width at mid antenna pattern, the common intersection of azimuth spectra is half ( $\frac{1}{2}$ ) the azimuth bandwidth only at high ranges. This intersection decreases at lower ranges leading to larger azimuthal resolution losses. Additionally, it also means that the azimuthal filtering must be strongly range dependent to keep a good coherence.

To avoid too important azimuth resolution losses, but also to ease azimuth filtering while keeping a larger ground range swath available, we recommended to limit the along-track baseline to one eighth

( $1/8$ ) of the 3 dB azimuth footprint width at mid antenna pattern. Consequently, the along-track baseline is recommended to be kept below  $\sim 500$  m if flying at an altitude of 2000 m (and proportionally to the flight altitude).

#### 4.4.3 Squint considerations

Both Doppler spectrums are then identical except for a constant frequency shift, and the Doppler shift between mono and bi-static scanned spectrum is twice this frequency shift. One way to optimize azimuth spectrum superposition in the bistatic mode is to squint both antennas in order to always observe the same footprint: squinting the leading plane antenna beam backward and the following plane antenna beam forward to point at mid-azimuthal distance between both planes to keep both spectrums as much as possible centered on zero Doppler.

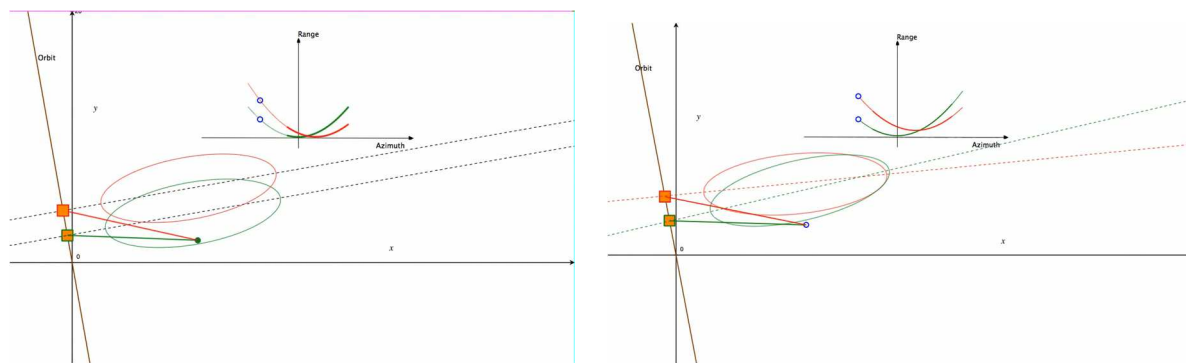


**Figure 4-3 Schematic representation of mono and bistatic range migration (left: no squint, both antennas are observing strictly across track at right angle with respect to flight direction; right: symmetrically squinted antennas)**

If both beams point to the same footprint, the azimuth resolution loss is proportional to the ratio of the time delay  $\Delta T$  between acquisitions and the mono-static synthetic antenna time length  $T_{3dB}$ .

In the monostatic acquisition, the scanned Doppler spectrum has a width given by:  $aT_{3dB}$ , where  $T_{3dB}$  is the 3 dB synthetic antenna integration time and  $a$  is the FM rate. Consequently, when both beams point to the same footprint, the azimuth resolution loss are proportional to the ratio of the time delay  $\Delta T$  between acquisitions and the mono-static synthetic antenna time length  $T_{3dB}$ :

$$\frac{\Delta T}{T_{3dB}} = 0.638 \frac{d}{r_0} \frac{L}{\lambda}$$

#### 4.4.4 Preliminary conclusions

To keep a convenient coherence range, it was recommended to keep the across-track baseline as short as possible and the flight altitude high. For an altitude of about 2000 m and for a signal bandwidth of

	<b>BeISAR Campaign 2018</b>		Doc.	RP-CSL-BEL-19003
	<b>Final Report</b>		Date	10/08/2019
			Issue:	1.1
			Page:	19 of 103

50 MHz, the recommended across-track baseline was below 30m. Increasing flight altitude and also signal bandwidth should allow relaxing the constraints.

The along-track baseline had to be below  $\frac{1}{4}$  of the flight altitude (below ~500 m at H = 2000 m).

#### 4.5 SAR Processing Requirements

Very few examples existed of bistatic airborne SAR images. Therefore, the generation of L-band bistatic images for vegetation monitoring that was performed in the BeISAR project was a very innovative step in remote sensing science with radar instruments. Data synchronization and processing combining the motion and attitude of 2 platforms are among the most stringent challenges in this endeavour. There were a number of challenges that must be overcome in the data processing in order to produce a focused output and these challenges are described hereafter.

The basic requirement for bistatic SAR processing is that the radar data are synchronized on a pulse-to-pulse basis. For achieving this, the two radars must start simultaneously and operate with the same clock. However, the two radars are on two different platforms flying at 300 km/h so no direct physical link is possible. A dedicated radio link for synchronization is also challenging and it showed problems in past attempts carried out by other researchers. MetaSensing devised a novel method to synchronize the radar data, based on GPSDOs (GPS Disciplined Oscillators) giving the system clock and trigger.

For generating bistatic images from the radar data, a novel SAR processor had to be implemented. The processor ingests radar raw data and the navigation data from two synchronized sensors and produces SAR bistatic images. The aircraft motion compensation of both airplanes is directly introduced in the processing chain and this is a very critical part that required severe effort. The processor had to be improved for automated processing of bistatic radar data sets with different geometrical configurations.

#### 4.6 Corner reflectors

The corner reflectors are meant not only to produce a geometrical reference but also to give the Point Spread Function (PSF) which gives the achieved resolutions. Besides, the PSF provides an indication about the quality of the synchronization between the transmitter and the receiver. The size of the used corner reflectors must be larger than the wavelength to be in the resonant scattering region and thus to have a higher RCS.

The corners that were used in this project are triangular-faced trihedrals. They are modular and they can be easily assembled with screws. They are lightweight and offer low resistance to wind thanks to honeycomb faces. Triangular pyramidal corner reflectors have a wide antenna diagram. Still, their correct installation and deployment is a fundamental aspect.

Four CRs were deployed on the fields and installed/removed before/after each acquisition flight by ground teams.

A picture and main characteristics of the CR are summarized in Figure 4-4.

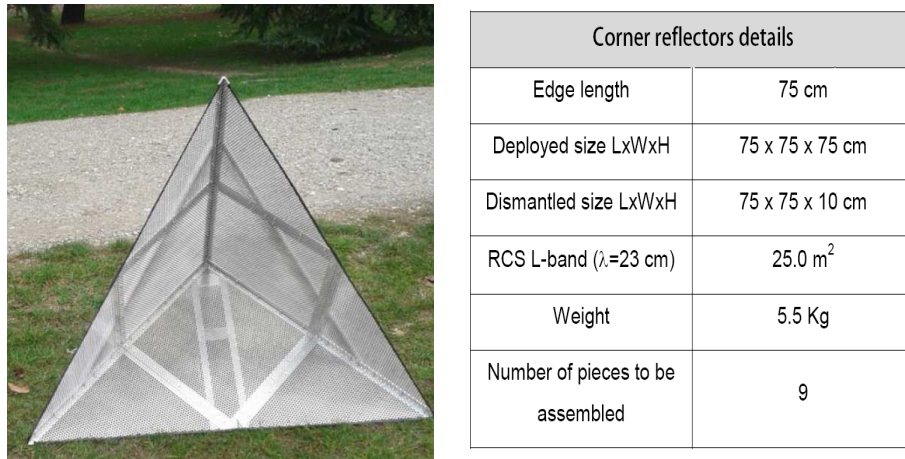


**Figure 4-4 Picture and main characteristics of the corner reflectors.**

#### 4.6.1 Deployment

The four corner reflectors were located on a line in the across-track direction. Ideally, they had to be located in an area of 50 m in both directions free of other reflecting objects to be able to see the side lobes of the PSF. The position was measured with a precision of 1 meter using a GNSS receiver.



**Figure 4-5 Corner reflectors localization within the subset**

They needed to be carefully oriented in both azimuth and elevation. The deployment and orientation were done by mean of tripods which were provided together with the corner reflectors. The corner can be oriented in the azimuth by a magnetic compass; it is important to take into account the

magnetic declination of the specific area where the measurement is done. For the elevation orientation a digital inclinometer can be used instead.

The values of the orientation and of the tilting angle depend on the acquisition geometry, mainly by the radar antenna pointing angle and by the flight altitude and direction (see Figure 4-6). In particular, in the elevation the main response direction of the corner must be complementary to the incidence angle (flat earth): for incidence angles between  $45^\circ$  and  $60^\circ$ , the base of the corner reflectors must be tilted downwards of  $19,5^\circ$  ( $(57^\circ - (60^\circ - 45^\circ))/2 - 30^\circ$ ). In azimuth, corner orientation and flight direction must be perpendicular, the angle of one of the vertical side of the corner reflector towards the flight trajectory being  $45^\circ$ .

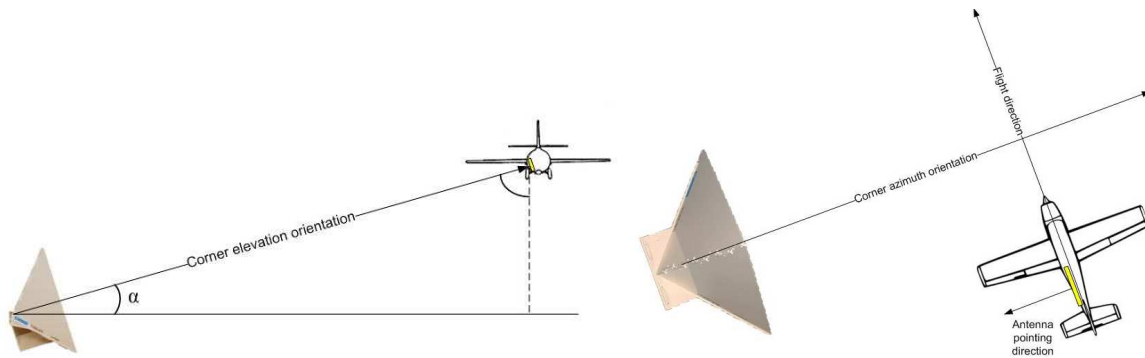


**Figure 4-6 Orientation of the corner reflectors with respect to aircraft trajectory, both in elevation (left) and azimuth (right) directions.**

## 5 Test Site Definition

### 5.1 Area of Interest

It was requested to be inside the HESBANIA area, which is one of the 3 BELAIR Belgian supersites. HESBANIA covers the rural area of Hesbaye/Haspengouw and is dedicated to agriculture and horticulture observations (see Figure 5-1). Lots of data had already been and continue to be collected over this area from air/space (visible) and ground measurements, among other during the APEX campaigns.

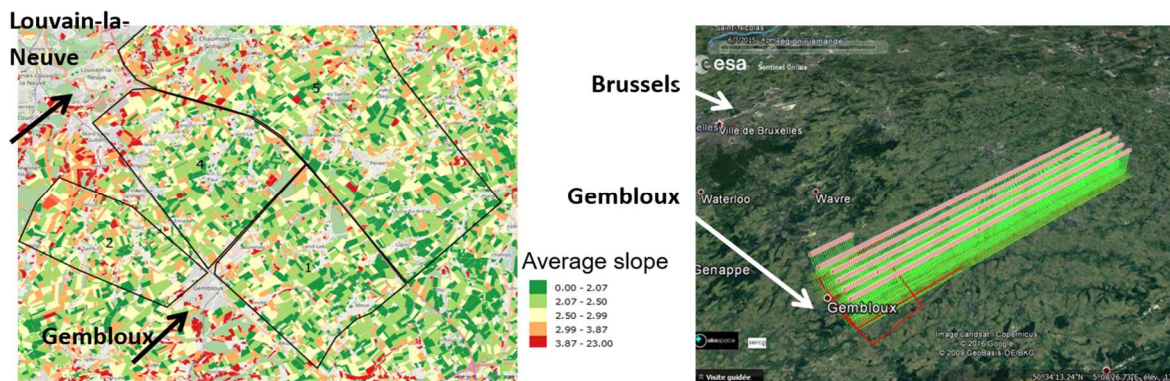


**Figure 5-1 Localization of the selected area inside the Hesbania BELAIR site, with average slope (left) and APEX flight lines (right) (on Google Earth – Google Map)**

The BeLSAR selected area measured about 15 x 4.5 km and it was limited by the following waypoints:

BS1	50°34'33"N	4°40'8"E
BS2	50°32'53"N	4°42'50"E
BS3	50°37'58"	4°51'52"E
BS4	50°39'51"N	4°49'15"E

### 5.2 Individual fields identification

For soil and plant parameters measurement, 20 fields were selected in the area of interest: 10 of winter wheat and 10 that were planned to be sown in maize by the farmers (see Figure 5-2). They all have more than 3-4 ha, are located in a rather flat terrain (fields slopes are no larger than 3 degrees) and are as homogeneous as possible (soil type, soil drainage, growing conditions).

### 5.3 Subset

In order to have a quick feedback of the data quality, a special subset of about 4 km, corresponding to a limited amount of data, was to be processed within 1 week after acquisition. The selected subset

incorporated the most numerous and representative fields (maize and winter wheat), and the 4 corner reflectors.

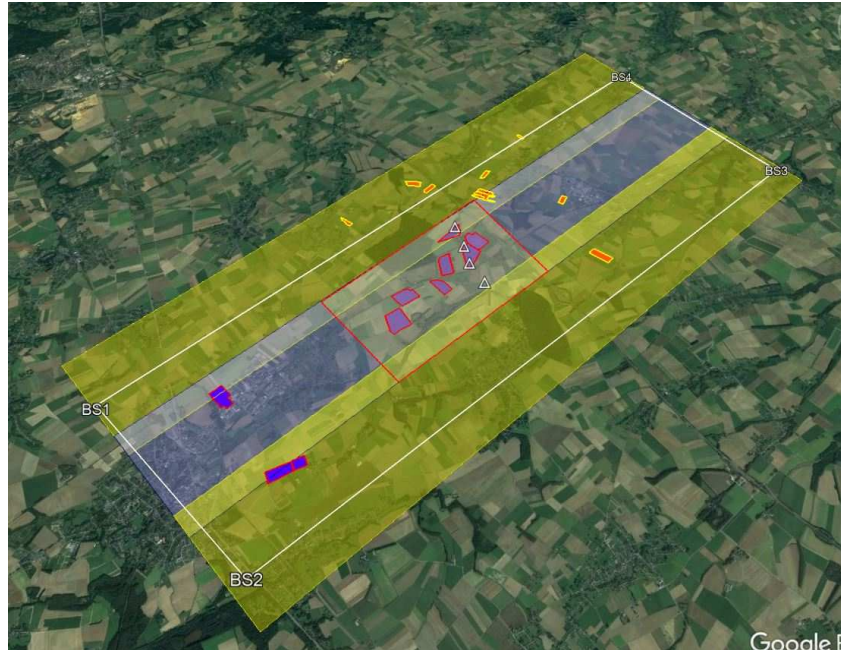


**Figure 5-2 Selected area with waypoints and the 3 parallel swaths covering the full area. Fields (blue: wheat, orange: maize) and Corner Reflectors (white triangles) locations. The subset area is in red. Fields outside the white area are not guaranteed to be imaged.**

## 6 Flight Hardware

### 6.1 L band SAR system

The L band SAR system is a versatile, compact (23x28x37 cm) and light weight (< 18 Kg) sensor characterized by low power consumption (<200 W) providing imaging with spatial resolution up to one meter. Depending on the application, it can be operated in polarimetric or interferometric modes, FMCW or pulsed modulation techniques. The sensor is equipped with flat panel antennas based on microstrip technology.

In Table 6-1, some technical specifications of the sensor are summarized. More details can be found in [R03].

MetaSensing L-band radar sensor	
Operating frequency	1.3 GHz (adjustable)
Bandwidth	Up to 200 MHz
Receiving channels	2
Polarization modes	VV / VH / HH / HV
Azimuth resolution	Up to 30 cm
Slant range resolution	Up to 75 cm
Swath width	Up to 8 Km
Radiometric accuracy	1 dB
Radiometric resolution	1 dB
DC power	10 – 28 VDC
Power consumption	< 200 Watt
Optimal platform	Cessna 208 Caravan

**Table 6-1 Main specification for the MS L band sensor.**

#### 6.1.1 Sensor

The MS L band sensor enclosure with dimensions is shown in the next figure. The sensor features a waveform generator, ADCs, control unit, data storage device, power converter stage and RF subsystem, including HPA (max power 10W, tunable) and LNA. An integrated navigation unit (GPS/IMU) is fastened on top of the sensor and a heat dissipater element is installed at one side. The overall sensor weight is less than 20 Kg, including sensor and navigation unit.



**Figure 6-1 L-band sensor**

### 6.1.2 Antennas

The RF antennas are based on microstrip technology (flat panel). Two kind of antennas were used for each flight, a squared and a rectangular one. Common characteristics include 1.2-1.35 GHz operating frequency range, dual (V & H) linear polarization, beamwidth of 40° in elevation. The antennas come with robust mounting kit. Main radiation characteristics are summarized in the Table 6-2. In Figure 6-2 the antenna set-up is shown, which has been used during some test flights in the Netherlands.

	Squared	Rectangular
<b>Frequency:</b>	1.20 - 1.35 GHz	1.2 - 1.4 GHz
<b>Gain:</b>	13 dBi Nom.	16 dBiC Target.
<b>Polarisation:</b>	Linear (Vertical & Horizontal)	Dual Linear (Vertical & Horizontal)
<b>Beamwidth:</b>	40° (Az) x 40° (El) Approx.	20° (Az) x 40° (El) Approx.
<b>Cross Polar:</b>	20 dB.	>20 dB.
<b>VSWR:</b>	1.5:1 Typ. 2:1 Max.	2:1 Max.
<b>Power Rating:</b>	10 W	10 W
<b>Front to Back:</b>	>30 dB	20 dB Approx.

**Table 6-2 L-band RF antennas specs.**



**Figure 6-2 Installation of MetaSAR-L on board a C208 in NL**

## 6.2 Technical Test Campaign

Synchronization of the 2 radar systems and bistatic de-ramping were preliminary tested in lab. An airborne test campaign was then planned as follows:

- A first flight with 1 aircraft and 2 sensors on board; to prove that the coherent bistatic de-ramping works also when moving fast with an aircraft and to exclude azimuth squint and undulation due to the processing
- A following flight with sensors on 2 different aircrafts. The pilots were trained for building the flight formation with the desired baselines. Special effort was put also in devising a robust method for coordinating the acquisitions of the two radar sensors, commanded by the operators on the two planes.

The aircrafts used for these campaigns were 2 Cessna's from the ParaCentrum of Teuge (NPCT - The Netherland).

The second flight with 2 planes allowed to generate bistatic coherent polarimetric airborne SAR images. Different configurations (AT and XT) were experimented with baselines between the few tens of meters and the several hundred meters. Different flight altitudes between 600 and 1500 m were also flown. All altitudes showed good SNR and swath in excess of 2 km. The boresight look angle was 45 degrees with local incidence angles in the swath between 30 and 60 degrees.



**Figure 6-3 Airborne configuration, showing the very small baseline that can be achieved (C208s used for test flight in NL)**



**Figure 6-4 Monostatic (left) and bistatic (right) images, showing no azimuth undulation or drift, but only range shift as expected from the theory.**

### 6.3 Airplanes Provider and Onboard Installation

The designed platform for the campaign was the Cessna 208 Grand Caravan. The aircraft provider was a Belgian parachuting (commercial) company, Skydive Spa, based few kilometers south of the town of SPA, Belgium, at the Aerodrome of Spa – La Sauvenière. This represented the base of airborne operations during the BelSAR campaign (see [R05], [R01]). Before each acquisition the MetaSAR systems (namely L1 and L2) were installed on board inside the fuselage, according to the installation instructions [R04]. All the equipment was fastened inside each aircraft, including the RF antennas which radiate radar signal through the lateral cargo door, see Figure 6-6. For both aircrafts, the set-up resulted in a left-hand side looking SAR configuration, characterized by a nominal antenna look angle of 45°.

An EASA certification process was initiated in order to certificate such installation on board the C208. The German company Gomolzig Flugzeug- und Maschinenbau GmbH was appointed for this task. Two

C208 aircraft from Skydive Spa underwent the certification process, with registration numbers OO-SPA and OO-SEX. Aircraft Maintenance Netherlands (AMN) B.V., based in Teuge, The Netherlands (EASA part 145 organization) performed the installations on the two aircrafts. The installation/certification is divided into two parts: permanent installation (GPS antenna and power electronics) and removable equipment (MetaSAR-L system which needed to be installed/removed before/after each acquisition flight).



**Figure 6-5 The installation of the Mission Equipment in the C208.**





**Figure 6-6 Pictures of the two Cessna 208 from Skydive Spa**

	<b>BelSAR Campaign 2018</b> <b>Final Report</b>		Doc.	RP-CSL-BEL-19003
			Date	10/08/2019
			Issue:	1.1
			Page:	<b>30 of 103</b>

## 7 Airborne Data Acquisition

### 7.1 Campaign Implementation

All acquisitions have been performed with the following parameters:

#### Frequency allocation:

Authorized bandwidth allocated by BIPT (Belgian Institute for Post and Telecommunications, in charge of frequency spectrum management)

- Center frequency: 1375 MHz
- Authorized Signal bandwidth: 50 MHz

NB.: It must be highlighted that the restriction of the frequency bandwidth drastically affected the constraint on baseline for limited coherence losses.

PRF: 1.004 kHz

Sampling frequency: 50 MHz

#### Flight Level:

Authorization has been granted to fly at

- Flight Level 60 for missions M1 and M2
- Flight Level 70 for missions M3, M4 and M5

(See tables in § 7.2)

#### Baselines

- Across-track (XT) for tracks A, B, Z and  $Z_{\text{short}}$  :  $B_{\text{XT}} = 30$  m. *For safety reasons, the two airplanes operated at slightly different altitudes (~5 m). Additionally, to facilitate the tracking of the "slave" aircraft, the "master" aircraft flew few meters in front (~5 m).*
- Along-tracks (AT): tracks A, B, Z and  $Z_{\text{short}}$  :  $B_{\text{AT}} = 300$  m. *For safety reasons, and to avoid turbulences of the "master" aircraft on the "slave", the two airplanes operated at slightly different altitudes (~10 m). Ideally there was not across-track separation.*

The implementation, similar for the 5 flight missions, is shown in Figure 7-1:

- In yellow the tracks and estimated ground coverage for the two South-to-North tracks Alpha (A) and Bravo (B),

- in blue the one for the North-to-South track Zulu (Z). This last could be flown twice to complete two entire laps. For this reason, the subset, including the corner reflectors, was located within this track.

The missions were conducted along the 4 tracks Zulu, Alpha, Bravo, once in across-track (XT) and once in along-track (AT) configurations. A short data sample was also acquired over the corner reflectors (Zulu\_short track Z<sub>short</sub>) with the intention to perform a quick preliminary quality analysis of the data.

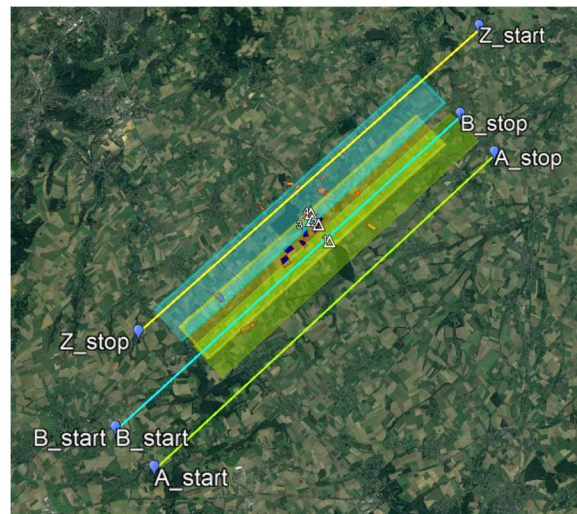


**Figure 7-1 Track design for the BeISAR AOI, simulated for an antenna look angle of 45°, flight altitude of 1500 m AGL, 40° 3dB beamwidth in elevation, 20% images overlapping.**

The 4 corner reflectors were mounted for each mission following instructions given in the Campaign Implementation Plan [R05] (location, azimuth and elevation angles) adapted to current flight level:

Corner reflector	Latitude	Longitude	Azimuth	Tilt angle (FL60)	Tilt angle (FL70)
CR 1	50°36'8.00"N	4°46'29.00"E	317°	30°	34.8°
CR 2	50°36'35.00"N	4°46'2.00"E	317°	41.5°	46.5°
CR 3	50°36'42.00"N	4°45'46.00"E	317°	47.3°	52.8°
CR 4	50°36'53.00"N	4°45'43.00"E	317°	53°	58°

**Table 7-1 CRs orientation angles**

Table 7-2 gives the actual measurements taken during M1 by ground teams.

	Latitude	Longitude	Azimuth	Elevation (morning)	Elevation (noon)	Elevation (evening)
<b>CR1</b>	50°36.1280'	4°46.4788'	317°	29.1°	29.1°	29.1°
<b>CR2</b>	50°36.5710'	4°46.0498'	317°	42.1°	42.3°	42.2°
<b>CR3</b>	50°36.7014'	4°45.7598'	317°	47.4°	47.4°	47.3°
<b>CR4</b>	50°36.8736'	4°45.7421'	317°	52.5°	52.7°	52.6°

**Table 7-2 Corner reflectors actual measurements for Mission 1**

Figure 7-2 and Figure 7-3 respectively show four aerial and four ground pictures of a deployed corner (CR4) taken during different missions over the site.



**Figure 7-2 Areal pictures of corner reflector number 4 (CR4) shot during different missions; from top left, clockwise: M2, M3, M4, M5.**

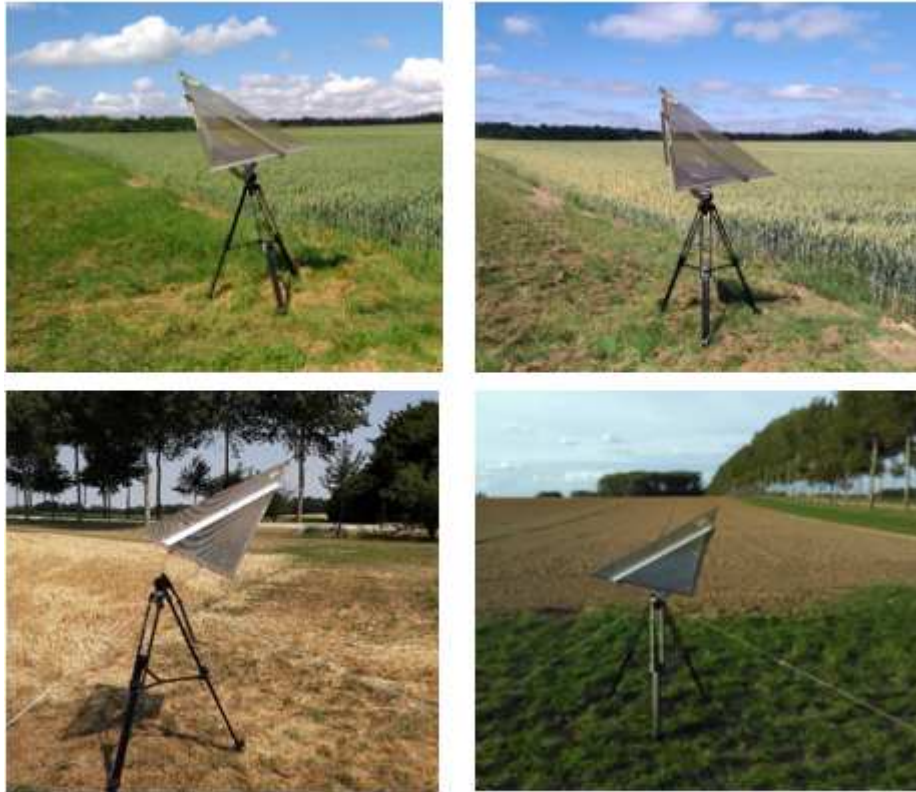


Figure 7-3 Ground pictures of corner reflector number 4 (CR4) shot during different missions; from top left, clockwise: M1, M2, M3, M5.

## 7.2 Acquired SAR Data

For each mission, data from monostatic and bistatic, XT and AT acquisitions, for the 4 polarization channels HH, HV, VH and VV, were acquired:

Mission 1:

Acq #	File ID (20180530...)		Track	Form	H <sub>msl</sub> [m]
	L1	L2			
1	153509	153510	Z	XTI	2100
2	154510	154509	B	XTI	2100
3	155509	155510	Z <sub>s</sub>	XTI	2100
4	160409	160410	A	XTI	2100
5	161309	161310	Z	ATI	2100
6	163610	163610	A	ATI	2100
7	165310	165309	B	ATI	2100
8	170210	170210	Z <sub>s</sub>	ATI	2100

Table 7-3 Mission 1 acquisition log

Mission 2:

Acq #	File ID (20180620...)		Track	Form	H <sub>msl</sub> [m]
	L1	L2			
1	134210	134210	Z	XTI	2320
2	135309	135309	B	XTI	2330
3	141110	141110	A	XTI	2310
4	142009	142009	Z <sub>s</sub>	XTI	2320
5	143709	143710	Z	ATI	2330
6	144810	144810	A	ATI	2330
7	145609	145609	Z <sub>s</sub>	ATI	2320
8	140509	150509	B	ATI	2330

**Table 7-4 Mission 2 acquisition log**

Mission 3:

Acq #	File ID (20180730...)		Track	Form	H <sub>msl</sub> [m]
	L1	L2			
1	144510	144510	A	XTI	2310
2	145410	145410	Z	XTI	2320
3	150609	150610	B	XTI	2300
4	151409	151409	Z <sub>s</sub>	XTI	2290
5	152410	152410	A	ATI	2310
6	153309	153309	Z	ATI	2300
7	154409	154410	B	ATI	2320
8	155210	155209	Z <sub>s</sub>	ATI	2310

**Table 7-5 Mission 3 acquisition log**

Mission 4:

Acq #	File ID (20180828...)		Track	Form	H <sub>msl</sub> [m]
	L1	L2			
1	143409	143410	Z <sub>s</sub>	XTI	2300
2	144309	144310	A	XTI	2290
3	145309	145310	Z	XTI	2290
4	150410	150410	B	XTI	2280
5	151409	151410	Z <sub>s</sub>	ATI	2280
6	152410	152409	A	ATI	2280

7	153410	153410	Z	ATI	2280
8	154410	154410	B	ATI	2280

**Table 7-6 Mission 4 acquisition log**

Mission 5:

Acq #	File ID (20180910...)		Track	Form	H <sub>msl</sub> [m]
	L1	L2			
1	144309	144310	B	XTI	2330
2	145209	145209	Z	XTI	2330
3	150410	150409	A	XTI	2340
4	151210	151209	Z <sub>s</sub>	XTI	2340
5	152209	152210	A	ATI	2340
6	153110	153110	Z	ATI	2340
7	154210	154209	B	ATI	2340
8	154910	154910	Z <sub>s</sub>	ATI	2320

**Table 7-7 Mission 5 acquisition log**

### 7.3 Stored Data Format

The processed SAR data format is described in detail in MetaSAR-L NetCDF, File Format Description, MS-CSL-BEL-FFD-002-13, Iss. 1.3, 24 July 2019 [R06], given in Appendix A.

The format of the stored interferometric products (master and slave amplitude and phase images, coherence maps and interferometric baseline maps) is described in Chapter 10 here below.

## 8 SAR Data Processing and Results

### 8.1 Processing of airborne SAR data

During each flight a short data sample was acquired over the corner reflectors (*Zulu\_short* track) with the intention of processing it and performing a preliminary quality analysis of the data. For reference, in this chapter the results are shown concerning M1 and M2.

Figure 8-1 shows the final implemented SAR processing chain used to deliver the SLC monostatic and bistatic SAR focused data of the BeISAR missions. All the output SLC data come in the same ground range grid and therefore data is co-registered. A description of the function of each block follows.

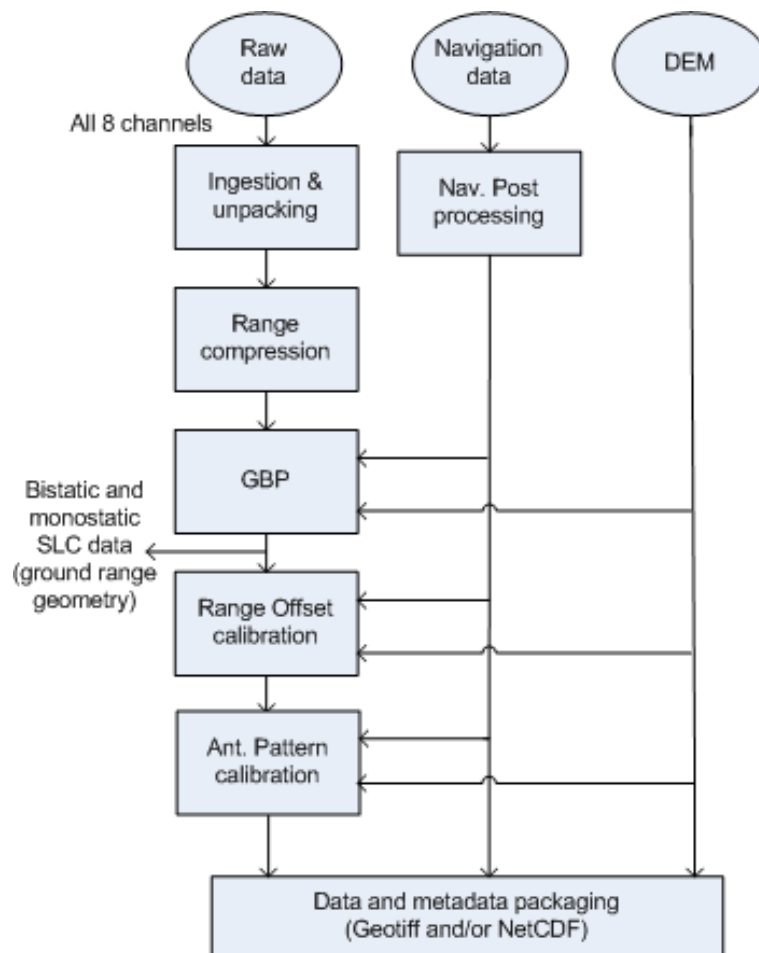


**Figure 8-1 SAR processing implemented on BeISAR airborne data**

	<b>BelSAR Campaign 2018</b> <b>Final Report</b>		Doc.	RP-CSL-BEL-19003
			Date	10/08/2019
			Issue:	1.1
			Page:	<b>37 of 103</b>

1. Ingestion & unpacking: the radar raw data is read and grouped according the transmission mode and the polarization channel.
2. Nav. Post processing: the GPS/IMU raw data are post-processed using information from ground base stations, to improve accuracy of the solution. Post-processed navigation data is synchronized with the radar data and the coordinate system is converted from the local frame into the coordinate system used by the SAR processor.
3. Range compression: the grouped raw data is pulse compressed and window filtered (Hanning) along slant range direction.
4. GBP: focus the range compressed data based on the global back projection (GBP) algorithm. The output data is projected into the specified ground range grid and, therefore, already ortho-rectified.
5. Range Offset Calibration: based on the position of the corners observed in the field, the slant range offset of focused SAR data is computed, and the corresponding slant range shift and phase correction are applied to the ortho-rectified focused data.
6. Ant. Pattern Calibration: based on the given antenna diagrams and radar geometry, the antenna gains are computed and compensated for each pixel in order to estimate a sigma nought image. The final sigma nought global offset is computed based on the radar cross section of the corner reflectors.
7. Data and metadata package: The final calibrated SLC SAR image is saved in a NetCDF file format along all metadata, which includes the antenna pattern, navigation data, digital elevation model used, geographical position of the focused pixels in geographical coordinates (WGS84). Detailed information about the NetCDF data format is provided in the appendix A at the end of this document.

## 8.2 Quick data look

During and after each mission a quick data look was performed to assess the campaign results. Raw data, Range-Doppler maps and SNR were plotted and analyzed from randomly selected datasets, as shown in the next figures (Figure 8-2).

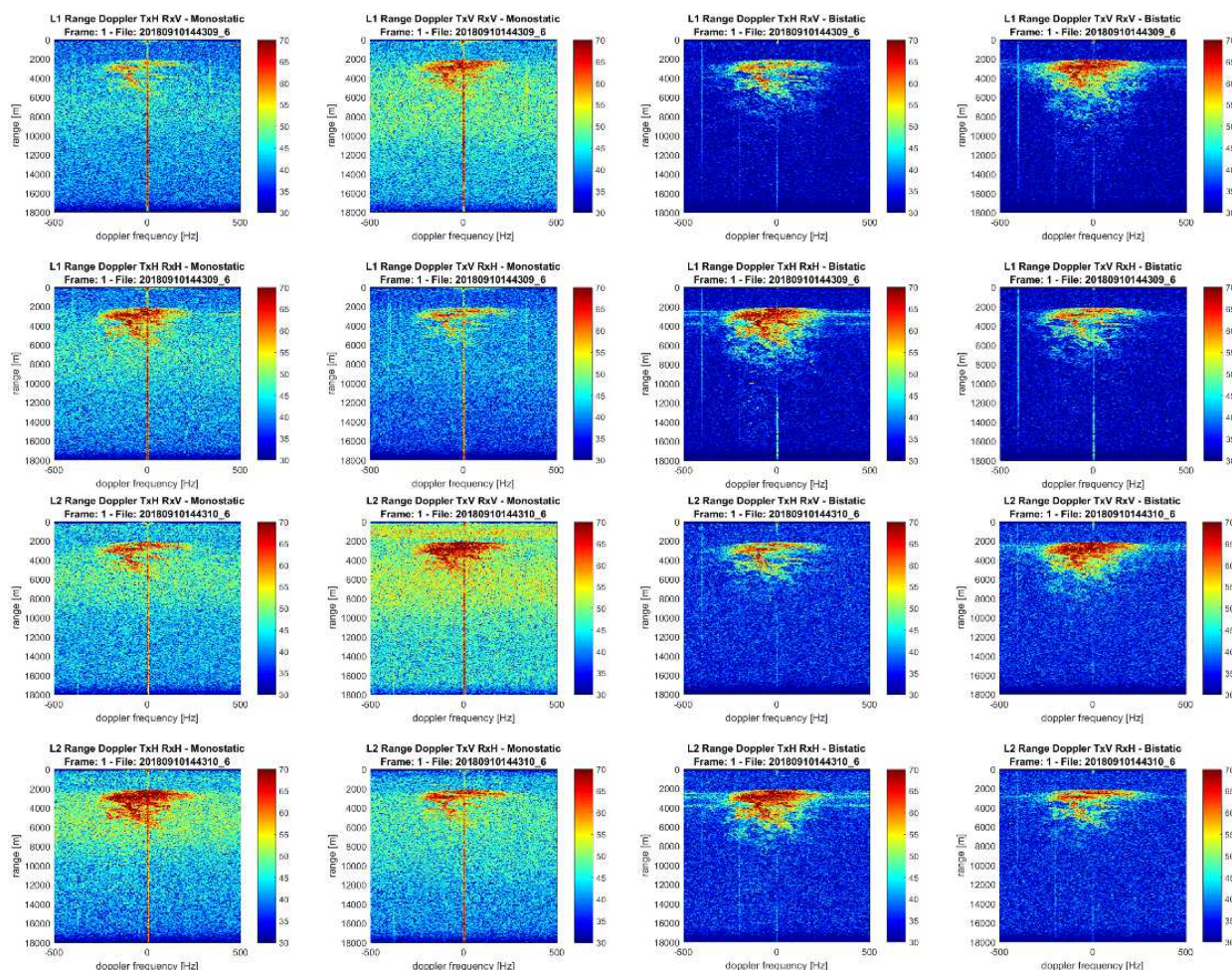


**Figure 8-2 Example of Range-Doppler maps processed after each acquisition day as data check.**

### 8.3 Navigation data

Besides the radar data, also the navigation data from both the MetaSAR-L systems underwent a quality check after being post-processed. To this extent, the accuracy of the computed solution was noted for both geographical position and inertial attitude.



**Figure 8-3 Example of post-processed navigation data: AC track plotted over Google Earth.**

The accuracies of the post-processed navigation solutions used for elaborating the BeISAR data are provided in Table 8-1 for all the 5 missions.

	MetaSAR-L1				MetaSAR-L2			
	Position [m]	Roll [°]	Pitch [°]	Yaw [°]	Position [m]	Roll [°]	Pitch [°]	Yaw [°]
<b>M1</b>	0.022	0.350	0.350	1.096	0.022	0.345	0.343	1.117
<b>M2</b>	0.023	0.365	0.364	1.231	0.024	0.372	0.371	1.363
<b>M3</b>	0.022	0.362	0.361	1.144	0.021	0.367	0.368	1.267
<b>M4</b>	0.020	0.375	0.374	1.296	0.021	0.375	0.374	1.363
<b>M5</b>	0.022	0.360	0.356	1.188	0.021	0.363	0.362	1.328

**Table 8-1 Accuracies of the post-processed navigation solutions for the two MetaSAR-L sensors for the five BeISAR missions, relatively to position and attitude measurements.**

## 8.4 Processed SAR Data

All the BeISAR images have been processed and calibrated for delivery (see Data Acquisition Report [R10] for the images from the short data samples over the corners). As an example, monostatic and bistatic (XT and AT modes) images from mission 2 are given here for each polarization channel.

**Mission 2 – Monostatic**

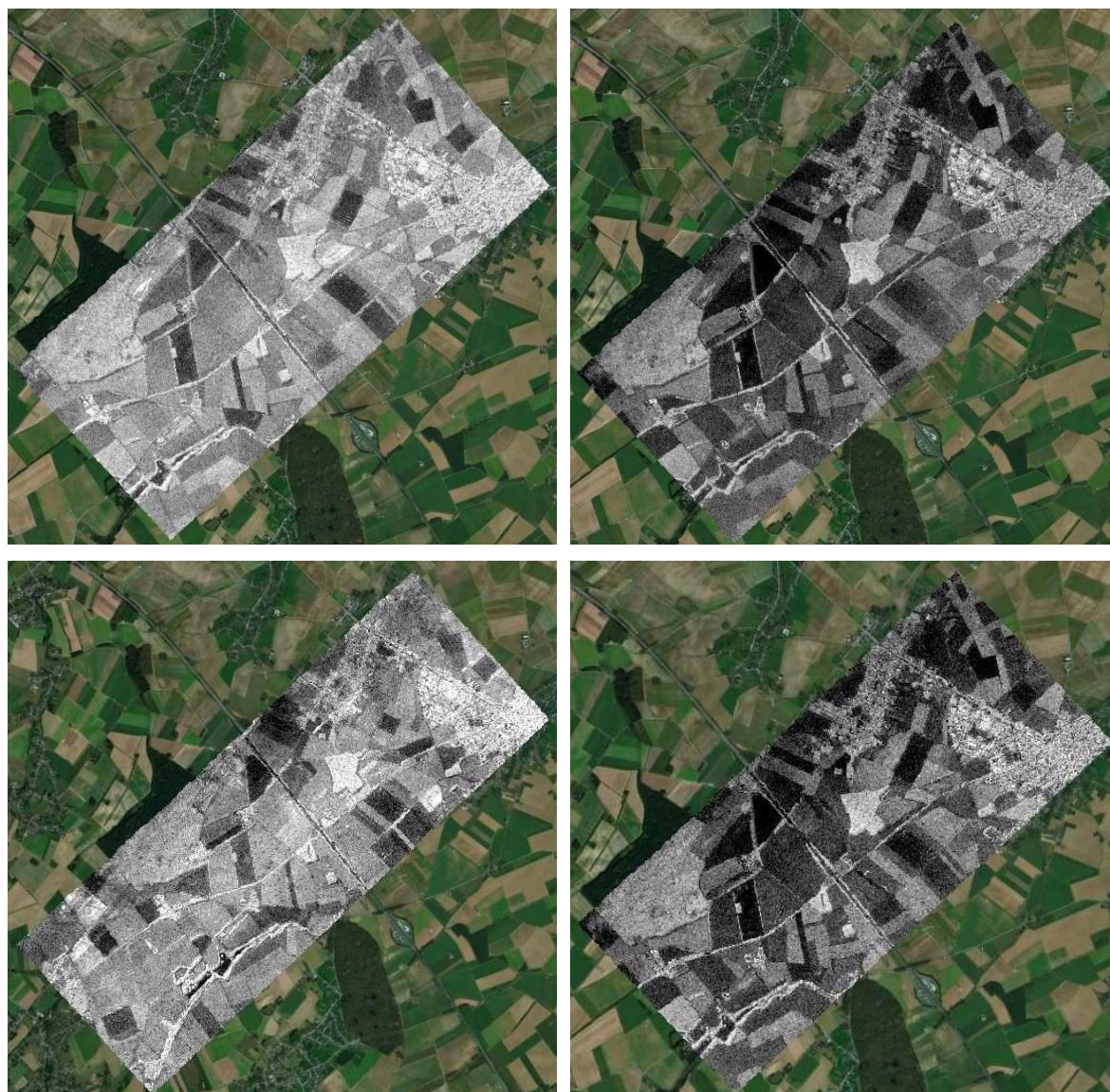


**Figure 8-4 Georeferenced BelSAR images from Mission 2, monostatic mode. From top left, clockwise: HH, VH, HV, VV.**

**Mission 2 – Bistatic XT**

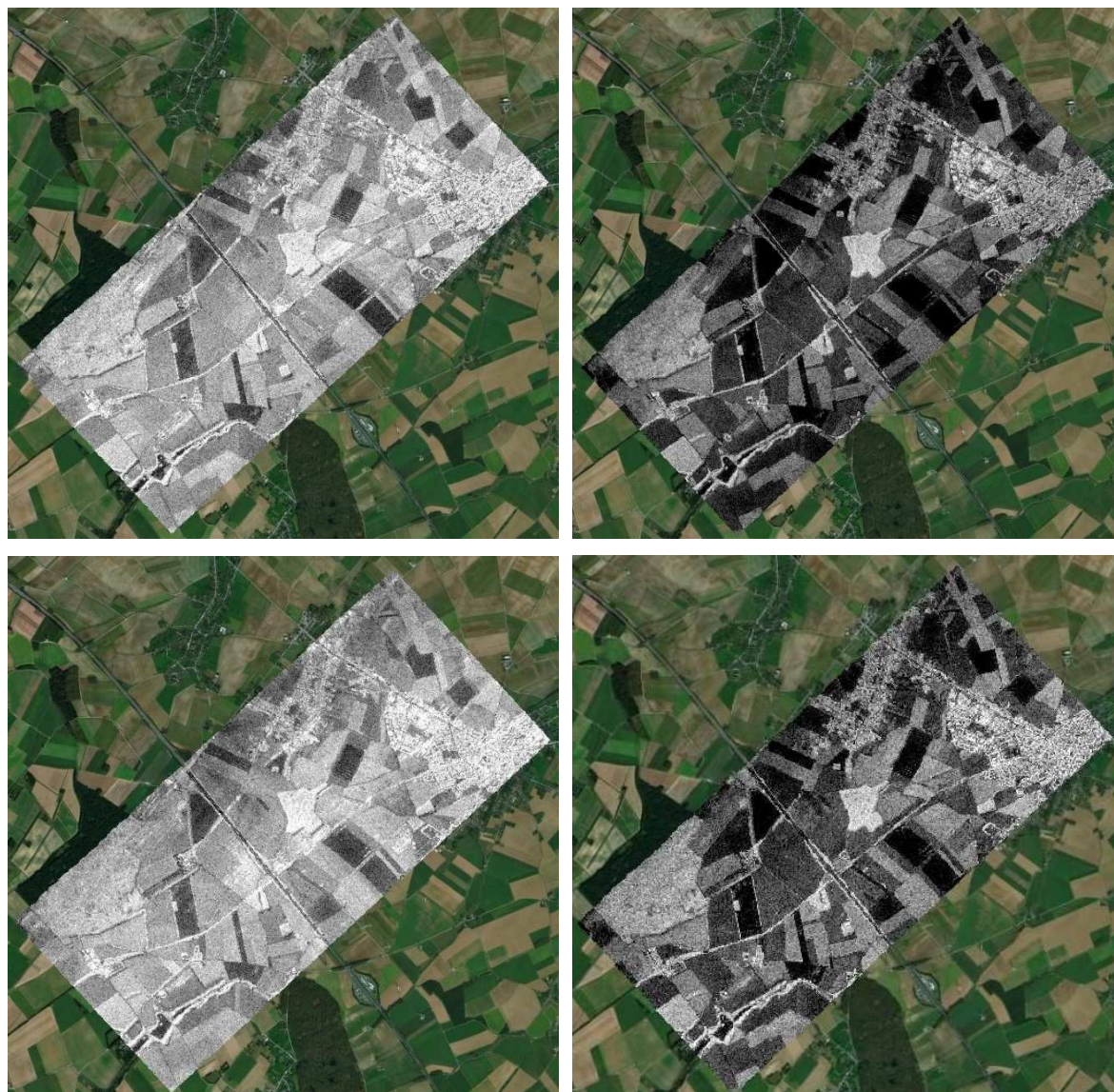


**Figure 8-5 Georeferenced BeISAR images from Mission 2, XT configuration. From top left, clockwise: HH, VH, HV, VV.**

## Mission 2 – Bistatic ATI

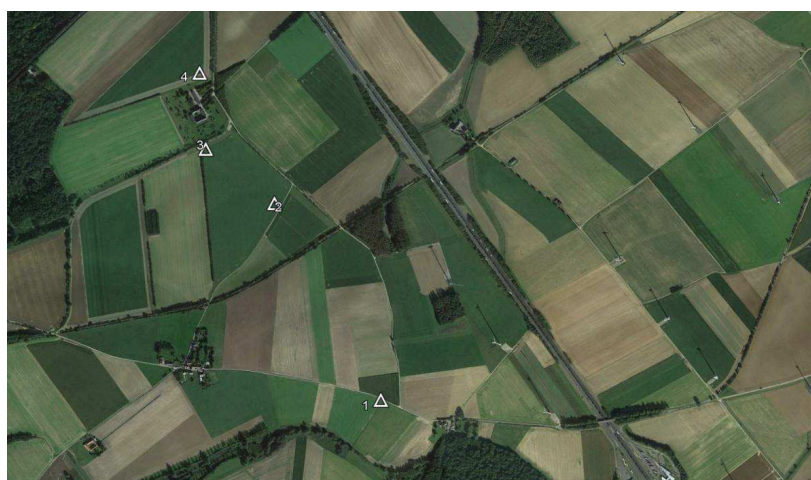


**Figure 8-6 Georeferenced BelSAR images from Mission 2, ATI configuration. From top left, clockwise: HH, VH, HV, VV.**

## 8.5 Geo-referencing check

Besides for the visual inspection, by overlapping on a GIS platform the processed images it is possible to check that the geo-referentiation step has been correctly performed.

Figure 8-7 (a) shows the designed position of the corners reflectors on a Google map image, while Figure 8-7 (b) is a polarimetric composite BelSAR image, where red, green and blue correspond to HH, VV and HV, respectively; there, the CRs appear as yellow spots, indicating a good polarimetric antenna characterization (as it will be shown also in the next section by IRF plots) and effective georeferencing.



(a)



(b)

**Figure 8-7 Position of the CRs. (a) Designed positions on a google map image. (b) Polarimetric SAR image composite from M1, where red, green and blue correspond to HH, VV and HV pol, respectively: corner reflectors appear as yellow spots.**

Figure 8-8 shows a zoom-in to each corner position from a georeferenced SAR image (acquisition 20180530155509, monostatic VV received with L1 during mission M1). In each plot, the red cross represents the measured geographical position of the corners (see Table 7-2). The geometric accuracy of the processed image is estimated in 0.75 m.

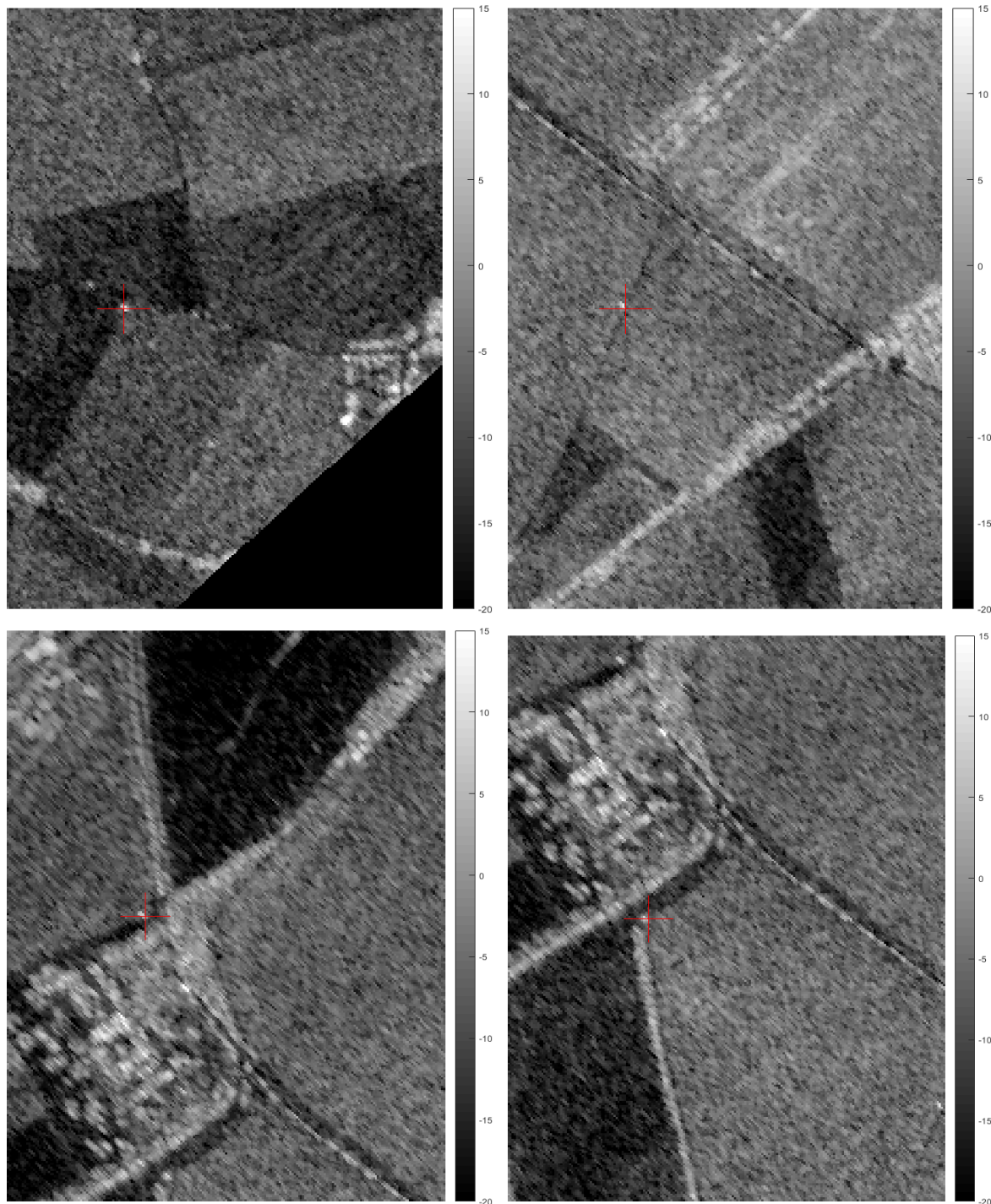


**Figure 8-8 CR: Processed SAR image versus measured geographical position (red cross). From top left, clockwise: CR1, CR2, CR3, CR4.**

## 8.6 Noise-Equivalent Sigma Zero (NESZ) estimation

The Noise-Equivalent Sigma Zero (NESZ) characteristics of the MetaSAR-L system has been estimated from the data acquired during the two initial missions M1 and M2. The information about corner reflectors has been used to absolutely calibrate the image; the backscatter values from an area with the lowest returns (see red circle in Figure 8-9) have been averaged and used to estimate the NESZ given Table 8-2 and Table 8-3 for M1 and M2, respectively. (See [R10] for other missions).



**Figure 8-9** Detail of a processed SAR image: in the red circle the selected area with the lowest backscatter levels which have been used for the NSEZ estimation.

Sensor	Monostatic		Bistatic	
	L1	L2	TxL2-RxL1	TxL1-RxL2
Co-pol H	-19.0	-26.0	-29.8	-28.6
Co-pol V	-20.5	-29.4	-29.1	-28.7
Cross-pol	-23.0	-31.0	-31.7	-31.7

**Table 8-2** NESZ [dB] estimated from SAR data acquired during M1

Sensor	Monostatic		Bistatic	
	L1	L2	TxL2-RxL1	TxL1-RxL2
Co-pol H	-19.6	-25.0	-26.7	-26.0
Co-pol V	-20.2	-27.5	-29.6	-27.7
Cross-pol	-21.8	-31.5	-32.7	-31.9

**Table 8-3** NESZ [dB] estimated from SAR data acquired during M2

The analysis shows a better performance of bistatic images w.r.t. monostatic ones, due to coupling effects. From the estimated values it can be concluded that the MetaSAR-L2 overperformed the MetaSAR-L1 in terms of sensitivity. This is due to the higher noise, as it can be noticed from the Range-Doppler maps shown in Figure 8-2. So, it is advised to use data from L2 for the monostatic imagery.

## 8.7 Impulse Response Function (IRF)

The IRF analysis of the corner reflectors is here provided to estimate the image resolution of processed SAR data and, eventually, to reveal imperfections in the image focusing which may be caused by residual motion error and/or synchronization issues. The IRF analysis also gives a polarimetric characterization of the processed images.

The IRF plots are provided in the Data Acquisition Report [R10] for both ground-range and cross-range directions, relatively to data processed from missions M1 and M2. The analyzed datasets have been acquired with a transmitted bandwidth of 50 MHz and processed with a Doppler bandwidth of 125 Hz. It results a theoretical *slant* range resolution of 4 m. The *ground* range resolution degrades according to the look angle, so resolution at far range is lower than resolution at near range. The theoretical *azimuth* resolution is 0.55 m.

Results for M2 are summarized in Table 8-4 and Table 8-5. The ground-range resolution is basically matching with the theoretical one, the azimuth resolution is ~1 m, against the 55 cm of the theoretical one. Random misalignments in the order of 0.5 m can be noticed sometime in both monostatic and bistatic cases, probably due to residual motion errors of the navigation data. (See [R10] for other missions).

	C1 (4.81)	C2 (5.64)	C3 (6.34)	C4 (7.13)
M-VV	5.4	6.4	7.0	7.5
M-HH	5.8	7.4	7.4	8.6
B-VV	5.4	6.3	7.0	7.4
B-HH	5.3	6.7	6.7	7.2

**Table 8-4 Ground-range resolution [m] estimated from IRF analysis of the four corners processed from data acquired during M2, for different polarization schemes The theoretical resolution is given in parenthesis for each corner .**

	C1 (0.52)	C2 (0.52)	C3 (0.52)	C4 (0.52)
M-VV	1.0	0.7	0.7	0.7
M-HH	0.9	0.4	0.4	0.4
B-VV	0.7	0.9	0.7	0.4
B-HH	0.9	0.7	0.6	0.6

**Table 8-5 Azimuth resolution [m] estimated from IRF analysis of the four corners processed from data acquired during M2, for different polarization schemes The theoretical resolution is given in parenthesis for each corner.**

## BelSAR Campaign 2018 Final Report

### 8.8 Additional Comments for further Interferometric Processing

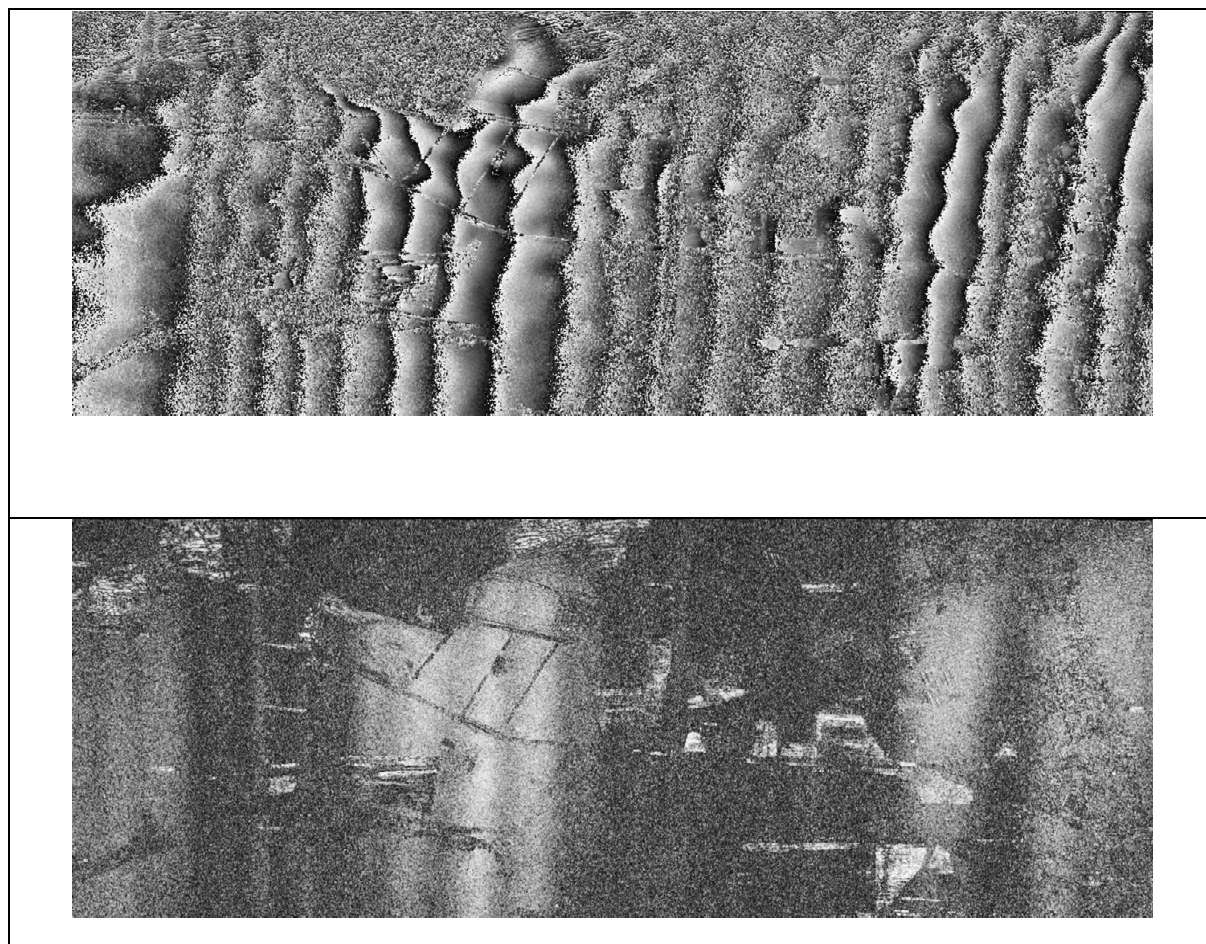
The focusing quality, geo-location and co-registration accuracies of the processed SLC SAR images can be affected by errors on the navigation post-processed data (residual motion errors) and/or mis-synchronization issues in the case of the bistatic data. In principle, the data have been geometrically calibrated based on the corner reflectors location in the image. As shown in the previous chapter, the external calibration accuracy is within 0.75m. Therefore, the standard deviation of the geo-location errors as well the co-registration errors among the images are expected to be below the pixel size of the image, which is 1m.

For amplitude-based application (polarimetric analysis for example), the pixel size accuracy shall be enough. For interferometric application, it is necessary to achieve sub-pixel co-registration, typically in the order of 0.1 pixels.

In the current delivery data set, sub-pixel co-registration can be achieved, for example, through amplitude-based co-registration in patch-by-patch basis. Advanced techniques like multisquint for residual baseline estimation can be also used enabling better results. In both cases, the spatial variability of the co-registration errors due to residual motion errors or/end mis-synchronization issues must be taken into account.

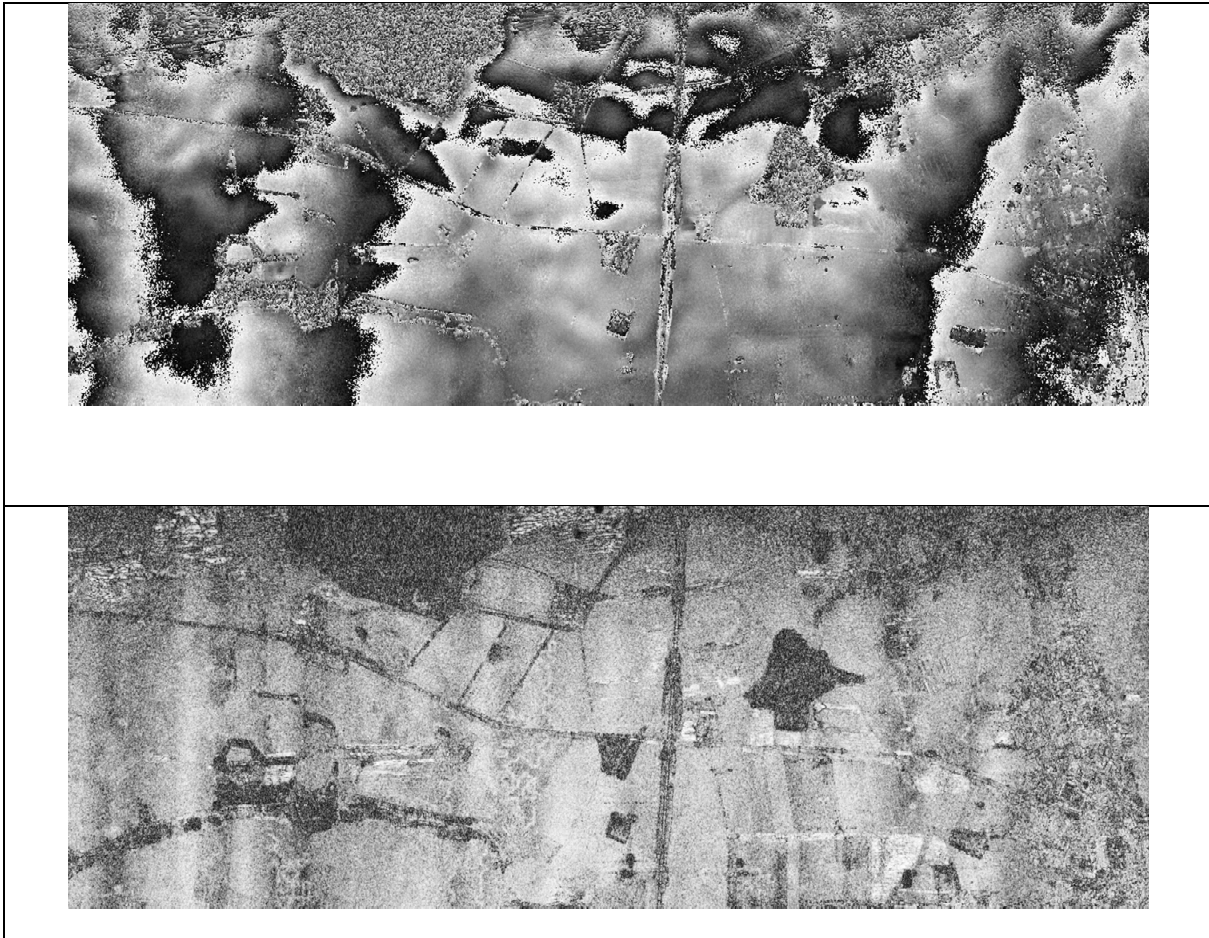
As an example, Figure 8-10 shows the bistatic interferometric coherence between two BelSAR images. The master image is the SAR\_CPLX\_20180530155510\_2\_1.4G\_VV\_12\_pres\_8\_fdc\_0.sar.tmb.rgo.tmr, the slave image is the SAR\_CPLX\_20180530155510\_2\_1.4G\_VV\_22\_pres\_8\_fdc\_0.sar.tmb.rgo.tmr.

Figure 8-10 shows some loss of coherence due to residual motion errors and mis-synchronization issues. These errors cause mis-registration and low frequency phase undulations in the interferogram. The main linear phase term causes a constant mis-registration offset along track direction of  $\sim 0.6$  m. This is being caused mainly by a linear phase variation due to mis-synchronisation between the transmitter and receiver clocks.



**Figure 8-10 Phase (top) and coherence (bottom) between two delivered BeISAR images.**

In order to improve the coherence, an amplitude-based co-registration method was applied (only in the along-track direction), optimizing the coherence for each small patches of 32 x 32 pixels and resampling the SAR data accordingly. The phase main undulations were filtered by removing the peak response of the spectrum of the complex interferogram. The obtained phase and coherence are shown in Figure 8-11.



**Figure 8-11 Phase (top) and coherence (bottom) between two delivered BelSAR images after coherence optimization and phase filtering.**

Figure 8-12 shows how the BelSAR data can be post-processed in order to enable interferometric analysis. This block diagram also shows how this post-processing step interfaces with the current processed data output. Note that the output of this post-processed step are interferometric data pairs, since the correction and compensation of residual mis-registration errors are relative to a master image.

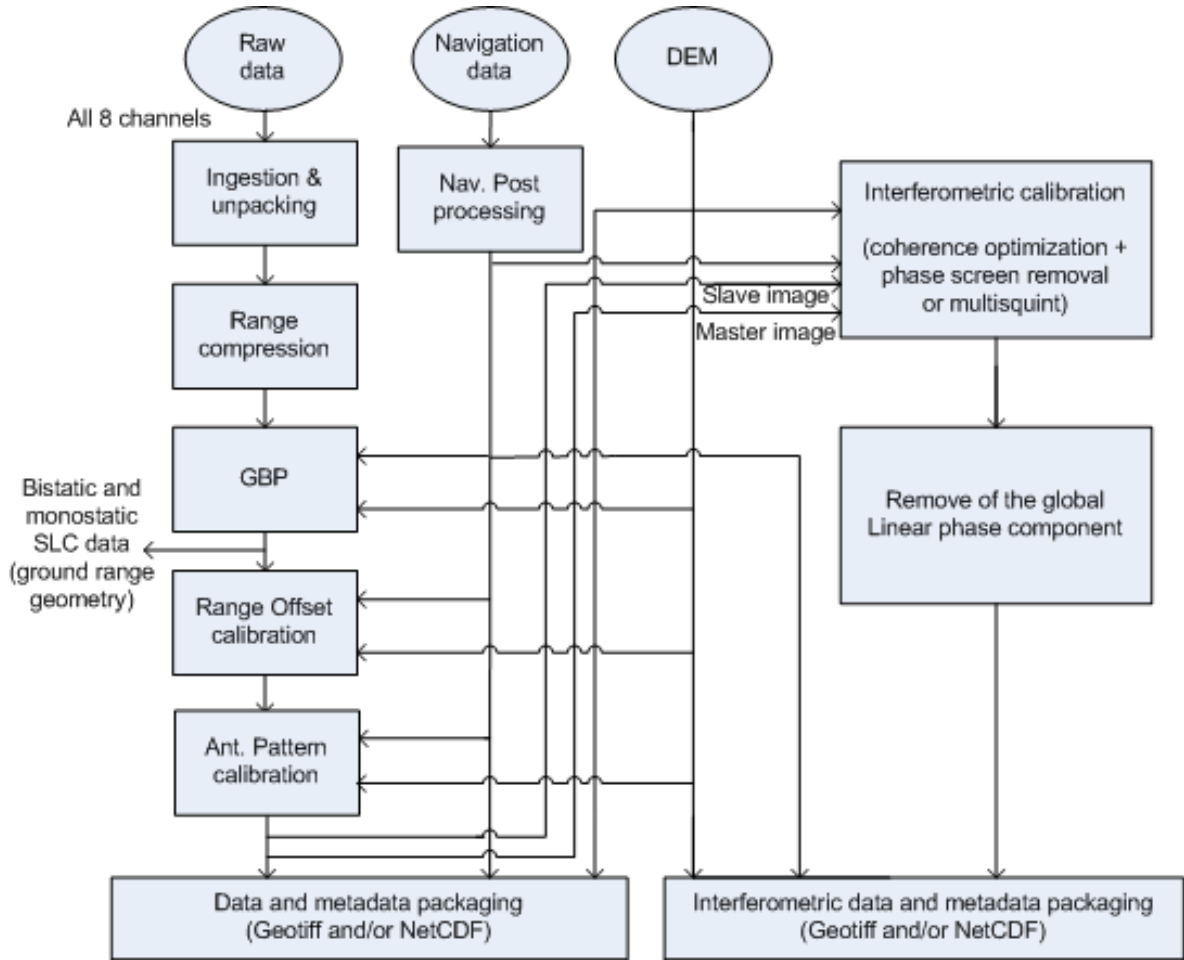


**Figure 8-12 SAR processing and post-processing for interferometric analysis on BeISAR data.**

## 8.9 Conclusion

From a preliminary data analysis performed on data sample acquired during each mission, it can be concluded the successful finalization of the campaign. Both radar and navigation data looks healthy and in good shape for further processing. In particular, post-processed navigation data shows the expected accuracies. The NESZ analysis showed a better performance of bistatic images w.r.t. monostatic ones, due to coupling effects. MetaSAR-L2 overperformed MetaSAR-L1. IRF analysis showed comparable resolutions for monostatic and bistatic cases, both close to theoretical values, showing a good focusing processing. Additional information for interferometric processing is provided.

## BelSAR Campaign 2018 Final Report

## 9 Bistatic SAR Science

### 9.1 Data with ground-range misalignment

#### 9.1.1 Data and selection of scatterers

An analysis of the effects (such as geometric distortion) on the SAR images resulting from mis-synchronization between the transmitter and receiver clocks was performed.

The first set of data used for this analysis consisted of the first version of the SAR images uploaded on 2018-06-22 on the shared server DoX-ULiège, i.e. a cross-track scenario from the first mission (M1, 2018-05-30), and more specifically the monostatic and bistatic SAR images corresponding to the VV polarisation scheme.

A dozen of scatterers were selected and their respective ground-range and cross-range coordinates were compared between the monostatic and bistatic SAR images. For illustration purposes, two different scatterers were drawn in both monostatic and bistatic SAR images and ground-range misalignment of about 17 and 28.5 [m] respectively could be noted (see Data Acquisition Report [R10]).

After computing the coordinates' differences between both images, it was observed that ground-range displacements are higher than cross-range displacements and that these displacements decrease with increasing ground-range.

#### 9.1.2 Analysis of the ground-range misalignment

Theoretical considerations showed that a constant frequency offset ( $\delta f$ ) between the transmitter and receiver clocks leads to a constant temporal shift (or delay, equal to  $\delta f/\alpha$  where  $\alpha$  is the chirp rate) in the impulse response, or equivalently to a constant bistatic range shift, but to a variable ground-range shift.

By fitting the theoretical ground-range shift function to the experimental data points, the delay was estimated to be 100 ns, which could be due to a constant frequency offset ( $\delta f$ ) between transmitter and receiver clocks.

As a matter of fact, that delay was determined to be due to a hardware issue and resolved. Indeed, the ground-range shifts noted between more recent [BI]SAR images (uploaded on 2018-10-09, with filenames including an additional “.rgo” extension) and monostatic images was zero.

### 9.2 Analysis of random phase noise effects in the azimuth direction

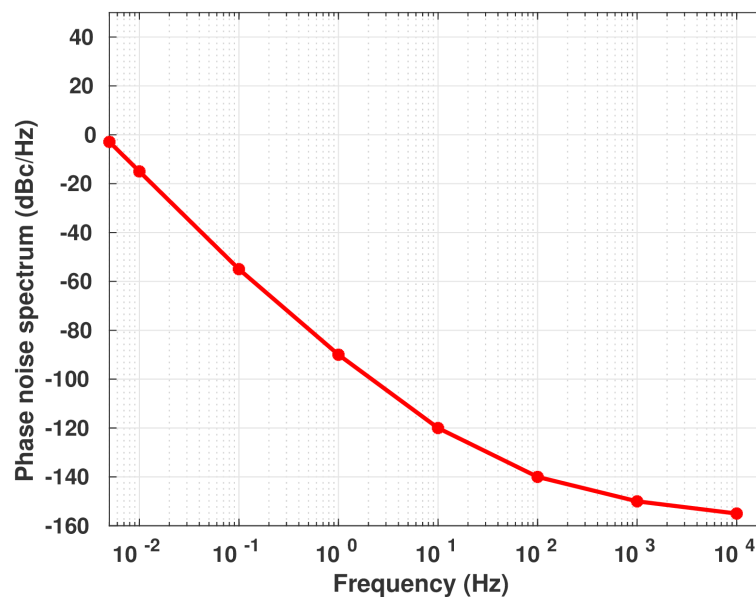
#### 9.2.1 Introduction

Besides the constant frequency shift between the oscillators at transmitter and receiver, responsible for a linear phase drift, typically leading to a shift in the azimuth (i.e. along-track) direction, these oscillators also have a limited stability during SAR data acquisitions. In contrast to monostatic SAR

systems using the same oscillator for both modulation and demodulation, bistatic SAR systems use two different oscillators, preventing any direct cancellation of low-frequency phase errors. As a result of residual low-frequency and high-frequency phase errors, the quality of the focussed SAR image is degraded, due to the deformation of the bistatic impulse response (broadening of the main lobe and/or increase of the side lobes) [R08]. This degradation can be evaluated by means of the ISLR (Integrated Side-Lobe Ratio), the ratio between the energy in the impulse response side lobes and the energy in the main lobe. This ISLR value can be considered as a measure of the ability to detect weak targets in the neighbourhood of strong targets.

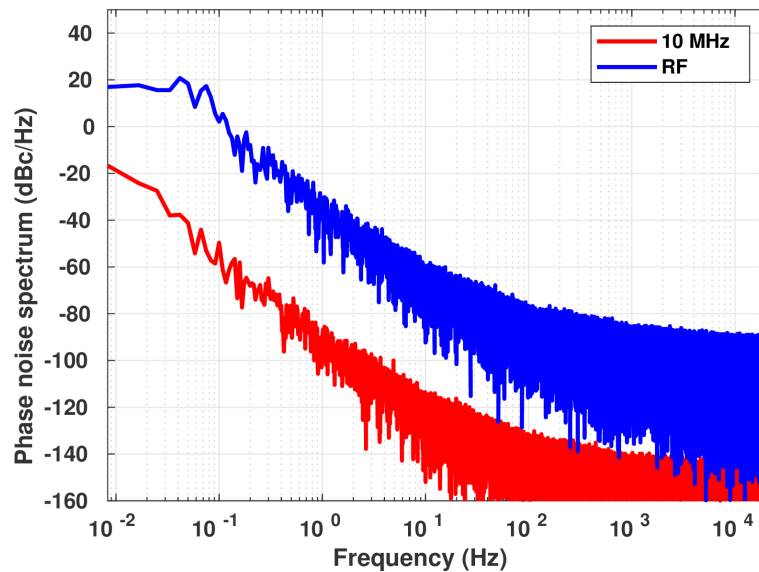
### 9.2.2 The random phase noise model

Random phase noise can be modelled by a second-order stationary stochastic process. The power spectral density of the oscillator phase noise is assumed to obey a composite power law model combining contributions from random walk frequency noise, frequency flicker noise, white frequency noise, flicker phase noise, and white phase noise [R09]. Assuming uncorrelated oscillators with equal phase spectrum at transmitter and receiver, the power spectral density of the bistatic phase noise in the RF band can be deduced by multiplying the power spectral density of the oscillator phase noise by  $2m^2$  where  $m = f_0/f_{osc}$  is the frequency up-conversion factor from the local oscillator frequency ( $f_{osc} = 10\text{MHz}$ ) to the radar carrier frequency ( $f_0 = 1.375\text{GHz}$ ). Note that an increase by a factor 2 of this frequency up-conversion factor leads to an increase of 6 dB of the power spectral density of the bistatic phase noise in the RF band. A phase noise spectrum similar to that provided as a representative example of ultra-stable oscillator by Krieger and Younis (2006) [R09] was used as a reference, as shown in the next figure.



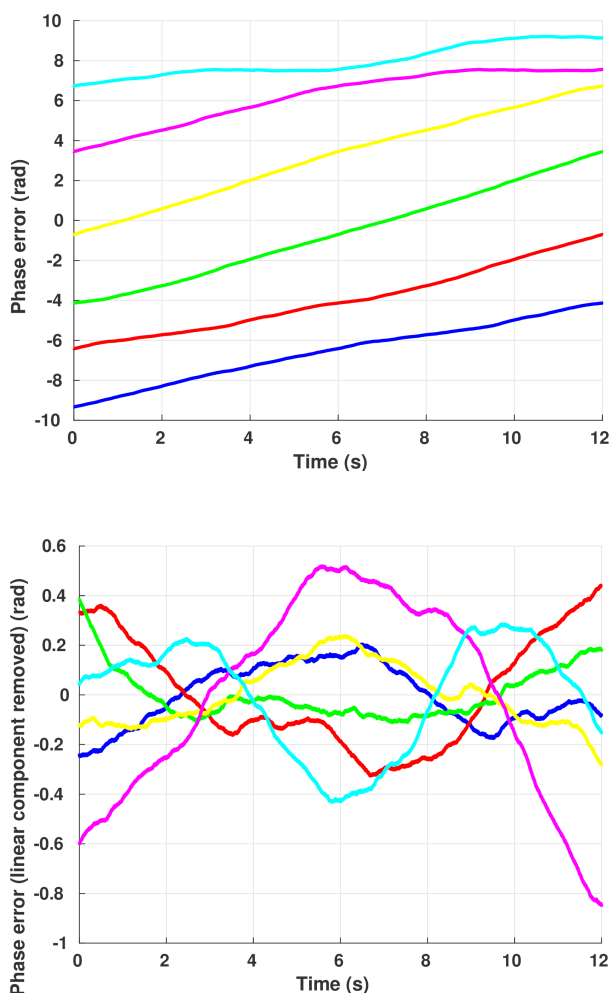
**Figure 9-1 Reference phase noise spectrum**

Figure 9-2 below illustrates stochastic realisations of the phase noise spectrum, both for the local oscillator (at 10 MHz) and the RF signal (after frequency up-conversion to the carrier, at 1375 MHz). An increase of about 46 dB can be observed.



**Figure 9-2 Stochastic realisations of the phase noise spectrum for both the Local Oscillator and the RF signal**

Following computations and illustrations were obtained by considering parameter values close to those used during the acquisition campaign. For instance, the realisations of the phase noise were generated from the stochastic process defined above. The first 6 realisations are plotted below, as raw sequences on one hand, and after removal of the linear component on the other hand.



**Figure 9-3 Phase error sequences for different stochastic realisations of the phase noise  
(a) as raw sequences, (b) after removal of the linear component**

### 9.2.3 Analysis

The cross-track scenario with a 'typical' baseline of 25 m was considered, with a flight altitude of 2000 m and a velocity of 50 m/s for both aircrafts.

The deformation of the (bistatic) azimuth IRF (Impulse Response Function) is illustrated below for different realisations of the phase noise, allowing the comparison between the ideal noise-free curve and the contribution of the phase noise without the linear component, in the cross-track scenario, using a coherent integration time equal to 12 s (corresponding to a Doppler bandwidth of about 120 Hz, thus close to the value of 125 Hz mentioned in the Data Acquisition Report [R10]). Note that no apodisation was performed (i.e. a rectangular window was used).

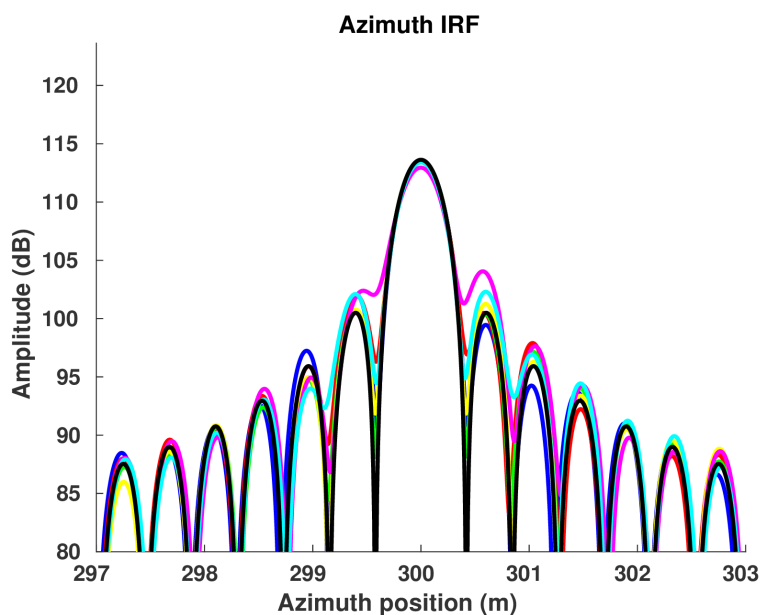


**Figure 9-4 Azimuth IRF for successive stochastic realisations of the phase noise after removal of the linear component from the phase noise error (plotted in color), compared to the ideal (noise-free) azimuth IRF (plotted in black)**

#### 9.2.4 Simulations and results

Simulations were performed with different values of the coherent integration time, as well as different values of additional phase noise, allowing the comparison of other frequency up-conversion factors and/or oscillators characterised by a similar phase noise spectrum as the representative example used as a reference, but at a globally higher level of all components. The evolution of the mean value of the ISLR, as well as its standard deviation, with these parameters is shown in the figures below.

Not surprisingly, the ISLR values are degraded with increasing additional phase noise; indeed, both the mean and the standard deviation values of the ISLR measure are increased, as can be observed in the next figure, generated by using the same coherent integration time equal to 12 s as above. Whereas the 'reference' (noise-free) ISLR value is -10.6 dB, the mean value of the ISLR increases from -8.7 dB up to -3.4 dB when applying an additional phase noise level of 10 dB w.r.t. the reference phase noise spectrum defined before.

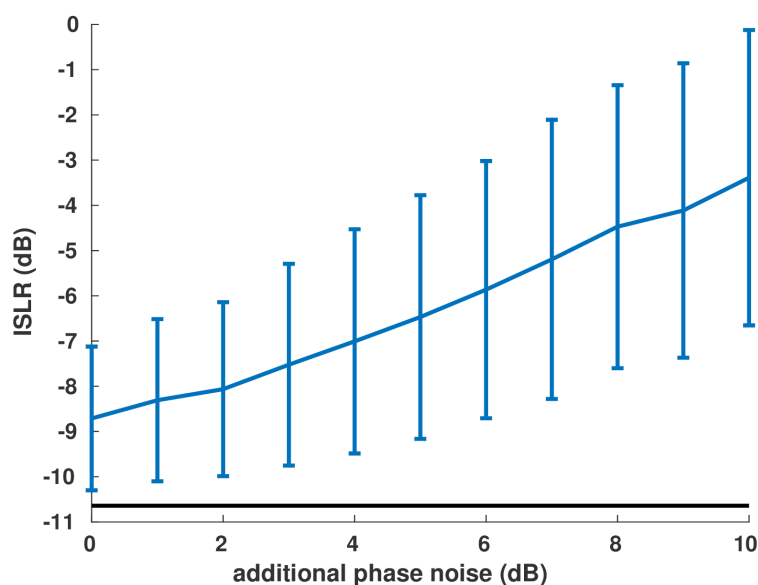


**Figure 9-5 Evolution of the ISLR in function of the additional phase noise level (mean and std value), the black curve illustrates the ISLR in the absence of phase noise.**

Also, the ISLR values are degraded with increasing integration time; indeed, both the mean and the standard deviation values of the ISLR measure are increased, as can be observed in the figures, generated without additional phase noise (i.e. 0 dB) w.r.t. the reference phase noise spectrum defined before.

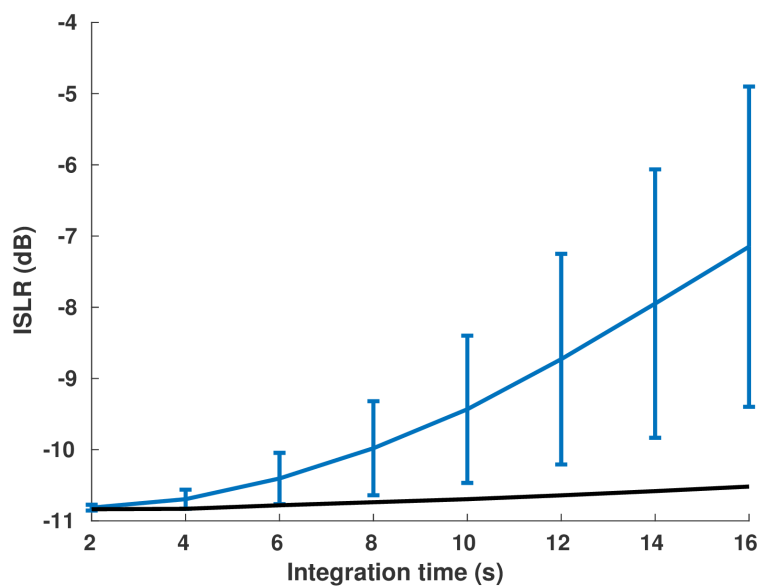


**Figure 9-6 Evolution of the ISLR in function of the coherent integration time (mean and std value), the black curve illustrates the ISLR in the absence of phase noise.**

## BelSAR Campaign 2018 Final Report

It can also be observed from this figure that the standard deviation values of the ISLR with random phase error are of the same order of magnitude as the increase of the corresponding ISLR mean values w.r.t. the 'reference' (i.e. noise-free) values. For instance, with a coherent integration time of 12 seconds, the mean value of the ISLR with random phase error is about -8.7 dB whereas the 'reference' (noise-free) ISLR value is -10.6 dB (cf. Figure 9-6 above); so the increase of the ISLR mean value is 1.9 dB, compared to a corresponding standard deviation value of 1.4 dB (see Figure 9-6).

### 9.3 Conclusions

An analysis was performed to measure the effects (like geometric distortion) on the SAR images resulting from mis-synchronization between the transmitter and receiver clocks, as well as from random phase noise due to the limited stability of the oscillators.

Clock synchronization problems can be detected on the basis of the SAR images. In practice, the comparison between a first set of monostatic and bistatic SAR images revealed a ground-range misalignment of the selected scatterers, due to a hardware-related constant delay estimated to be 100 ns.

Furthermore, simulations showed the impact of random phase noise on the ISLR, as well as the influence of the coherent integration time, though an experimental evaluation was not performed yet.

## BelSAR Campaign 2018 Final Report

## 10 Interferometric Processing

CSL was tasked to process the images provided by MetaSensing and provide coherence maps to the consortium for further analysis. The present chapter describes the processing tools developed for that purpose, illustrates the results with specific examples, and briefly discusses the origin of the loss coherence observed in several interferometric pairs. The chapter ends with a description of the output files and a few recommendations for future work.

### 10.1 Description of data sets

The images were obtained at a central frequency of 1.375 GHz and with a bandwidth of 50 MHz, corresponding to a slant range resolution of 3 m. The latest release of the data provided by MetaSensing consisted of NetCDF files in ground range format with a ground resolution of 1 m (see [R06]). The files are divided among the five different missions and two different acquisition modes (AT or XT). For each mission and acquisition mode, four different tracks were obtained with two planes. Accounting for the four different polarizations, this amounts to a total of  $5 \times 4 \times 4 \times 2 \times 2 = 320$  files. The images were focused SLC and already co-registered. The coregistration was based on the absolute position accuracy of the navigation data, which is around 0.75 m (less than pixel size). In addition, the phase related to the distance between the target and the sensor was removed from the phase information of a given pixel (i.e., the interferometric phase between two images is already flattened).

### 10.2 Data processing

Data processing was performed using a python code developed by the SAR group at CSL specifically for this project [R10]. The code reads the images and metadata, performs a global coregistration, crops the master and slave images to match each other, performs Gaussian filtering, and computes a series of outputs relevant for diagnostics and InSAR analysis (e.g., coherence, interferogram). The latest version of the code is fully automatized in order to process all the interferometric pairs efficiently (e.g., 80 image pairs for a given master mission).

### 10.3 Example of results

This section presents the main output produced by the python code for the following monostatic pair: mission 5 as master and mission 4 as slave, AT, track A, and polarization HH. To be specific, the files considered for this example are named:

- MASTER: SAR\_ATI\_20180910152210\_2\_1.4G\_HH\_41\_pres\_8\_fdc\_0.sar.tmb.rgo.tmr.sig.nc
- SLAVE: SAR\_ATI\_20180828152409\_2\_1.4G\_HH\_41\_pres\_8\_fdc\_0.sar.tmb.rgo.tmr.sig.nc

The amplitude image for each file is shown in Figure 10-1 while the corresponding coherence map and interferometric phase are shown in Figure 10-2. The amplitude images are smoothed over 20 pixels

for noise reduction and the coherence maps are computed assuming a multi-looking parameter of 20 pixels.

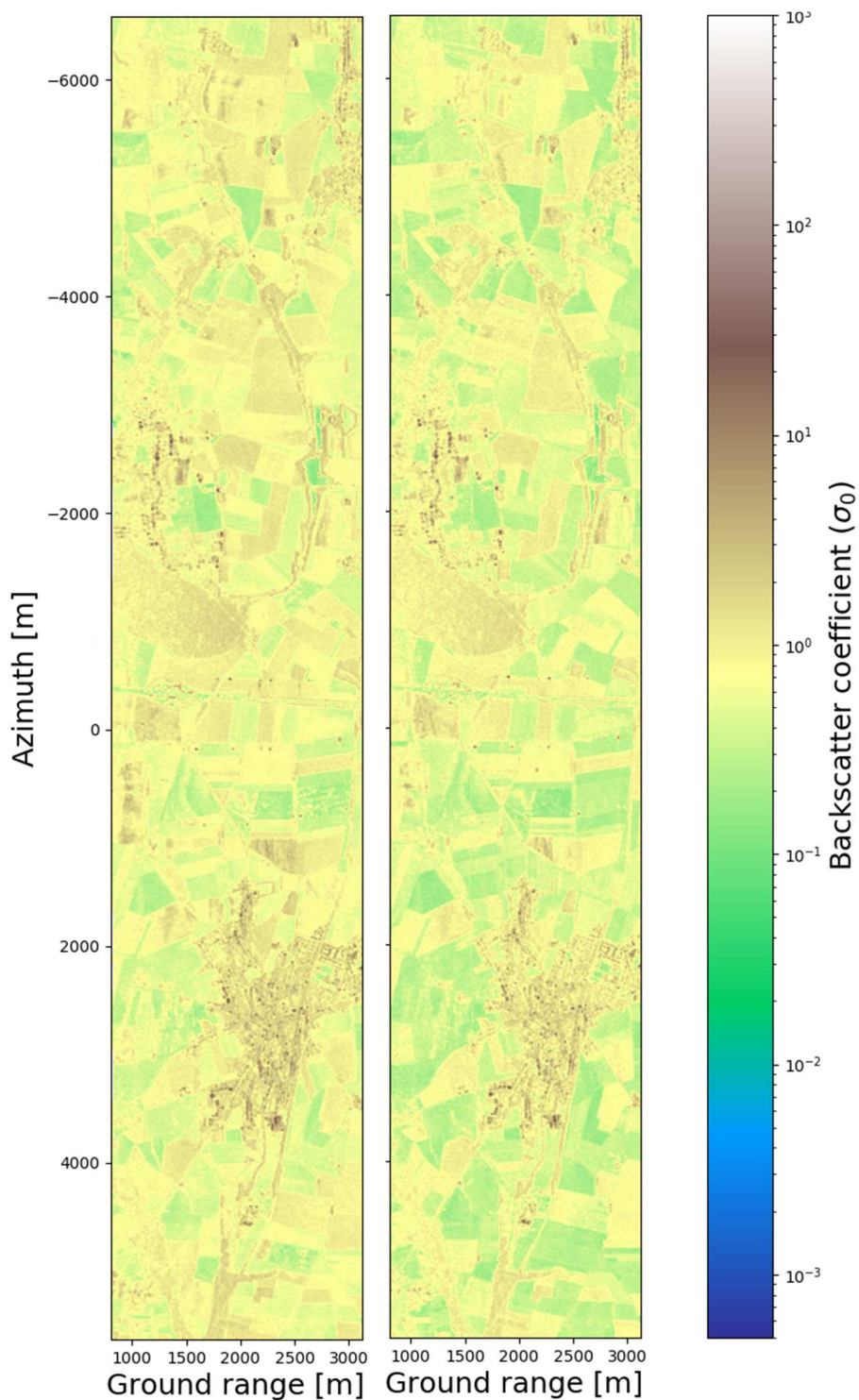


**Figure 10-1 Example of co-registered master (left) and slave (right) backscatter coefficient images (mission 5 as master and mission 4 as slave, AT, track A, and polarization HH).**

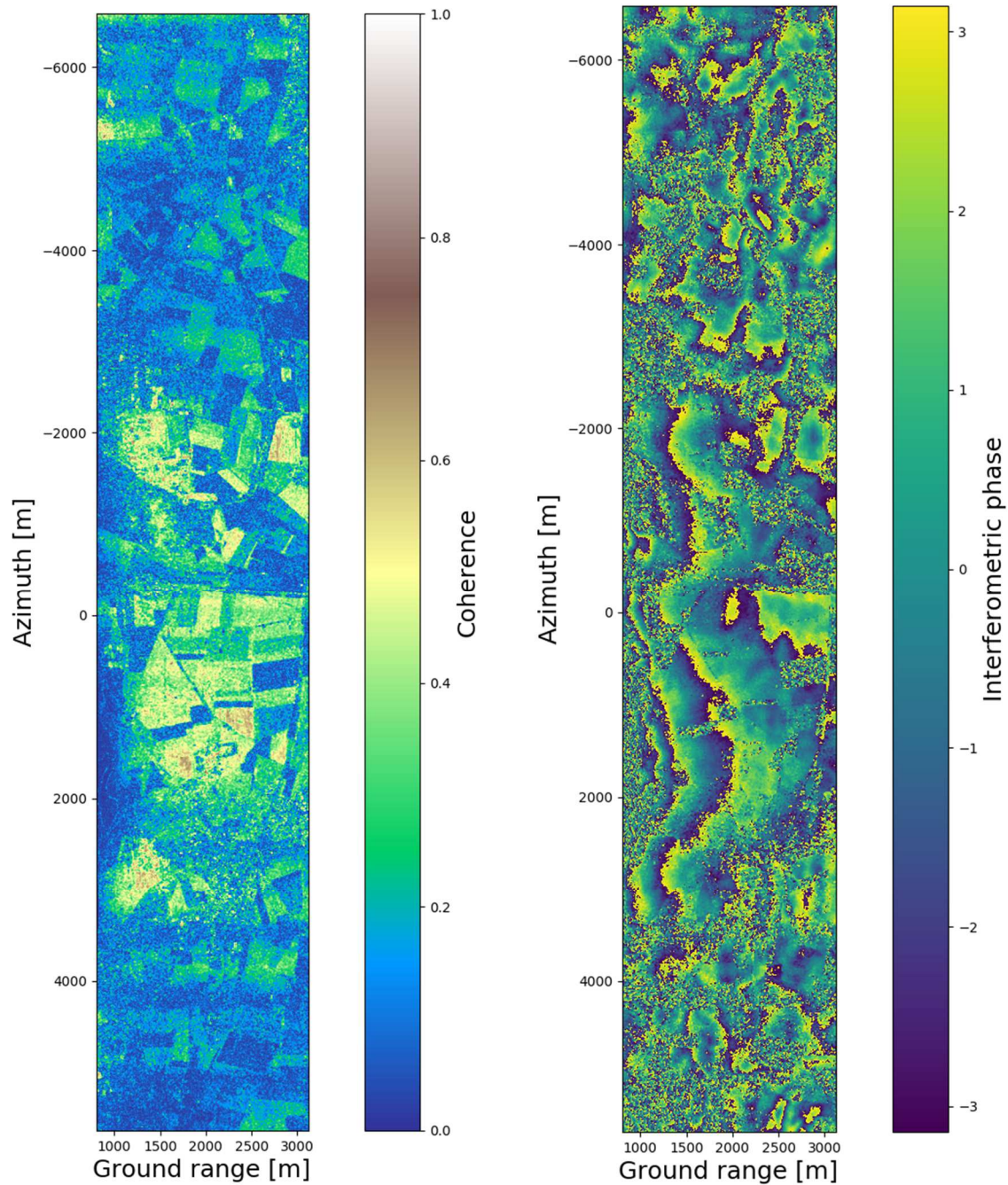


**Figure 10-2 Coherence map (left) and interferometric phase (right) for the image pair shown in Figure 10-1.**

## 10.4 Temporal loss of coherence

Figure 10-3 shows the coherence maps computed for the same master image (mission 5, XT, track A, polarization HH) and the corresponding slave images in the four other missions. The temporal loss of coherence is obvious and makes the image pairs taken far apart hardly usable.

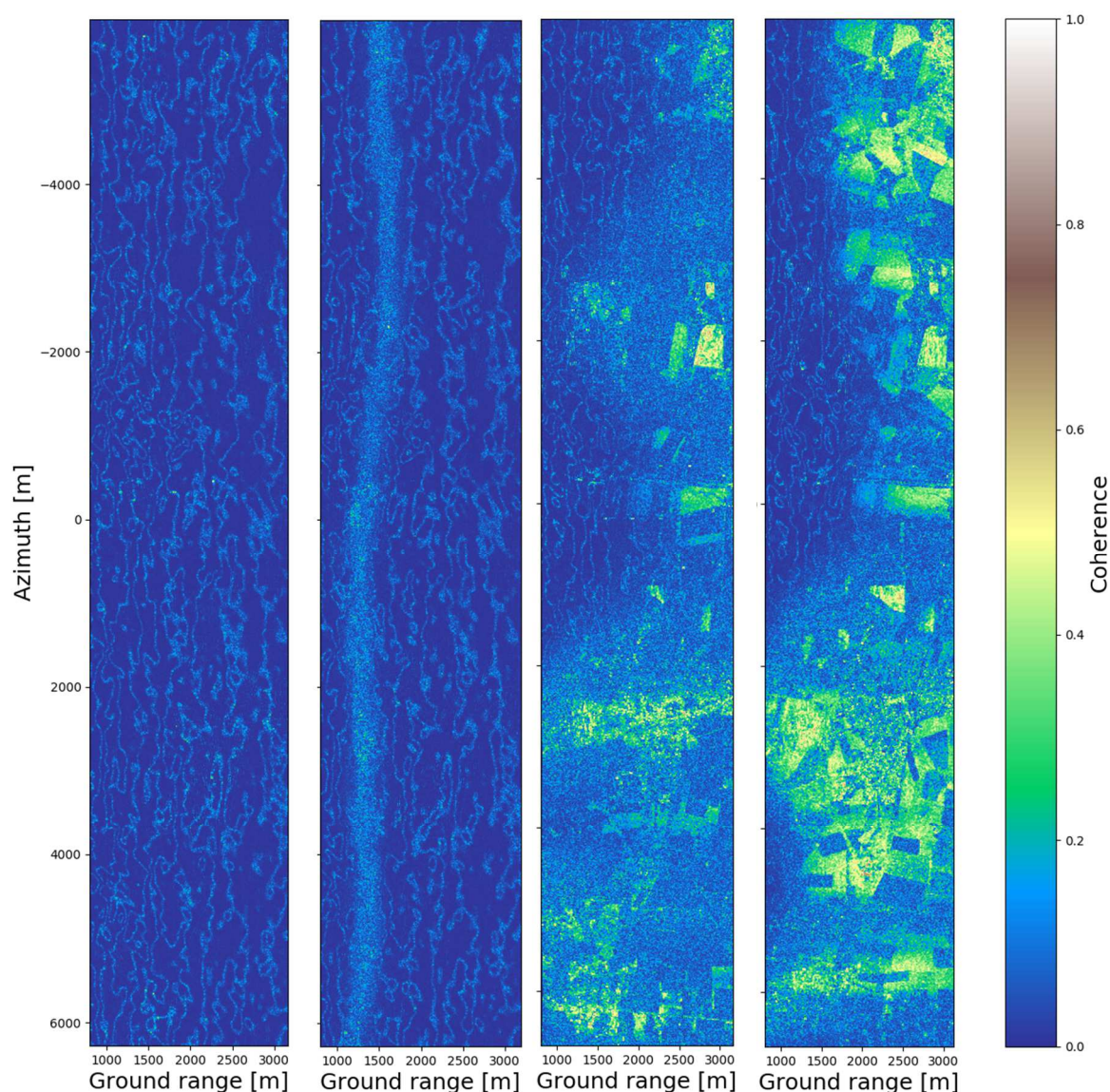


**Figure 10-3 Coherence map for the same master image (mission 5, XT, track A, polarization HH) and the corresponding slave images for the four other mission (1 to 4 from left to right), illustrating the strong temporal loss of coherence.**

## 10.5 Geometric loss of coherence

Figure 10-4 (left) shows the coherence maps for the following image pair: mission 1 (master), mission 2 (slave), XT, short track, polarization HH. The level of coherence is clearly correlated with the geometric decorrelation as illustrated by Figure 10-4 (right). As a reminder, the geometric decorrelation ( $gd$ ) occurs as the separation between the two plane trajectories increases (i.e., it is inversely proportional to the perpendicular baseline component):

$$gd = 1 - bp/bc$$

where  $bp$  is the perpendicular baseline and  $bc$  the critical baseline. A perpendicular baseline map is also produced by the code but not shown here.

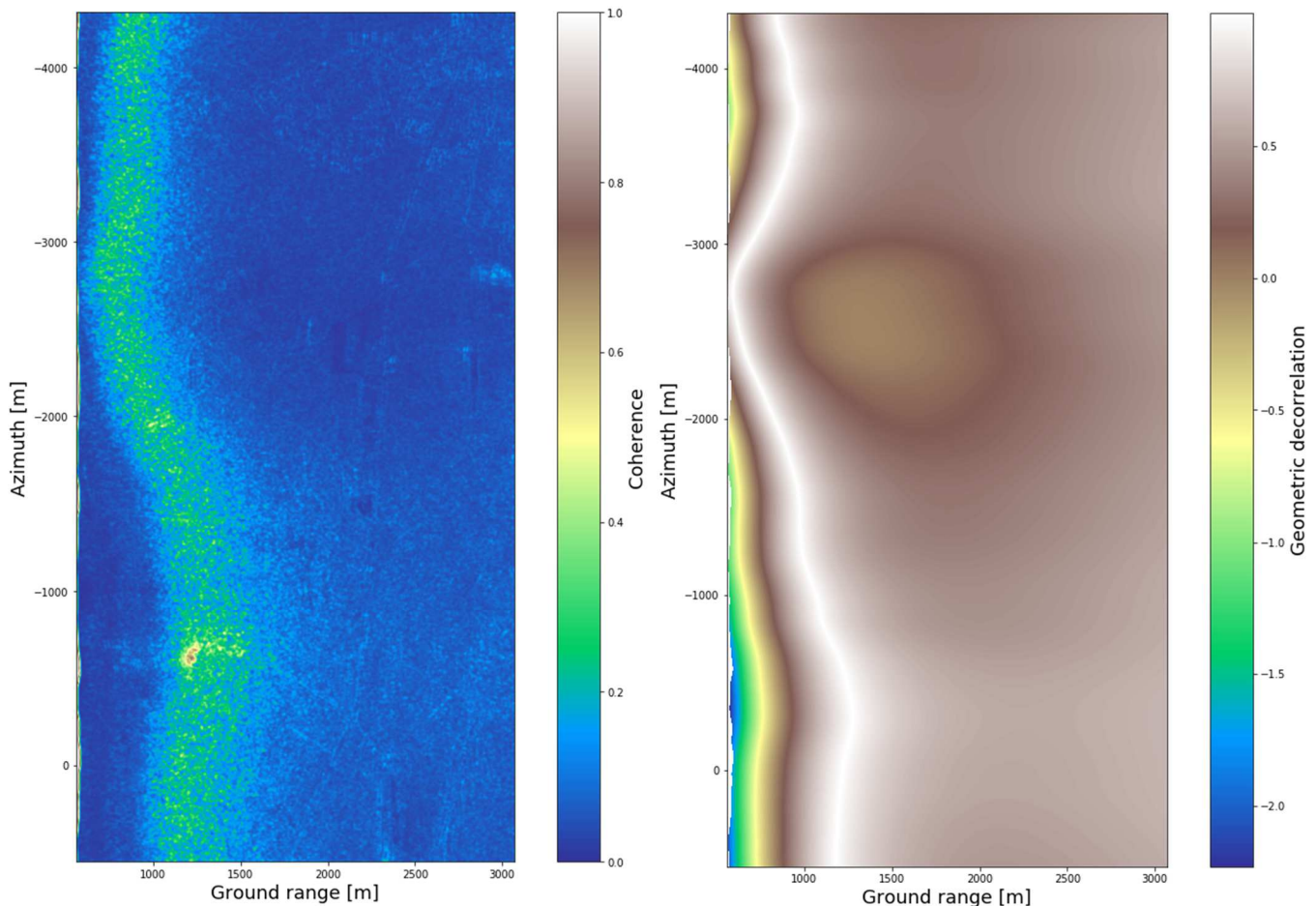


**Figure 10-4 Coherence map (left) and corresponding geometric decorrelation (right) for an example interferometric pair (mission 1, mission 2, XT, short track, polarization HH). The loss of coherence is clearly related to the geometric decorrelation, caused by the large perpendicular baseline**

	<b>BelSAR Campaign 2018</b> <b>Final Report</b>		Doc.	RP-CSL-BEL-19003
			Date	10/08/2019
			Issue:	1.1
			Page:	<b>63 of 103</b>

## 10.6 Output data and file format

For each image pair, the python code produces the following files described below:

- The amplitude images for the master and the slave acquisition (\*\_AMPL);
- The amplitude images for the master and the slave acquisition (\*\_PHASE) ;
- The corresponding coherence map (\*\_COH);
- The interferometric phase map (\*\_PHASE);
- The baseline map (\*\_BASE).

The amplitude images and coherence maps are provided in two formats (*png* and *tif*). The file naming convention is as follow:

**Mxy\_A(X)TI\_mode-x\_date-x\_pol-x\_mode-y\_date-y\_pol-y**

where

- **x, y** are the mission number of the master and slave image respectively;
- **mode** is the acquisition mode (SAR for double-pass monostatic, BISAR for single-pass bistatic);
- **date** is the date and time at which the data have been acquired (yyyymmddhhmmss);
- **pol** is the polarization;
- **-x, -y** denote the master and slave image respectively.

Here is an example of file name for a master image obtained on September 10<sup>th</sup>, 2018 (mission 5) and a slave image obtained on May 30<sup>th</sup>, 2018 (mission 1), both in HH polarization.

**M51\_ATI\_SAR\_20180910152210\_HH\_SAR\_20180530161310\_HH\_BASE.png**

For this data release, we decided to consider images from mission 5 as the master image and computed all possible pairs with the other missions (double-pass monostatic case, files M51\*, M52\*, M53\* and M54\*) or with the other plane of the same mission (single-pass bistatic case, files M55\*).

## 10.7 Conclusions

The images provided by MetaSensing have been successfully processed and the results have been released to the BelSAR consortium. CSL developed a new python-based software to process the files and produce a series of outputs relevant for diagnostics and InSAR analysis. The analysis of the coherence maps showed a strong temporal coherence loss between the different missions as well as geometric decorrelation due to the relatively large perpendicular baseline. As a result, the coherence extracted from double-pass monostatic pairs is usually rather poor across the image. The results obtained from single-pass bistatic pairs will likely be more useful for further analysis.

Regarding future work, it would be particularly useful to remove the spatially-variable co-registration errors due to the residual motion of the airplanes and/or mis-synchronization issues. This

	<b>BeISAR Campaign 2018</b> <b>Final Report</b>		Doc.	RP-CSL-BEL-19003
			Date	10/08/2019
			Issue:	1.1
			Page:	<b>64 of 103</b>

---

could be achieved by amplitude-based co-registration in patch-by-patch basis or more advanced techniques such as multisquint (see also Section 8.8). Better phase filtering could also be considered in order to remove the main undulation component from the complex interferogram. Finally, it would be useful to geo-reference the *tif* images for easier comparison with other images.

## BeISAR Campaign 2018 Final Report

# 11 Ground measurements: Soil moisture and roughness

## 11.1 Hardware

The scattering of microwaves at a soil surface depends on the two surface properties, i.e. the dielectric constant of the top soil layer and the surface roughness. The dielectric constant of a soil depends on the soil moisture content and therefore makes the scattering process interesting to hydrologists. Unfortunately, the penetration depth of the signal depends on the frequency of the radar signal but is generally limited to a couple of centimeters. Furthermore, this penetration depth is also influenced by the moisture content of the soil. For developing or testing retrieval algorithms, soil moisture of the top soil layer is generally obtained, where the depth of measurement reflects the penetration depth. Often, observations of the top 5 to 10 centimeters are made, where the depth often depends on the measurement devices used. In this research, TDR (time domain reflectometry) measurements are put forward as these allow a fast monitoring. The instrumentation used is equipped with 11 cm pins that are quite robust such that they can easily be driven in the soil, such that the average soil moisture in the top 11 cm soil layer is measured. Per field, top layer soil moisture was measured at several places to ensure a good estimation of the field average soil moisture.

As stated above, the scattering process is also determined by the soil roughness. In this project, we opted for measuring the roughness with a 1-m pin profilometer as this allows for a fast monitoring. Per field several roughness measurements were made, and the average RMS height and correlation length were determined.

For both soil moisture and soil roughness, multiple measurements were made which allows for estimating the uncertainty upon the measurements.

## 11.2 Protocol

3 variables were monitored during the BeISAR campaign by LHWM (Ghent University):

- soil moisture
- soil roughness
- bulk density

### 11.2.1 Soil moisture measurement

The soil moisture was monitored using TDR (time domain reflectometry) probes having 11 cm pins. In this way, average soil moisture in the top 11 cm soil layer is obtained.

Top layer soil moisture was measured for at least 10 locations per field (if feasible) to ensure a good estimation of the field average soil moisture. At each measurement location, the soil moisture was determined as the average of 3 repetitions taken within a circle with a diameter of 1 m.

## BeISAR Campaign 2018 Final Report

### 11.2.2 Bulk density measurement

Bulk density was sampled using Kopecky rings. 5 samples were taken during flight 1 on all fields, allowing to determine field average and standard deviations. If during later flights the bulk density was changed due to tillage operations, additional samples were taken.

### 11.2.3 Soil roughness measurement

Roughness is determined using a 1-m pin profilometer, with a spacing of 1cm.

A picture of the profile along and across the rows of the crops were taken, which were digitized to correct for tilted pictures and to allow determination of correlation lengths and root-mean-square heights. Only field averages and standard deviations are available.

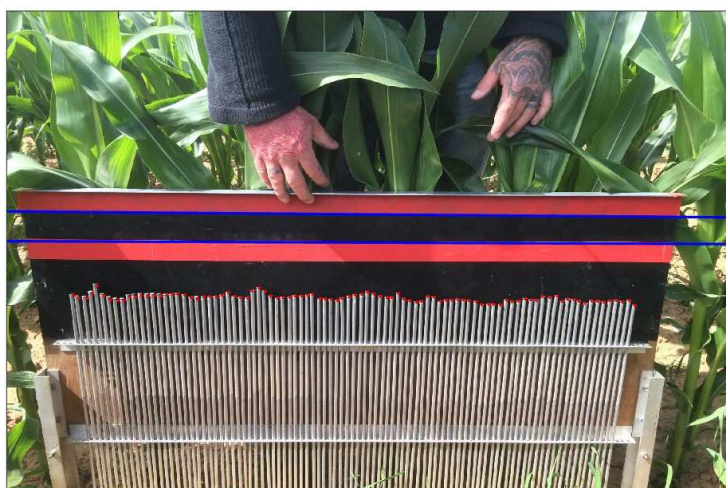


**Figure 11-1 1-m pin profilometer, with a spacing of 1cm**

Per field, at least 5 profiles were taken on each flight date and each orientation.

### 11.2.4 Error characteristics

For both soil moisture and soil roughness, several (>10) measurements were made which allow for estimating the uncertainty upon the measurements. Such exercise was only determined once per class of roughness (as determined visually). For soil moisture, such exercise was made at one field for each day of sampling.

## 11.3 Acquisition report

Figure 11-2 shows the field distribution in the BeISAR acquisition area.

For each mission, field measurements of soil moisture were taken with at least 10 collection points in each field, and 3 repetitions for each collection point. As an exception, three winter wheat fields were not sampled during Mission 1 due to time constraints. Despite sensor failure resulting in corrupted datafiles, coverage over all fields was obtained.

Roughness profiles were taken on all fields during Mission 1 and 2 in order to set a baseline of the roughness class to which each field is assigned. These profiles were collected at minimum five randomly-chosen locations in each field, with a profile along and across tracks at each location.

Roughness is assumed to stay constant during the growing season. During Missions 3-5, roughness profiles were only taken on fields that were harvested or operated on, thus changing the roughness characteristics. Maize fields could not be monitored during their growing season, resulting in missing values during flights 3, 4, and 5. Field W7 could not be monitored during flight 4 due to tillage operations at the moment of the flight.



**Figure 11-2 Fields distribution for soil moisture and roughness measurements**

Bulk density measurements were performed on each field during Mission 1 by taking 5 samples randomly spread across the field. Similar to the roughness profiles, bulk density is assumed to stay

constant during the growing season if the conditions on the fields don't change (e.g. no harvesting, no severe storms etc.). Therefore, bulk density measurements were only repeated on fields that were harvested during the campaign, and on a limited set of field operated on by the farmer after harvesting in later missions. On these fields, three repetition-samples were taken during the first mission after harvesting, assuming that the conditions remain constant for the following missions.

Recorded data are organized as follows:

- BeISAR\_soil\_bulkdensity\_database
- BeISAR\_soil\_moisture\_database
- BeISAR\_soil\_roughness\_database
- Coordinates fields

Databases group all the measurements in xlsx files.

Soil moisture	Roughness	Bulk density
<ul style="list-style-type: none"> <li>• Volumetric soil moisture per field</li> <li>• 5 missions</li> <li>• All fields (except Mission 1)</li> <li>• Extremely dry → Low variability</li> <li>• Broken sensors → Quality check with precipitation</li> </ul>	<ul style="list-style-type: none"> <li>• Correlation length (L) and RMS (s) per field</li> <li>• All "changed" fields → Assumed constant during crop season</li> <li>• Maize: Mission 1, 2 + (4) + (5)</li> <li>• Winter wheat: Mission 1-5</li> </ul>	<ul style="list-style-type: none"> <li>• 5 per field</li> <li>• Mission 1</li> <li>• + All "changed" fields</li> <li>• Classification of fields</li> </ul>

**Table 11-1 Campaign summary – Soil moisture & roughness**

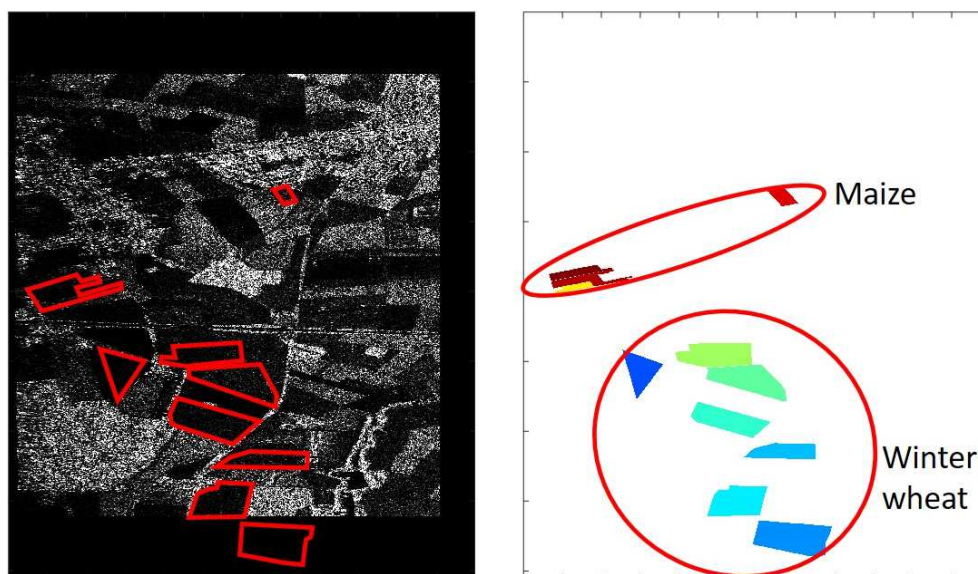
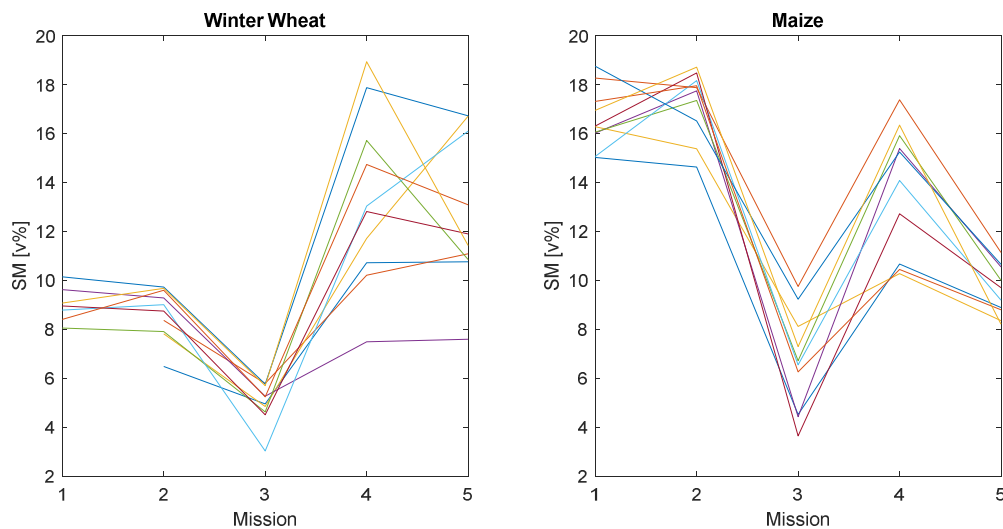


**Figure 11-3 Soil moisture & roughness acquisition areas**

## 11.4 Preliminary Analysis

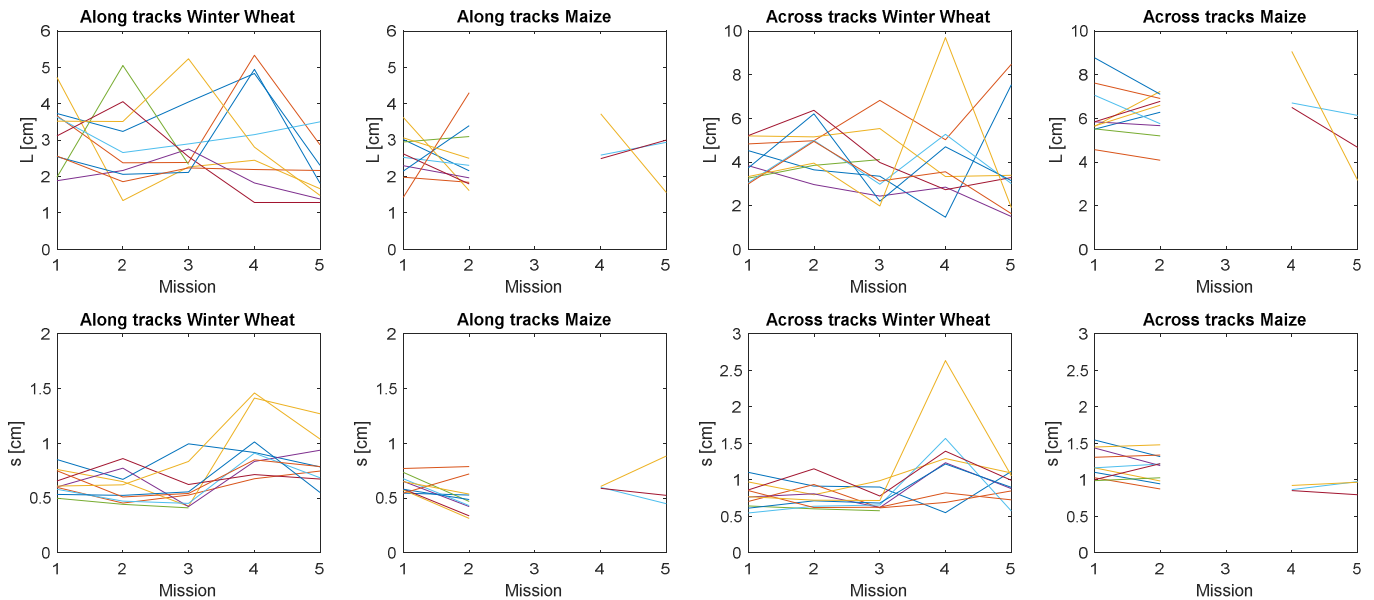
### 11.4.1 Data quality

Figure 11-4 shows the evolution of the soil moisture for all sampled fields during the acquisition period. As can be observed, field average soil moisture contents are low due to the 2018 summer drought. However, the similar behaviour of all fields over time indicate robust measurements.



**Figure 11-4 Field average soil moisture measurements for winter wheat (left) and maize (right) fields for the 5 missions. The different coloured lines represent different fields.**

Figure 11-5 visualise the roughness parameters over time during the acquisition period for all fields. Winter wheat fields were sampled during all field campaigns, while all maize fields could only be sampled during the first two campaigns, and some harvested fields during campaign 4 and 5. Overall, the fields show high inter-field variability, but also variability over time within fields due to changing surface conditions, either due to meteorological events (drought and extreme precipitation) or harvesting and/or ploughing practices.



**Figure 11-5 Field average roughness correlation length ( $L$ ) (top row) and root mean square variation ( $s$ ) (bottom row). For each vegetation type, along and across track measurements were taken. Different colours represent different fields.**

#### 11.4.2 Comparison radar versus bistatic radar

Figure 11-6 shows the relations between the observed signal for both radar and bistatic radar and the field properties (e.g. soil moisture and roughness). During the first campaign, the backscatter seemed to increase with increasing roughness correlation lengths (along track), both for radar and bistatic radar. However, the aim of this study was to assess if bistatic radar can complement the retrieval of soil moisture from normal radar. Therefore, differences should occur in the relations between the backscatter and soil moisture for radar and bistatic radar. Here, the largest divergences can be observed for cross polarization set ups (VH and HV), indicating that most might be gained in these polarizations.

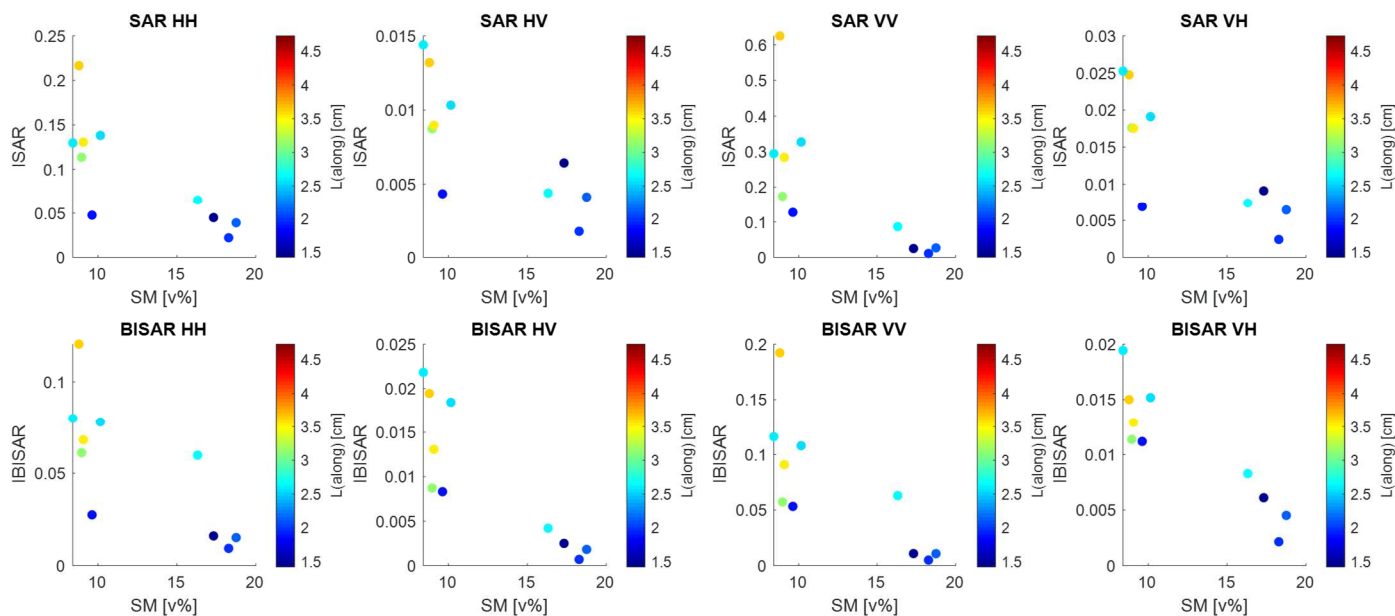


**Figure 11-6 Radar backscatter in function of soil moisture with roughness correlation length defining the colour of the dots for a selection of fields during campaign 1. Radar and bistatic radar are shown on top and bottom row, respectively.**

## BelSAR Campaign 2018 Final Report

## 12 Ground measurements: Agriculture

### 12.1 Hardware

As for the soil surface, the above ground plant canopy also influences the SAR backscattered signal. Both geometric and dielectric properties must be measured in-situ. The geometric canopy properties are characterized vertically by measuring the plant height and horizontally with the canopy cover fraction parameter.

The plant height is usually measured in-situ with a ruler. This very fast technique allows collecting a large number of records. A common technique for measuring the canopy cover fraction relies on vertical pictures recorded from top of the canopy and post-analyzed with an image processing software (such as the CANEYE MatLab application) in order to map the soil and plant areas. The required instrumentation consists in a hemispheric lens camera mounted on a 3-meter telescopic pole with a L-shape to approximate a nadir view from above the crop canopy and a computer with CANEYE application for picture post-processing and canopy cover fraction estimation (see Figure 12-2). The crop phenology is also recorded in-situ. For each in-situ measurement date, the crop development stage is noted following BBCH<sup>1</sup> codification by visual observation in the fields.

Dielectric canopy property is influenced by plant water content. This is a very important parameter for crop monitoring by SAR remote sensing. It is usually estimated by destructive measurement and drying in an oven. Such in-situ measurements must be performed as close as possible to the SAR acquisition time to avoid potential rain event between the image acquisition and ground measurement to affect the recorded field information. Moreover, this technique is very time consuming and a limited number of samples can be collected in a single field to guarantee the monitoring the 20 agricultural fields in a single day.

All the crop measured parameters are recorded on smartphone in an electronic form relying on ODK (open data kit) technology. At the end of the day the information is send to a dedicated server: <http://maps.elie.ucl.ac.be/belsar/odk/>. For each field, the average height and the uncertainty of the measurement can be provided for each bi-static SAR acquisition date.

### 12.2 Protocol

#### 12.2.1 Dataset 1

The crop type was recorded once for the growing season for the 5 main crop types (winter wheat, barley, maize, potato, sugar beet). A crop map was produced using this field survey and the field boundaries as derived from external sources. Circulating in the AOI with a GPS, the crop type was

---

<sup>1</sup> Biologische Bundesanstalt, Bundessortenamt und CHemische Industrie

recorded during the growing season. These geographic point locations were then converted to crop map using field boundaries delineated on a VHR satellite image.

### 12.2.2 Dataset 2

The second dataset consists in the properties of the crop canopy for a set of 10 winter wheat and 10 maize fields. Such variables were collected concurrently to the five aircraft overpasses. As the first fly was planned at end of May, maize fields had just been sown. In the same way, as the last fly was done in end August/early September, winter wheat fields were already harvested. In consequence, for each of both crop types, only four visits were planned to record the plant-related parameters (as shown in Figure 12-1). However, when grass or other green manure was still in place in May in the future maize fields, the plant parameters were recorded for this vegetation.

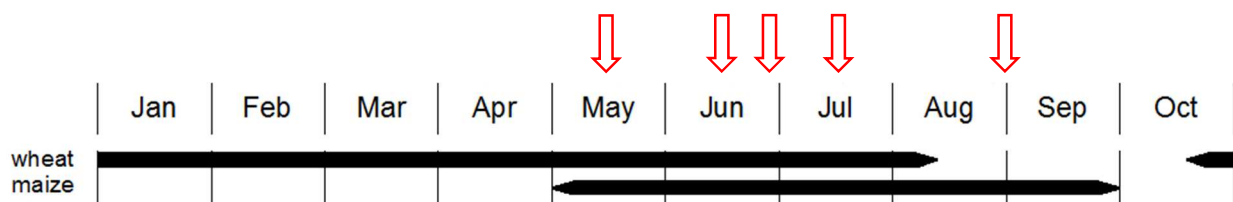


**Figure 12-1 Typical crop calendar for winter wheat and maize in the Hesbania site (Belgium). The black time lines represent the crop canopy presence. The red arrows represent the five bistatic acquisitions period**

#### 12.2.2.1 Recorded parameters

In order to characterize the crop canopy properties, the main plant **development stages** were recorded following the BBCH<sup>2</sup> codification. The **canopy cover fraction** was estimated using digital hemispheric pictures (DHP) are taken vertically acquired in the field from the ground using a digital camera mounted on a pole. These pictures were subsequently post-processed with the CANEYE software (Figure 12-2). **Plant height** was measured, in situ with a ruler and the **fresh and dry biomass** was measured by destructive sampling. The vegetative and reproductive plant parts were measured separately. Fresh biomass was measured in-situ while dry biomass was estimated after plant drying in oven (Figure 12-3). The **sowing density** was recorded once for the growing season in each field.

<sup>2</sup> Biologische Bundesanstalt, Bundessortenamt und Chemische Industrie

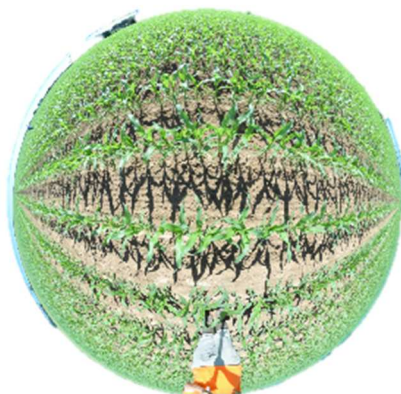


**Figure 12-2 Example of DHP picture in maize plot**



(a)



(b)

**Figure 12-3 (a) Biomass harvesting in maize plot and in-situ weighting of maize subsample and (b) Drying of subsamples in oven**

	<b>BeISAR Campaign 2018</b> <b>Final Report</b>		Doc.	RP-CSL-BEL-19003
			Date	10/08/2019
			Issue:	1.1
			Page:	<b>75 of 103</b>

#### 12.2.2.2 Sampling frame

The sampling frame had to allow an accurate estimation of the crop parameters average at the field level. A stratified approach was adopted to sample three different locations in each single field where three samples were collected. Both averages and standard deviations values were provided to characterize every single field concurrently to each flight campaign while crop canopy was in place.

#### 12.2.2.3 Field work cycle

Due to the large sampling frame density the plant parameters were not recorded on a single day in the 20 fields. Depending on their availabilities, two or three field operators were required during two or three consecutive days for each bistatic acquisition. Considering its fast variation in time, biomass is the parameter which has to be recorded the most simultaneous to the flight.

The first operator was responsible of the development stage and canopy cover. As the canopy should not have been altered before the cover fraction recording, the vertical picture was first taken. The plant development stage, eventually requiring plant manipulation, was then determined. Recording these two parameters in-situ for 20 fields required two working days. A third day was dedicated to the processing of the vertical pictures with CANEYE.

The second operator recorded the plan height and the biomass. While the first parameter is rather fast, the second is very time consuming as fresh biomass must be measured in-situ directly after plant cutting. Two working days were also required to records the 20 fields. Drying and weighting of the sample required a third day to the second operator.

When the third operator was present, the measures time could have been reduced to one day.

### 12.3 Acquisition report

All the in-situ data acquired during the field campaign are summarized in Table 12-1 below.

Flight	Date	Plant density	Canopy cover fraction (DHP)	BBCH development stage	Plant height	Biomass
	16/05					
F1cancelled	17/05	W1-W6	W1-W6	W1-W6	W1-W6	W1-W6
F1cancelled	18/05	W7-W10	W7-W10	W7-W10	W7-W10	W7-W10
<b>F1</b>	<b>30/05</b>					
	31/05	M1-M10	M1-M10	M1-M10	M1-M10	M1-M10
	05/06		W1-W10	W1-W10	W1-W10	W1-W10
<b>F2</b>	<b>20/06</b>					
	21/06		W1-W10	W1-W10 M2	W1-W10 M2	W1-W10 M2
	22/06			M1 , M3-M10	M1 , M3-M10	M1 , M3-M10
	26/06		M1-M10			
F3cancelled	18/07		M1-M10			
F3cancelled	19/07		W1-W7 (W8-W10 harvested)	W1-W7 (W8-W10 harvested)	W1-W7 (W8-W10 harvested)	W1-W7
F3cancelled	20/07					
F3cancelled	23/07					
F3cancelled	25/07					
F3cancelled	26/07					
<b>F3</b>	<b>30/07</b>			(Wheat fields harvested)		
	01/08		M1-M10			
	02/08			M1-M10	M1-M10	M1-M10
<b>F4</b>	<b>28/08</b>					
	29/08		M2-M5, M7, M8, M10 (M1, M6, M9 harvested)			
	30/08			M2-M5, M7, M8, M10 (M1, M6, M9 harvested)	M2-M5, M7, M8, M10 (M1, M6, M9 harvested)	M2-M5, M7, M8, M10 (M1, M6, M9 harvested)
<b>F5</b>	<b>11/09</b>			(Wheat & maize fields harvested)		

**Table 12-1 Campaign summary - Agriculture**

Unfortunately, summer 2018 was marked by an exceptional drought and these climatic conditions impacted the campaign. Indeed, crops were in advance and were harvested several weeks earlier than usual.

Complete dataset is then available for wheat for the flights 1 and 2 and for maize for flights 1, 2, 3. On flight 4, three maize fields were already harvested but data are complete for the 7 other fields.

Some ancillary data are also available for cancelled flights (flight 1 cancelled for wheat and flight 3 cancelled for wheat and maize).

Collected data are written in the file BeISAR\_agriculture\_database. Data are group by crop type in two sheets (.xlsx files). In each sheet, the data provided are

- the flight number,
- the date of the flight,
- the hour of the flight,
- the field name,

	<b>BeISAR Campaign 2018</b> <b>Final Report</b>		Doc.	RP-CSL-BEL-19003
			Date	10/08/2019
			Issue:	1.1
			Page:	<b>77 of 103</b>

- the plot ID,
- the development stage (BBCH scale),
- the plant height (all the measure and the mean),
- the GAI and Fcover obtain with the DHP and the software CANEYE,
- the biomass and the sowing density.

The database also includes:

- Drone pictures from the different missions
- GPS points where the measures were done
- Pictures taken in the fields (naming in a time format YYYYMMDD\_HHMMSS)
- Shapefiles containing the localization of the fields of maize and wheat and the areas of interest

## 12.4 Preliminary Analysis

### 12.4.1 Field data analysis

As it was explained earlier, the date when the data were collected did not totally correspond to the date of the flights. In the next graphs, the date of the flights is shown with the red lines and the data are shown with the points.

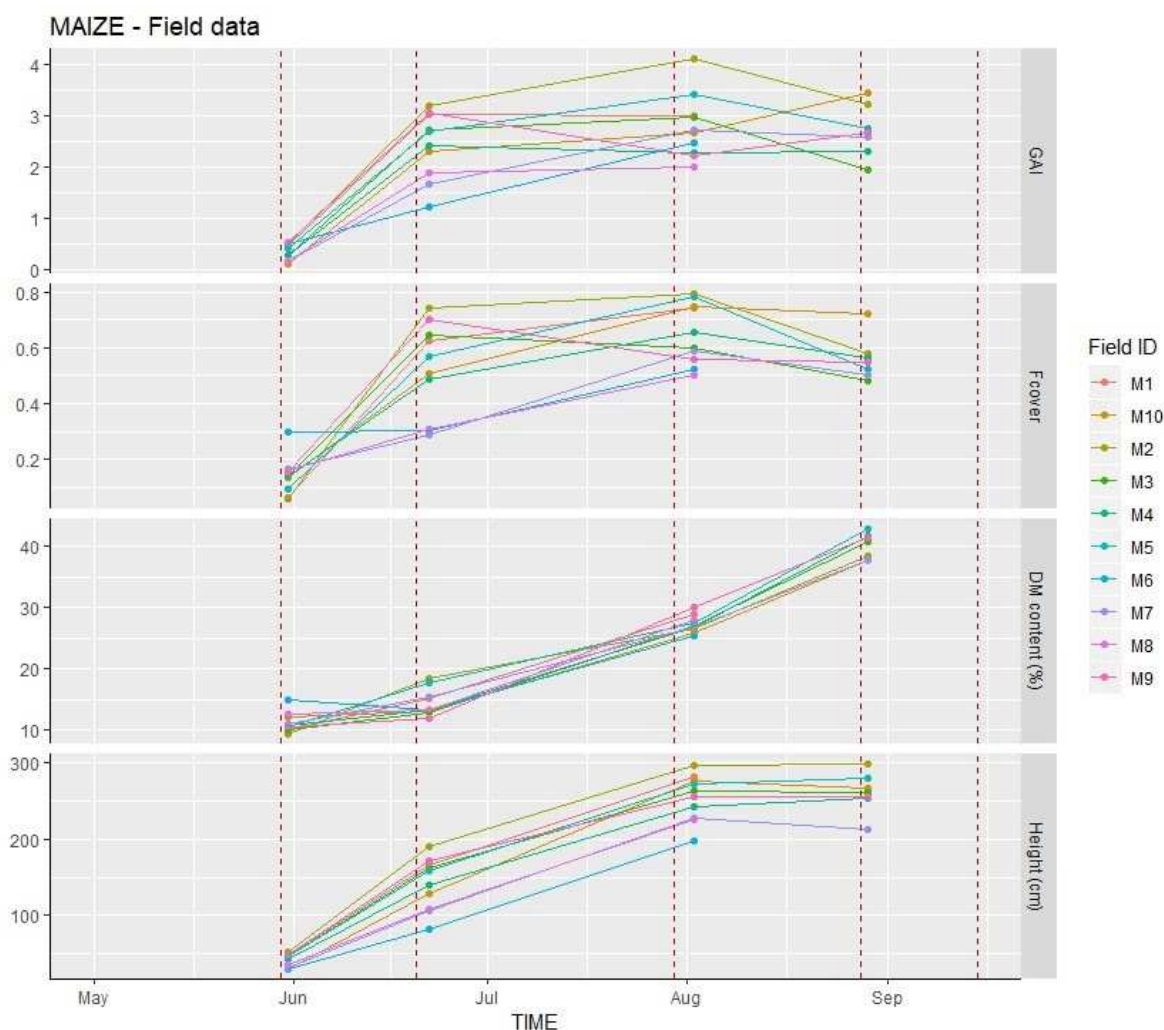


**Figure 12-4 Field data observation over the campaign for the agricultural variables (Fields of maize).**

Figure 12-4 shows the different variables observed for the agricultural data for the maize. We can observe here from the height that the maize grew faster between Flight 1 and 2, which is similar to the GAI and the Fcover. The dry matter content evolved over the all season.

In the GAI and Fcover variables, the variability is bigger around the flight 2 and 3. In addition, in the Fcover, we observe some fields where the ground was covered later.

The winter wheat field data are shown in Figure 12-5. At first, we observe a bigger variability in the data compare to the maize data. The first data set shows value for the GAI above three, which means that the wheat was already well develop before the first flight. The other variables show similar results. The dry matter content (DM) shows an outlier in the dataset around the second flight.

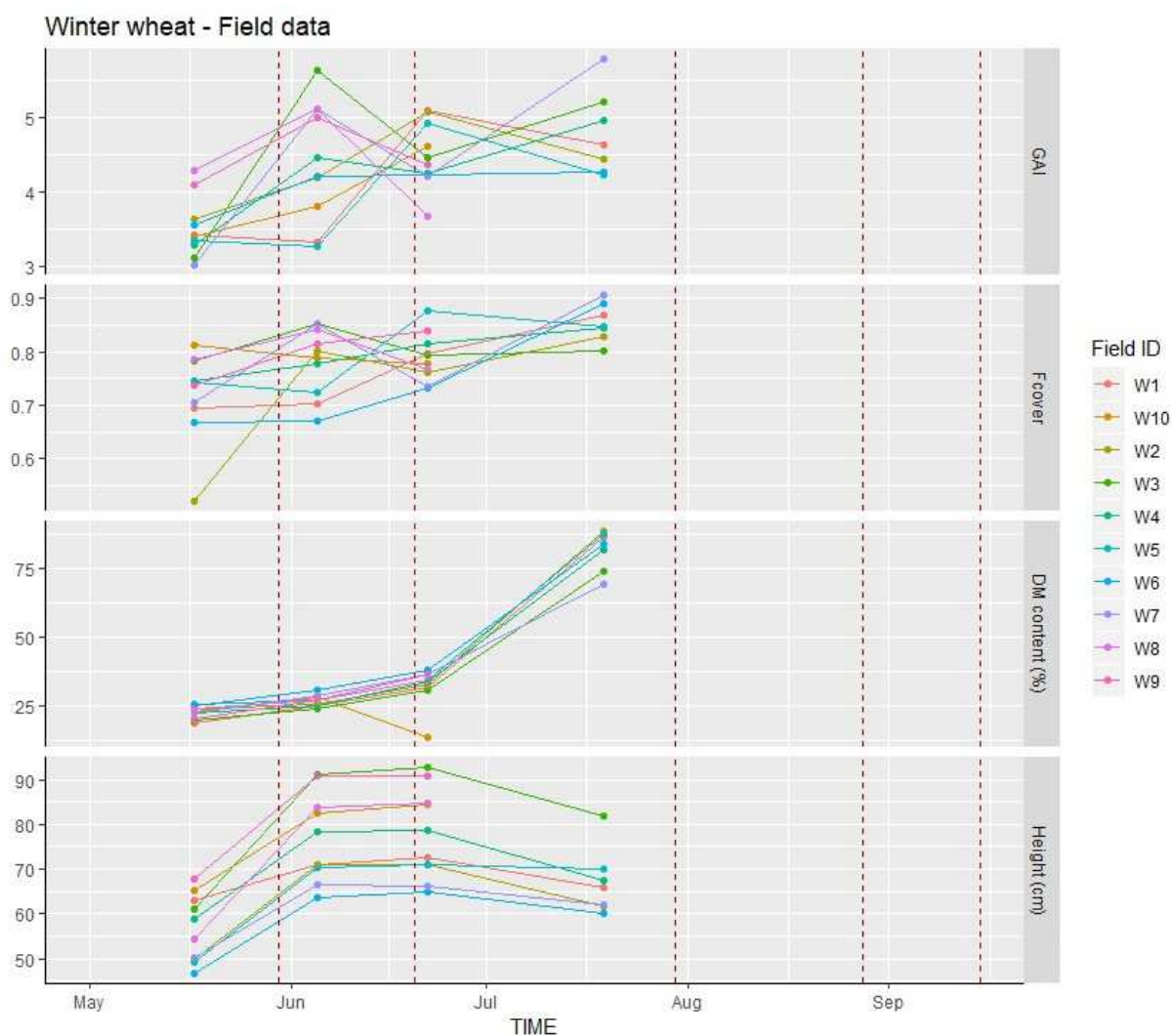


**Figure 12-5 Field data observation over the campaign for the agricultural variables (Fields of winter wheat)**

### 12.4.2 SAR data

After getting the images from the CSL for the five flights, they had to be georeferenced in order to extract the data corresponding to the different fields. For each flight, polarisation and interferometry, three images were provided, which correspond to the three different tracks explained in Chapter 8 (Airborne Campaign Implementation). Those tracks may bring a variability in the data due to the fact that distance between each field and the airborne was different for each track.

The amplitude (backscatter coefficient) was computed for the five flights and for the monostatic acquisition mode (SAR). As the tracks did not cover the all area of interest (Figure 12-6), some of the field never got any SAR data (M9 and M10) and other fields had some time no data but not all the time (W8-W9-W10).

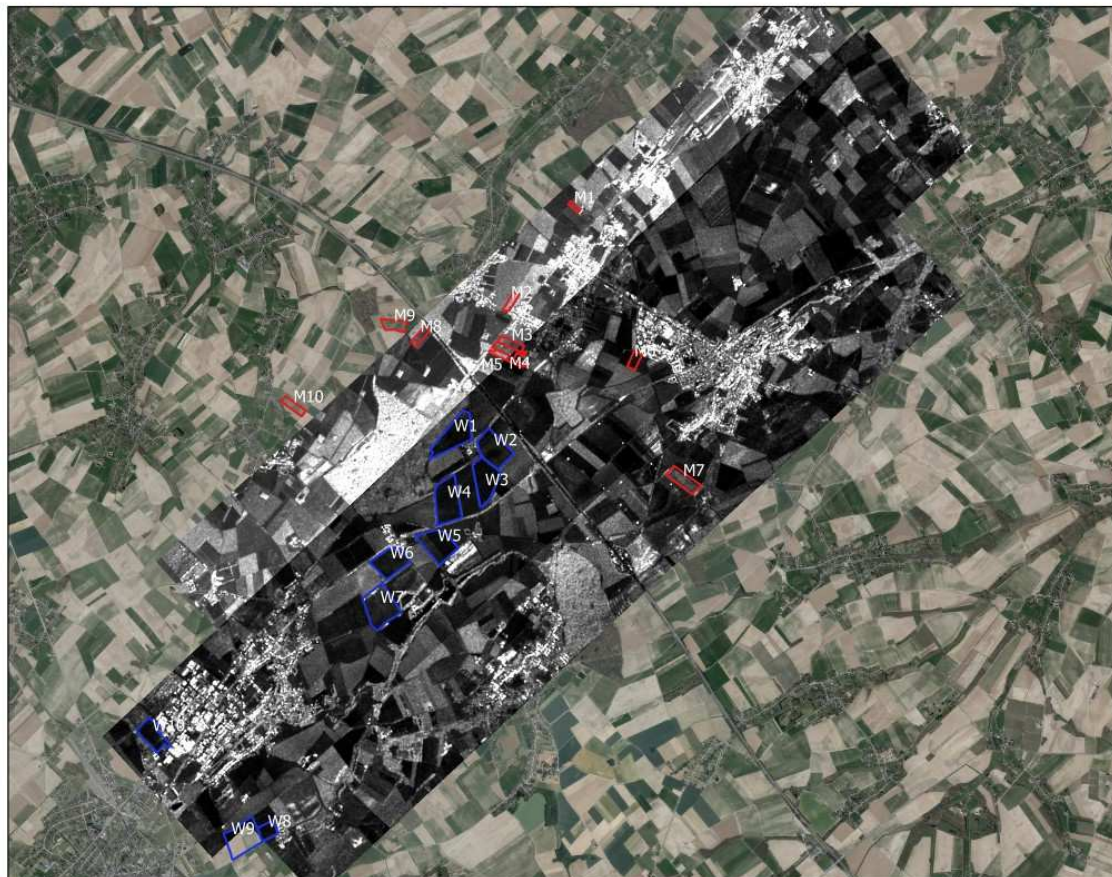


**Figure 12-6 The three tracks (A-Z-B) of the AT and the polarisation HH from the mission 2. The winter wheat fields are displayed in blue and the maize fields in red.**

#### 12.4.2.1 Backscatter coefficient vs field data (GAI)

The ratios VV/VH were computed pixel by pixel and then the values of the backscatter coefficient are extract with a zonal statistic for each field.

The first illustrations from the SAR data (Figure 12-7 and Figure 12-8) allow us some comments. The interferometry (along AT and across XT track) seems to bring the same kind of information. The polarisation VV shows higher backscatter coefficient values.

From the data from the maize fields, the tree first flights do not show any trend. On the contrary, in the fourth flight we observe that when the GAI is growing the backscatter coefficient grows too.

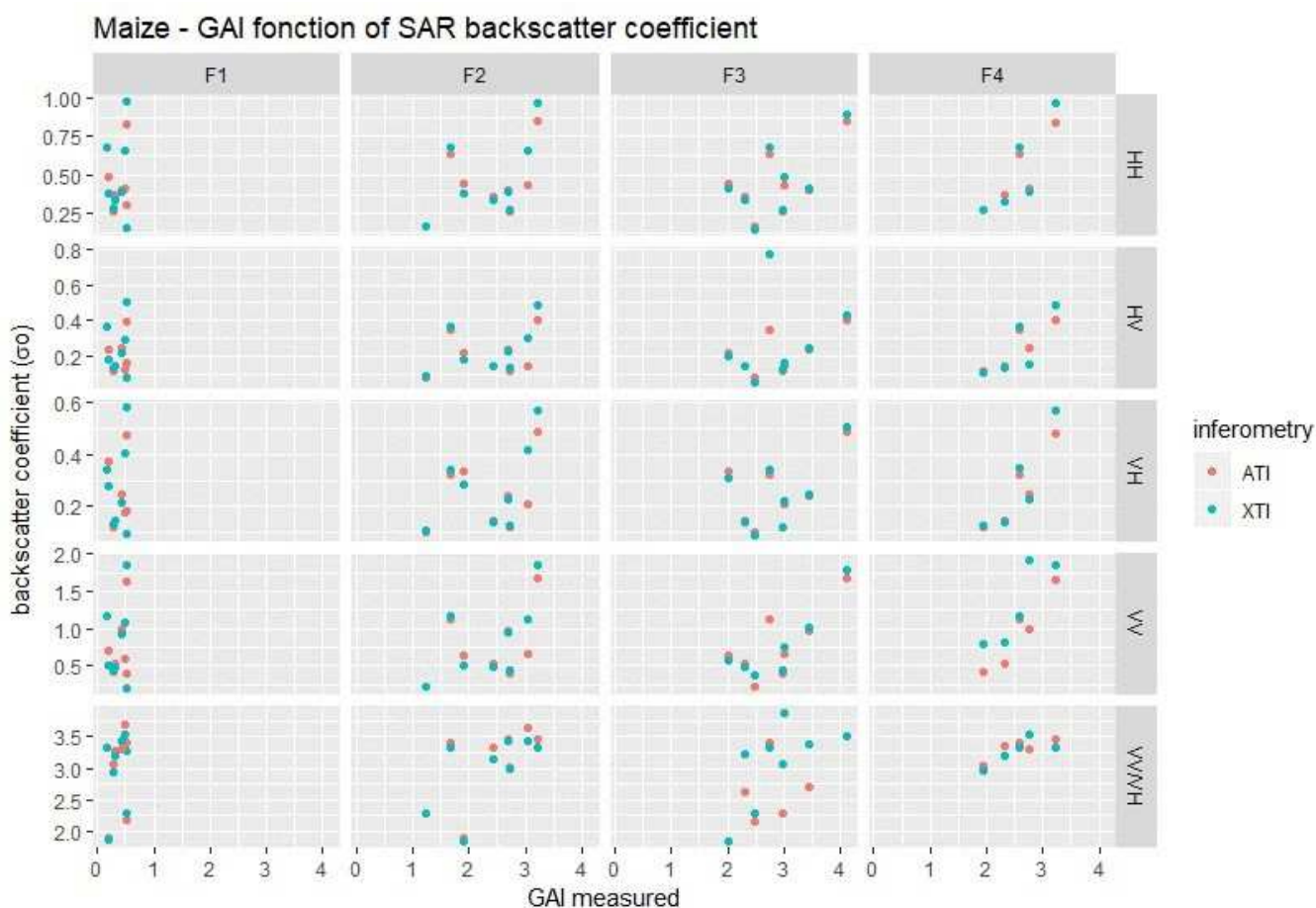


**Figure 12-7 GAI function of the backscatter coefficient (maize)**

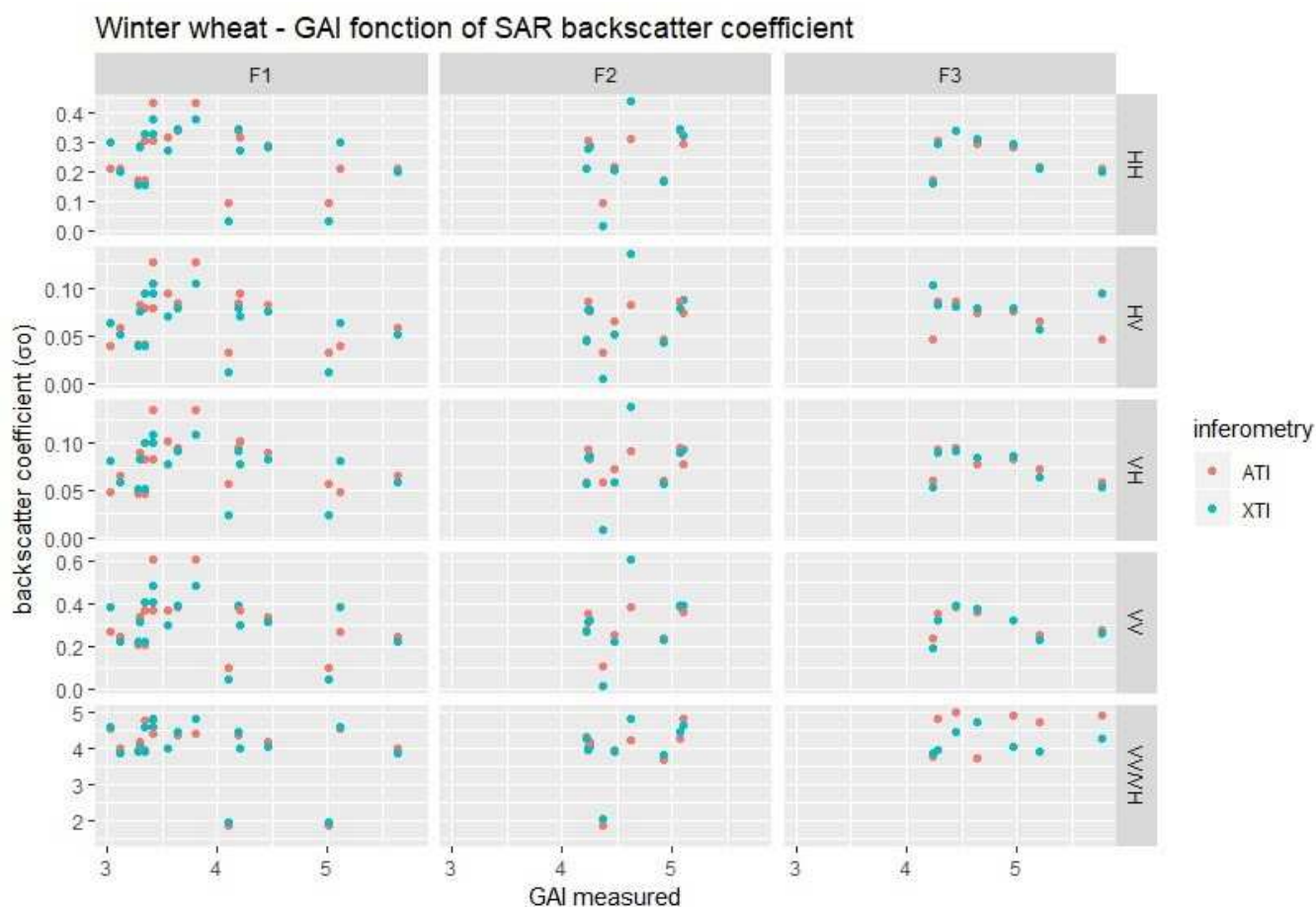


**Figure 12-8 GAI function of the backscatter coefficient (winter wheat)**

#### 12.4.2.2 SAR backscatter coefficient

After extracting the data for all the fields, we tried to see if there is change in the backscatter coefficient through the five flights.

The across track (XT) seems to show more change in the backscatter coefficient and that the change are happening after the two first flights (Figure 12-9).

Tree of the maize fields where harvested before the flight 4 (M1, M6 and M9). The M9 has no SAR data and the M1 and M6 are those where we observe the changes in HV, HH and VV. Nevertheless, others changes are also visible in field that were not yet harvested. For example, the M7 shows a big change in the F3 and M4 shows a big change in the F4.

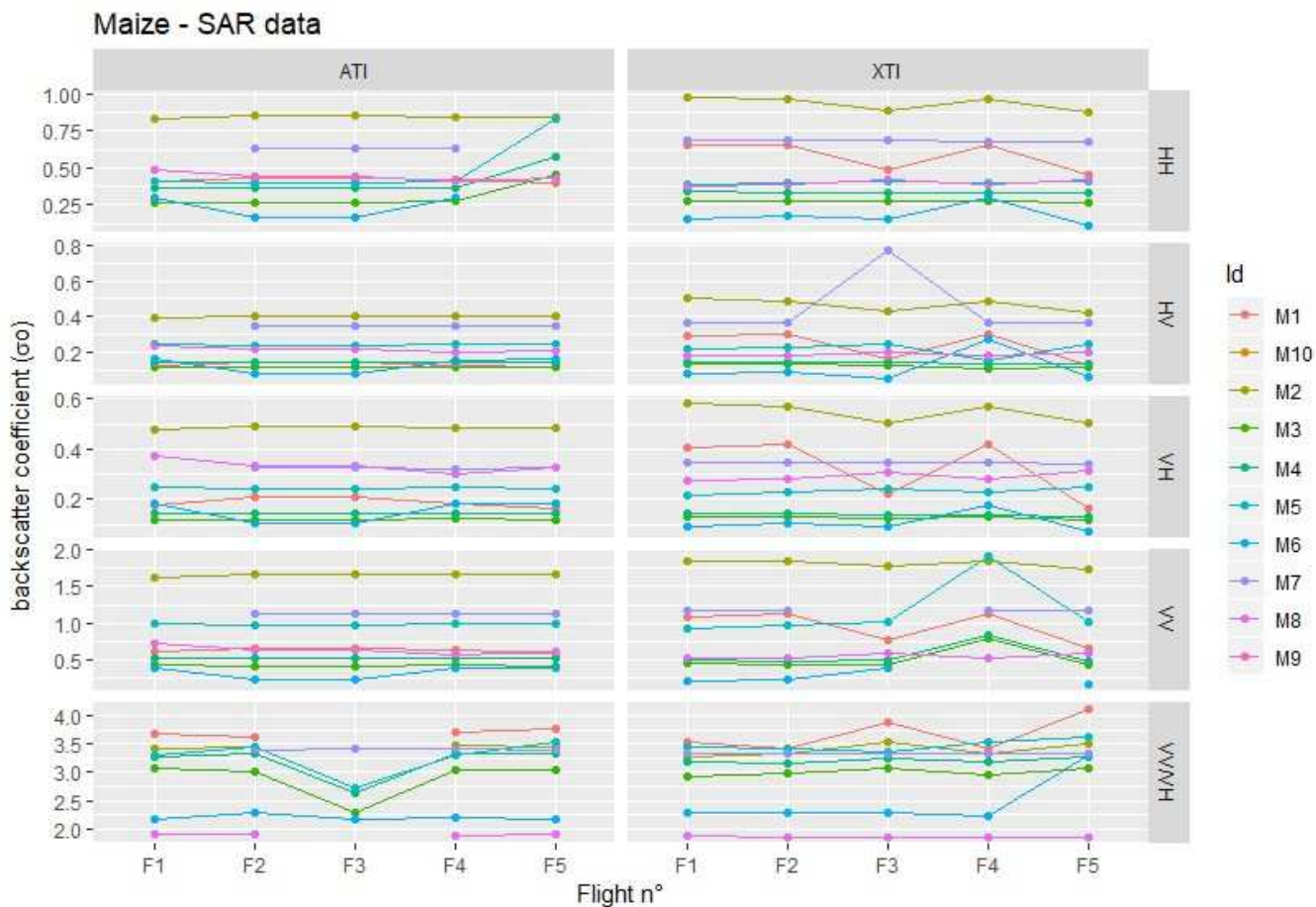


**Figure 12-9 SAR data for the different flights – all polarisation and interferometry.  
(Maize fields)**

The winter wheat fields show also some changes in the XT (Figure 12-10). For example, in the polarisation HV, most of the fields have a change in the backscattering. If the signal reacted in the same way as for the maize, the changes should have been seen on F3 and not on F4. All the winter wheat fields were harvested before the F3.

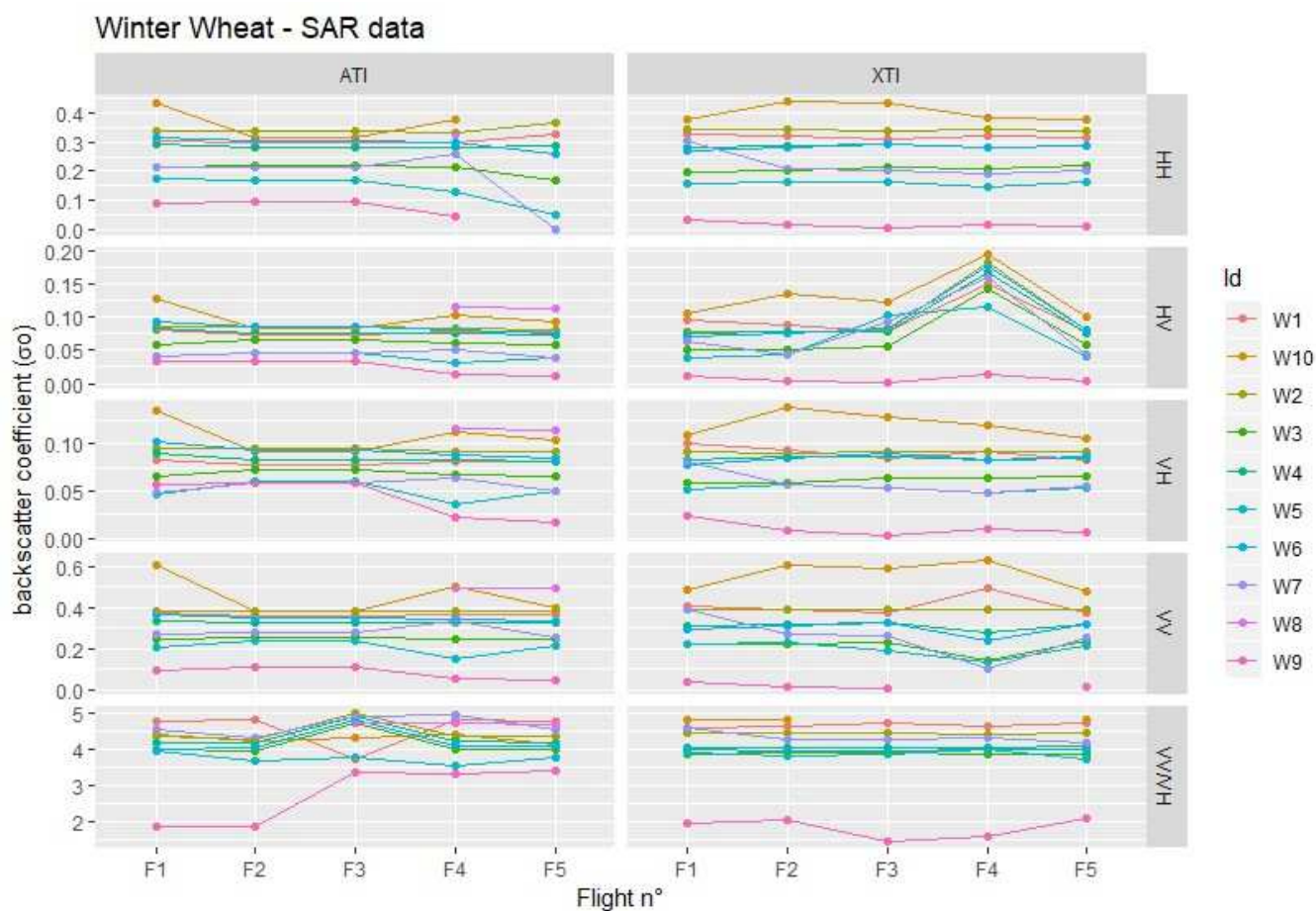


**Figure 12-10 SAR data for the different flights – all polarisation and interferometry (winter wheat fields)**

## 13 Sentinel-1 acquisitions

For each scheduled week of mission, the dates of Sentinel-1 passes were considered. Two missions were done within the same day of a S1 acquisition of the area of interest:

- M3 - 30/07/2018 : S1B, orbit 110, DSC
- M5 - 11/09/2018 : S1B, orbit 37, DSC

For the 3 other missions, there were S1 passes both the day before and the day after. Considering all descending orbits, we have:

- M1 (30/05): S1B, orbit 110, 31/05/2018
- M2 (20/06) : S1B, orbit 37, 19/06/2018
- M4 (28/08) : S1B, orbit 110, 29/08/2018

Day	Date	S1-Orbit	Platform	S1-Pass	BelSAR flight
<b>Flight 1 - Week 22</b>					
Monday	28-05-18	161	S1-A	ASCENDING	
Tuesday	29-05-18	88	S1-B	ASCENDING	
Wednesday	30-05-18				x
Thursday	31-05-18	110	S1-B	DESCENDING	←-----
Friday	01-06-18	37	S1-A	DESCENDING	
<b>Flight 2 - Week 25</b>					
Monday	18-06-18	110	S1-A	DESCENDING	
Tuesday	19-06-18	37	S1-B	DESCENDING	←-----
Wednesday	20-06-18				x
Thursday	21-06-18	161	S1-A	ASCENDING	
Friday	22-06-18	88	S1-B	ASCENDING	
<b>Flight 3 - Week 30</b>					
Saturday	28-07-18	88	S1-B	ASCENDING	
Sunday	29-07-18				
Monday	30-07-18	110	S1-B	DESCENDING	x ←-----
Tuesday	31-07-18	37	S1-A	DESCENDING	
Wednesday	01-08-18				
<b>Flight 4 - Week 35</b>					
Sunday	26-08-18	161	S1-B	ASCENDING	
Monday	27-08-18	88	S1-A	ASCENDING	
Tuesday	28-08-18				x
Wednesday	29-08-18	110	S1-A	DESCENDING	←-----
Thursday	30-08-18	37	S1-B	DESCENDING	
<b>Flight 5 - Week 37</b>					
Sunday	09-09-18				
Monday	10-09-18	110	S1-A	DESCENDING	
Tuesday	11-09-18	37	S1-B	DESCENDING	x ←-----
Wednesday	12-09-18				
Thursday	13-09-18	161	S1-A	ASCENDING	

**Table 13-1 Sentinel-1 acquisition planning**

## BeISAR Campaign 2018 Final Report

### 14 Summary and Conclusions

The BeISAR Campaign was conducted in spring and summer 2018, having in mind a persisting need to collect bistatic signatures and explore their possible use. The targeted application fields of the BeISAR campaign were soil moisture, agriculture and bistatic SAR science. Five airborne missions allowed to acquire multi-temporal bistatic full-polarimetric SAR data. The data were acquired at L-band with a frequency bandwidth of 50MHz centred on 1.375 MHz, with two airplanes flying in both along-track and across-track interferometric configurations, over an area being part of the HESBANIA Belgian BELAIR supersite. The flight altitude was either FL60 or FL70. In-situ ground measurements were done simultaneously or within a few days from each airborne campaign, to get information on soil roughness and moisture, as well as crop type and crop canopy properties in selected wheat and maize fields. Sentinel-1 data were also registered.

The SAR data were successfully processed. Post-processed navigation data shows the expected accuracies. The NESZ analysis reveals a better performance of bistatic images w.r.t. monostatic ones, due to coupling effects. IFR analysis presents comparable resolutions for monostatic and bistatic cases, both close to theoretical values, showing a good focusing processing.

The effects on the images resulting from mis-synchronization between the transmitter and receiver clocks, as well as from random phase noise due to the limited stability of the oscillators, were measured. Clock synchronization problems could be detected on the basis of the SAR data. A comparison between a set of monostatic and bistatic SAR images revealed a ground-range misalignment of the selected scatterers, due to a hardware-related constant delay estimated to be 100 ns. Furthermore, simulations allowed to show the impact of random phase noise on the ISLR, as well as the influence of the coherent integration time, though an experimental evaluation was not performed yet.

A python-based software was developed to generate outputs relevant for diagnostics and InSAR analysis. The coherence maps show a strong temporal coherence loss between the different missions as well as geometric decorrelation due to the relatively large perpendicular baseline. As a result, the coherence extracted from double-pass monostatic pairs is usually rather poor across the image and the results obtained from single-pass bistatic pairs will likely be more useful for further analysis.

As the BeISAR campaign per se consisted in the specification, planning and organization of the campaign, few scientific investigations on the resulting data have been done yet. As a follow up, a new project financed by Belspo and coordinated by UCLouvain, under the name *BeISAR\_Science*, is devoted to the scientific exploitation of the L-band SAR bistatic and in situ data. The specific contribution of the BeISAR time series will be investigated, combined with corresponding time series of C-band Sentinel-1 data and pairs of bistatic images acquired with the ground-based C-band bistatic radar receiver operated by RMA, for various land applications in the perspective of a better understanding of the physics and the potential of the bistatic SAR remote sensing and the definition of possible future SAR missions, the overarching

	<b>BeISAR Campaign 2018</b> <b>Final Report</b>		Doc.	RP-CSL-BEL-19003
			Date	10/08/2019
			Issue:	1.1
			Page:	<b>87</b> of <b>103</b>

---

research objective being to explore the application potential of mono- and bistatic InSAR/PolInSAR products acquired in L/C-band, focusing on three fields of applications: change detection, hydrology, and agriculture.

In particular, as noted in Section 10, it would be particularly useful to optimize the interferometric coherence, by removing the spatially-variable co-registration errors due to the residual motion of the airplanes and/or mis-synchronization issues.

In addition, it would be useful to implement the geo-referencing of the tif images for easier comparison with other images.

## Appendix A – MetaSAR-L NetCDF data format

Detailed information about the contents of the delivered NetCDF files is provided in this appendix. File naming and matrixes dimensions are provided in paragraph A.1. The main variables and parameters used are listed in paragraphs A.2 and A.30.

### A.1 File names

In this paragraph it is described the meaning of the different fields in the name of the delivered files.

Because of the bistatic nature of the BeISAR airborne acquisitions, there are two sensors, namely L1 and L2. Each sensor Li records eight different NetCDF files for each datatake: four for the monostatic case and four for the bistatic case, see Figure A-1.

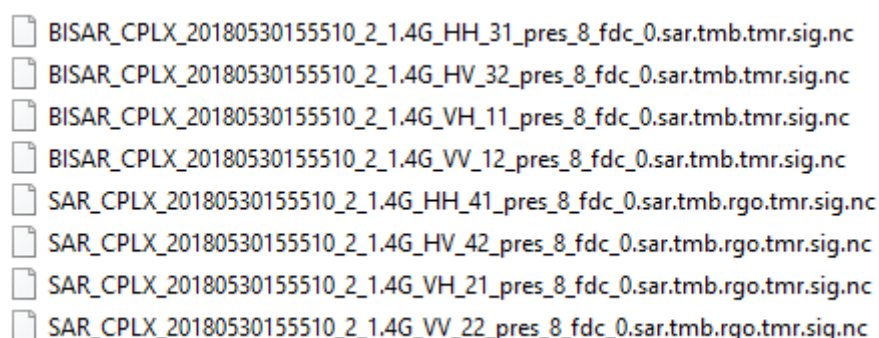


**Figure A-1 Example of delivered SAR data set.**

In the following the meaning of the different fields in the file name are explained.

SAR_CPLX	The file contains monostatic SLC focused SAR data.
BISAR_CPLX	The file contains bistatic SLC focused SAR data.
20180530155510:	Starting time of the acquisition in the format YYYYMMDDHHMMSS, where YYYY is the year, MM the month, DD the day, HH the hour, MM the minutes and SS the seconds, in UTC time.
2:	Refers to the recording system number (in a bistatic configuration there are 2 sensors in two different aircraft, 1 and 2 for L1 and L2, respectively).
VV:	Polarization of the transmitting and receiving channel, respectively.
12:	Channel number. The first and second number represent the transmitting and the receiving antennas, respectively.
pres_8:	The presuming factor applied to the Pulse Repetition Frequency (in this case 8).

fdc\_0: Doppler centroid: the central frequency [Hz] of the processed bandwidth (in this case 0).

The extension of the name indicates the processing steps applied to the data.

- .sar SAR image focused through backprojection algorithm;
- .sig SAR image is radiometrically calibrated;
- .tmb Phase modulation due to topography have been added back.
- .rgo SAR images is calibrated for range delay offset.
- .tmr Phase modulation due to topography have been removed.
- .nc SAR data and metadata have been encapsulated in NetCDF format.

The NetCDF files are composed by several matrixes of different dimensions; as an example, the dataset given in Figure A-1 is characterized by the following values:

*GroundRange* = 2976  
*CrossRange* = 9232  
*GPSTime* = 19901  
*AntPatternAngles* = 359  
*ModelTransformationTagRows* = 4  
*ModelTransformationTagCols* = 4

The *GroundRange* and *CrossRange* dimensions are related to the pre-defined grid of the focused SAR image, see Figure A-2. The grid is uniformly sampled in space. The *GroundRange* dimension refers to the number of samples in the direction perpendicular to the flight direction. The *CrossRange* dimension refers to the number of samples in the direction parallel to the nominal flight direction.

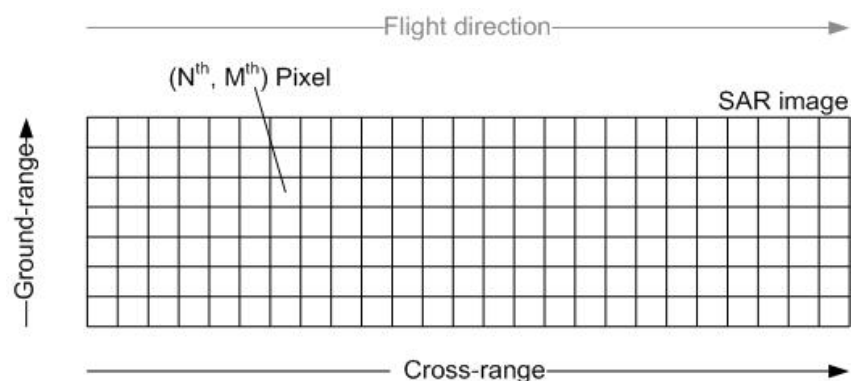


**Figure A-2 Dimensions of the provided SAR images**

The *GPSTime* provides the time dimension of the (post-processed) navigation data.

The *AntPatternAngles* is the number of samples characterizing the antenna pattern, both in azimuth and in elevation directions, equally spaced in  $[-180^\circ, 180]$ .

	<b>BelSAR Campaign 2018</b> <b>Final Report</b>		Doc.	RP-CSL-BEL-19003
			Date	10/08/2019
			Issue:	1.1
			Page:	90 of 103

The *ModelTransformationTagRows* and *ModelTransformationTagCols* refers to the matrix dimensions that relates the SAR image grid to the model space (geographical coordinates) grid.

## A.2 Variables

The variables handled within the delivered NetCDF files are shortly described in the following paragraphs 0 and 0, for 1D and 2D cases respectively.

### A.2.1 Variables 1D

#### *GroundRange*

*Size:* 2976x1

*Dimensions:* *GroundRange*

*Datatype:* single

*Attributes:*

*long\_name* = 'Dimension of the image in ground range direction '

*units* = '[m]'

The *GroundRange* variable defines the grid dimension of the SAR images in the ground range direction. The difference between two consecutive samples of the *GroundRange* variable defines the ground-range spacing.

#### *CrossRange*

*Size:* 9232x1

*Dimensions:* *CrossRange*

*Datatype:* single

*Attributes:*

*long\_name* = 'Dimension of the image along cross-range direction'

*units* = '[m]'

The *CrossRange* variable defines the grid dimension of the SAR images in the cross range direction. The difference between two consecutive samples of the *CrossRange* variable defines the cross-range spacing.

The *GPSTime* variable provides the GPS time tag of each state vector.

#### *GPSTime*

*Size:* 19901x1

*Dimensions:* *GPSTime*

*Datatype:* double

*Attributes:*

*long\_name* = 'GPS time (orbit)'

*units* = '[s]'

	<b>BeISAR Campaign 2018</b> <b>Final Report</b>		Doc.	RP-CSL-BEL-19003
			Date	10/08/2019
			Issue:	1.1
			Page:	91 of 103

The state vector is composed by the following information about position and attitude of the aircraft:  
*OrbitLatitude*, *OrbitLongitude*, *OrbitHeight*, *OrbitHeading*, *OrbitRoll*, *OrbitPitch*:

#### *OrbitLatitude*

*Size:* 19901x1

*Dimensions:* GPSTime

*Datatype:* double

*Attributes:*

*long\_name* = 'Latitude of the antenna orbit'

*units* = '[deg.]'

#### *OrbitLongitude*

*Size:* 19901x1

*Dimensions:* GPSTime

*Datatype:* double

*Attributes:*

*long\_name* = 'Longitude of the antenna orbit'

*units* = '[deg.]'

#### *OrbitHeight*

*Size:* 19901x1

*Dimensions:* GPSTime

*Datatype:* double

*Attributes:*

*long\_name* = 'Antenna height above WGS84'

*units* = '[m]'

#### *OrbitHeading*

*Size:* 19901x1

*Dimensions:* GPSTime

*Datatype:* double

*Attributes:*

*long\_name* = 'Heading (relative to the True North) angles'

*units* = '[deg.]'

#### *OrbitRoll*

*Size:* 19901x1

*Dimensions:* GPSTime

*Datatype:* double

*Attributes:*

*long\_name* = 'Roll angles'

*units* = '[deg.]'

#### *OrbitPitch*

*Size:* 19901x1

*Dimensions:* GPSTime

	<b>BelSAR Campaign 2018</b> <b>Final Report</b>	Doc.	RP-CSL-BEL-19003
		Date	10/08/2019
		Issue:	1.1
		Page:	92 of 103

*Datatype: double*

*Attributes:*

*long\_name = 'Pitch angles'*

*units = '[deg.]'*

For bistatic images, a second set of vectors describes the position of the second sensor

*GPSTime2*

*Size: 19901x1*

*Dimensions: GPSTime*

*Datatype: double*

*Attributes:*

*long\_name = 'GPS time (orbit) bistatic'*

*units = '[s]'*

*OrbitLatitude2*

*Size: 19901x1*

*Dimensions: GPSTime*

*Datatype: double*

*Attributes:*

*long\_name = 'Latitude of the antenna orbit bistatic'*

*units = '[]'*

*OrbitLongitude2*

*Size: 19901x1*

*Dimensions: GPSTime*

*Datatype: double*

*Attributes:*

*long\_name = 'Longitude of the antenna orbit bistatic'*

*units = '[]'*

*OrbitHeight2*

*Size: 19901x1*

*Dimensions: GPSTime*

*Datatype: double*

*Attributes:*

*long\_name = 'Antenna height above WGS84 bistatic'*

*units = '[deg.]'*

*OrbitHeading2*

*Size: 19901x1*

*Dimensions: GPSTime*

*Datatype: double*

*Attributes:*

*long\_name = 'Heading (relative to the True North) angles bistatic'*

*units = '[deg.]'*

*OrbitRoll2*

*Size: 19901x1*

*Dimensions: GPSTime*

*Datatype: double*

*Attributes:*

*long\_name = 'Roll angles bistatic'*

*units = '[deg.]'*

*OrbitPitch2*

*Size: 19901x1*

*Dimensions: GPSTime*

*Datatype: double*

*Attributes:*

*long\_name = 'Pitch angles bistatic'*

*units = '[deg.]'*

## A.2.2 Variables 2D

*SigmaImageSingleLookRealPart*

*Size: 2976x9232*

*Dimensions: GroundRange, CrossRange*

*Datatype: double*

*Attributes:*

*long\_name = 'sigma-nought calibrated and ground projected real-part SLC image'*

*units = '[]'*

The *SigmaImageSingleLookRealPart* is the real-part of the  $\sigma_0$  calibrated SLC focused SAR data.

*SigmaImageSingleLookImaginaryPart*

*Size: 2976x9232*

*Dimensions: GroundRange, CrossRange*

*Datatype: double*

*Attributes:*

*long\_name = 'sigma-nought calibrated and ground projected imaginary-part SLC image'*

*units = '[]'*

The *SigmaImageSingleLookImaginaryPart* is the imaginary-part of the  $\sigma_0$  calibrated SLC focused SAR data.

The position of each pixel in the SAR image in WGS-84 ellipsoid is given by:

*LatImage*

*Size: 2976x9232*

	<b>BelSAR Campaign 2018</b> <b>Final Report</b>		Doc.	RP-CSL-BEL-19003
			Date	10/08/2019
			Issue:	1.1
			Page:	94 of 103

*Dimensions: GroundRange, CrossRange*

*Datatype: double*

*Attributes:*

*long\_name = 'latitude of the pixels in the image'*

*units = '[deg]'*

*LonImage*

*Size: 2976x9232*

*Dimensions: GroundRange, CrossRange*

*Datatype: double*

*Attributes:*

*long\_name = 'longitude of the pixels in the image'*

*units = '[deg]'*

*DEMImage*

*Size: 2976x9232*

*Dimensions: GroundRange, CrossRange*

*Datatype: single*

*Attributes:*

*long\_name = 'Elevation (WGS84) of the pixels in the image'*

*units = '[m]'*

The *DEMImage* is the WGS-84 height model with the same geometry and the same dimension of the processed SLC SAR data. For each pixel of the SLC SAR data a DEM height value is given, corresponding to the one which has been used during the processing.

The timing and position of antenna associated with each focused pixel is given explicitly through a matrix of the same size of the SAR image as follows:

*OrbLatImage*

*Size: 2976x9232*

*Dimensions: GroundRange, CrossRange*

*Datatype: double*

*Attributes:*

*long\_name = 'latitude of the sensor for each pixel in the image'*

*units = '[deg]'*

*OrbLonImage*

*Size: 2976x9232*

*Dimensions: GroundRange, CrossRange*

*Datatype: double*

*Attributes:*

*long\_name = 'longitude of the sensor for each pixel in the image'*

	<b>BelSAR Campaign 2018</b> <b>Final Report</b>		Doc.	RP-CSL-BEL-19003
			Date	10/08/2019
			Issue:	1.1
			Page:	95 of 103

*units = '[deg]'*

#### *OrbHeightImage*

*Size: 2976x9232*

*Dimensions: GroundRange, CrossRange*

*Datatype: double*

*Attributes:*

*long\_name = 'Height above ellipsoid WGS84 of the sensor for each pixel in the image'*

*units = '[m]'*

#### *OrbTimeImage*

*Size: 2976x9232*

*Dimensions: GroundRange, CrossRange*

*Datatype: double*

*Attributes:*

*long\_name = 'Time (GPS sec week) of the sensor for each pixel in the image'*

*units = '[s]'*

The CallImage gives the calibration factor used to radiometrically calibrate each pixel of the SAR image.

#### *CallImage*

*Size: 2976x9232*

*Dimensions: GroundRange, CrossRange*

*Datatype: single*

*Attributes:*

*long\_name = 'Calibration Factor for each pixel in the image'*

*units = '[dB]'*

The *OrbitImage* is the file which links the pixel index of the SAR image with the GPStime vector. It corresponds to the time and therefore position within the trajectory where each pixel of the complex image has been focused. By reading a value in the OrbitImage, one can interpolate for the corresponding position and attitude value. With OrbitImage, GPStime and the navigation data, the matrix OrbLatImage, OrbLonImage and OrbHeightImage can be retrieved again as well as the roll, pitch, yaw for each pixel.

#### *OrbitImage*

*Size: 2976x9232*

*Dimensions: GroundRange, CrossRange*

*Datatype: single*

*Attributes:*

*long\_name = 'LUT to find the GPS time associated with the SLC image pixels'*

*units = '[]'*

For bistatic images, a second set of matrix describes the position of the second sensor for each pixel in the image as follows

#### *OrbLatImage2*

*Size: 2976x9232*

*Dimensions: GroundRange,CrossRange*

*Datatype: double*

*Attributes:*

*long\_name = 'latitude of the bistatic sensor for each pixel in the image'*

*units = '[deg]'*

#### *OrbLonImage2*

*Size: 2976x9232*

*Dimensions: GroundRange,CrossRange*

*Datatype: double*

*Attributes:*

*long\_name = 'longtitude of the bistatic sensor for each pixel in the image'*

*units = '[deg]'*

#### *OrbHeightImage2*

*Size: 2976x9232*

*Dimensions: GroundRange,CrossRange*

*Datatype: double*

*Attributes:*

*long\_name = 'Height above ellipsoid WGS84 of the bistatic sensor for each pixel in the image'*

*units = '[m]'*

## **A.3 Parameters**

### **A.3.1 The RF antenna**

The radiation patterns of the radar antennas are considered in terms of the following parameters:

#### *AntPatternAngles*

*Size: 361 x 1*

*Datatype: double*

*Attributes: long\_name = 'Antenna pattern angular dependence'*

*units = '[deg.]'*

*It varies from -180 to 180 degrees with a spacing of 1 deg.*

#### *TxElevationGain*

*Size:* 361 x 1

*Dimensions:* AntPatternAngles

*Datatype:* double

*Attributes:* long\_name = 'Transmitting antenna gain in elevation'  
units = '[dB]'

#### *TxAzimuthGain*

*Size:* 361 x 1

*Dimensions:* AntPatternAngles

*Datatype:* double

*Attributes:* long\_name = 'Transmitting antenna gain in azimuth'  
units = '[dB]'

#### *RxElevationGain*

*Size:* 361 x 1

*Dimensions:* AntPatternAngles

*Datatype:* double

*Attributes:* long\_name = 'Receiving Antenna elevation gain'  
units = '[dB]'

#### *RxAzimuthGain*

*Size:* 361 x 1

*Dimensions:* AntPatternAngles

*Datatype:* double

*Attributes:* long\_name = 'Receiving Antenna azimuth gain'  
units = '[dB]'

### A.3.2 The transformation matrix

In order to be geolocated, the processed SAR image has to be properly “aligned” according a geographical coordinate system, in this case the UTM. To do that, a transformation matrix is applied to the processed image, so that is properly rotated and translated before its conformal projection.

#### *ModelTransformationTag*

*Size:* 4x4

*Dimensions:* ModelTransformationTagRows, ModelTransformationTagCols

*Datatype:* double

The transformation matrix is defined as follows:

$$\begin{array}{cccc}
 -D_x \cos(rot) & D_y \sin(rot) & 0 & X\_Offset \\
 D_x \sin(rot) & D_y \cos(rot) & 0 & Y\_Offset \\
 0 & 0 & Z\_scale & Z\_Offset \\
 0 & 0 & 0 & 1
 \end{array}$$

where  $D_x$  and  $D_y$  are the spacing in cross- and along- track dimensions, respectively;  $rot$  is the orientation of the grid with respect to the geographical North;  $X\_Offset$  and  $Y\_Offset$  are the actual UTM offsets, while  $Z\_Offset = Z\_scale = 0$ .

### A.3.3 Others

#### StartYear

Size: 1x1

Datatype: int32

Attributes: long\_name = 'Year of the Start of Acquisition'  
units = '[year]'

#### StartMonth

Size: 1x1

Datatype: int32

Attributes: long\_name = 'Month of the Start of Acquisition'  
units = '[month]'

#### StartDay

Size: 1x1

Datatype: int32

Attributes: long\_name = 'Day of the Start of Acquisition'  
units = '[day]'

#### StartHour

Size: 1x1

Datatype: int32

Attributes: long\_name = 'Hour of the Start of Acquisition (UTC)'  
units = '[hour]'

#### StartMin

Size: 1x1

Datatype: int32

Attributes: long\_name = 'Minutes of the Start of Acquisition (UTC)'  
units = '[min]'

#### StartSec

Size: 1x1

Datatype: single

Attributes: long\_name = 'Seconds of the Start of Acquisition (UTC)'  
units = '[sec]'

#### FinalYear

Size: 1x1

Datatype: int32

Attributes: long\_name = 'Year of End of Acquisition'  
units = '[year]'

	<b>BeISAR Campaign 2018</b>		Doc.	RP-CSL-BEL-19003
	<b>Final Report</b>		Date	10/08/2019
			Issue:	1.1
			Page:	99 of 103

#### FinalMonth

Size: 1x1

Datatype: int32

Attributes: long\_name = 'Month of End of Acquisition'  
units = '[month]'

#### FinalDay

Size: 1x1

Datatype: int32

Attributes: long\_name = 'Day of End of Acquisition'  
units = '[day]'

#### FinalHour

Size: 1x1

Datatype: int32

Attributes: long\_name = 'Hour of End of Acquisition (UTC)'  
units = '[hour]'

#### FinalMin

Size: 1x1

Datatype: int32

Attributes: long\_name = 'Minutes of End of Acquisition (UTC)'  
units = '[min]'

#### FinalSec

Size: 1x1

Datatype: single

Attributes: long\_name = 'Seconds of End of Acquisition (UTC)'  
units = '[sec]'

#### TxPolarization

Size: 1x1

Datatype: char

Attributes: long\_name = 'TX Polarization'  
units = '[]'

#### RxPolarization

Size: 1x1

Datatype: char

Attributes: long\_name = 'RX Polarization'  
units = '[]'

#### LookDirection

Size: 1x1

Datatype: char

Attributes: long\_name = 'Look direction: R = Right, L = Left'  
units = '[]'

#### CentralFreq

Size: 1x1  
 Datatype: single  
 Attributes: long\_name = 'Central frequency'  
                   units = '[Hz]'

#### TransmittedBandWidth

Size: 1x1  
 Datatype: single  
 Attributes: long\_name = 'Transmitted bandwidth'  
                   units = '[Hz]'

#### PRF

Size: 1x1  
 Datatype: single  
 Attributes: long\_name = 'Pulse Repetition Frequency'  
                   units = '[Hz]'

The average aircraft velocity during the acquisition is noted as a reference.

#### MeanForwardVelocity

Size: 1x1  
 Datatype: single  
 Attributes: long\_name = 'Flight direction velocity'  
                   units = '[m/s]'

Depending on the desired resolution in cross range direction, the operating PRF is reduced by an integer value, the Presuming Factor (PF). The *DopplerPresumming* gives the value of the PF.

#### DopplerPresumming

Size: 1x1  
 Datatype: single  
 Attributes: long\_name = 'Doppler Presumming Factor'  
                   units = '[]'

The data are filtered in the frequency domain according to the desired Doppler centroid and resolution. The *MinProcessedDoppler* and *MaxProcessedDoppler* gives the values used to filtered out the spectrum. The Doppler centroid is given by  $(\text{MinProcessedDoppler} + \text{MaxProcessedDoppler})/2$ .

#### MinProcessedDoppler

Size: 1x1  
 Datatype: single  
 Attributes: long\_name = 'Minimum Processed Doppler'

*units* = '[Hz]'

*MaxProcessedDoppler*

*Size:* 1x1

*Datatype:* single

*Attributes:* *long\_name* = 'Maximum Processed Doppler'

*units* = '[Hz]'

The UTM zone used for gridding the SAR image is given as:

*UTMZone*

*Size:* 1x1

*Datatype:* int32

*Attributes:* *long\_name* = 'UTM zone'

*units* = '[]'

The geographical coordinates of the four corners of the delivered SAR image are also given, as a reference.

*Latitude11*

*Size:* 1x1

*Datatype:* double

*Attributes:* *long\_name* = 'Latitude of image corner (1, 1)'

*units* = '[deg.]'

*Longitude11*

*Size:* 1x1

*Datatype:* double

*Attributes:* *long\_name* = 'Longitude of image corner (1, 1)'

*units* = '[deg.]'

*Latitude12*

*Size:* 1x1

*Datatype:* double

*Attributes:* *long\_name* = 'Latitude of image corner (1, 10592)'

*units* = '[deg.]'

*Longitude12*

*Size:* 1x1

*Datatype:* double

*Attributes:* *long\_name* = 'Longitude of image corner (1, 10592)'

*units* = '[deg.]'

And similarly, for the other two SAR image corners 21 and 22.

	<b>BelSAR Campaign 2018</b> <b>Final Report</b>		Doc.	RP-CSL-BEL-19003
			Date	10/08/2019
			Issue:	1.1
			Page:	<b>102 of 103</b>

The SystemType variable indicates if the dataset has been acquired in a monostatic or bistatic configuration .

#### *SystemType*

*Size:* 1x1

*Dimensions:*

*Datatype:* char

*Attributes:* long\_name = 'System type: M for monostatic, B for Bistatic'  
units = '[]'

The pixels in the SAR image that do not correspond to a valid SAR data are given as dummy values (typically -9999).

#### *Dummy*

*Size:* 1x1

*Datatype:* int32

*Attributes:* long\_name = 'Dummy value'  
units = '[]'

## Appendix B - Acronyms

AOI	Area of Interest
AT	Along-Track
BBCH	Biologische Bundesanstalt, Bundessortenamt und CHemische Industrie
BIPT	Belgian Institute for Post and Telecommunications
CR	Corner Reflector
DHP	Digital Hemispheric Picture
DM	Dry Matter
EASA	European Aviation Safety Agency
FL	Flight Level
FMCW	Frequency Modulated Continuous Wave
GPS	Ground Positioning System
GPSDO	GPS Disciplined Oscillator
GAI	Green Area Index
HPA	High Power Amplifier
IMU	Inertial Measurement Unit
IRF	Impulse Response function
ISLR	Integrated Side Lobe Ratio
LNA	Low Noise Amplifier
M#	Mission nr #
NESZ	Noise-Equivalent Sigma Zero
PRF	Pulse Repetition Frequency
PSF	Point Spread Function
RCS	Radar Cross Section
RD	Range-Doppler
RMS	Root Mean Square
SLC	Single-Look Complex
TDR	Time Domain Reflectometry
XT	Across-Track